NEXAFS/XPS study of organic molecules adsorbed on rutile TiO_2(110) and Al_2O_3/Ni_3Al(111) substrates

Zur Erlangung des akademischen Grades eines
DOKTORS DER NATURWISSENSCHAFTEN
(Dr. rer. nat.)
Fakultät für Chemie und Biowissenschaften
Karlsruher Institut für Technologie (KIT) - Universitätsbereich

genehmigte
DISSERTATION

von
Michael Naboka

aus
Charkow, Ukraine

Dekan: Prof. Dr. Peter Roesky
Referent: Prof. Dr. Christof Wöll
Korreferent: Prof. Dr. Jan-Dirk Grunwaldt
Tag der mündlichen Prüfung: 24.10.2014

ABSTRACT

The spectroscopic studies of metal oxide surface interaction with different organic molecules have been performed for the needs of organic electronics, heterogeneous catalysis and surface chemistry. Three different systems: terephthalic acid (TPA) on rutile TiO_2(110), azobenzene on rutile-TiO_2(110), and tetracene on Al_2O_3/Ni_3Al (111) were investigated.

It was found that TPA adsorbs flat on rutile-TiO_2(110) at submonolayer coverage and adopts an upstanding orientation at monolayer coverage. The importance of this result lies in the fact that it demonstrated the suitability of metal oxides in particular TiO_2 to be used as a template for the structured organic monolayers growth.

The interaction of azobenzene with rutile-TiO_2(110) leads to the scissoring of N=N bond and formation of two phenyl imides with a flat orientation at room temperature Additionally azobenzene was shown to remain intact at the temperatures of 100 K.

Finally a phase transition study in thin films of tetracene adsorbed on Al_2O_3/Ni_3Al(111) showed that upon deposition onto cold (100 K) substrate a monolayer of tetracene molecules adopts a disordered adsorption configuration with a molecular platelets inclined with respect to the surface. The molecular orientation can be directly related to the luminescent properties of tetracene. Tetracene molecules oriented more flat on the AlOx/Ni_3Al(111) substrate are expected to show an electronic coupling of occupied and unoccupied states to those of the metal substrate through the thin oxide, as a result luminescence is quenched. For molecules with a significant tilt relative to the substrate, however, one would expect this coupling to be substantially weaker, thus restoring the tetracene luminescent properties.

TABLE OF CONTENTS

Abstract i

Table of Figures v

List of abbreviations ix

Notation list x

1. Introduction 1

1.1. Metal Oxides 2

1.2. Titanium dioxide 4

1.2.1 Structure of TiO_2 crystal 5

1.2.2 Rutile TiO_2 surface 5

1.2.3 Surface structure of stoichiometric, reduced and reoxidized rutile TiO_2(110) 6

1.2.4 Interaction of organic molecules with rutile TiO_2(110) surface 8

1.3. Thin Al_2O_3 films grown on Ni_3Al (111) 14

1.3.1 Growth of an ultrathin layer of Al_2O_3 on Ni_3Al (111) and its structure 14

1.3.2 Applications of ultrathin films Al_2O_3 grown on Ni_3Al(111) 15

1.3.3 Deposition of tetracene on Al_2O_3/Ni_3Al (111) 16

2. Experimental techniques 19

2.1 Synchrotron radiation 19

2.1.1 Synchrotrons 19

2.1.2 History of Synchrotrons 20

2.1.3 Properties of synchrotron radiation 22

2.1.4 Polarization of the synchrotron radiation 22

2.1.4. BESSY II 25

2.2 The X-ray photoelectron spectroscopy (XPS) 25

2.2.1 Principle of XPS 25

2.2.2 Advantages of the synchrotron based XPS 28

2.3 Near edge X-ray absorption fine structure spectroscopy (NEXAFS) 29

2.3.1 Principle of NEXAFS 29

2.3.2 Molecular orbitals 30

2.3.3. NEXAFS sensitivity to molecular orbitals 32

2.3.4. Angular dependence of resonance intensities 33

2.3.5 Acquisition of the NEXAFS spectra 38
2.4. Low energy electron diffraction (LEED) 41
3. Experimental equipment 43
3.1 HE-SGM Beamline 43
3.1.1 Determination of the polarization factor of the HE-SGM beamline 45
3.2 NEXAFS/XPS endstation at HE-SGM beamline at BESSY II 47
3.3 Sample holders 50
3.4. Construction of the cooling system in the analysis chamber 51
3.5. NEXAFS detector 52
3.6. Processing of the NEXAFS spectra 54
4. calculations of NEXAFS spectra 58
4.1. StoBe package 59
4.1.1 Density functional theory 60
4.2. Examples of StoBe calculation for simple aromatic molecules in the gas phase 62
4.2.1 Example of StoBe calculations for complicated molecules in the gas phase 64
5. Study of Terephthalic acid adsorbed on rutile TiO_2(110) using NEXAFS spectroscopy 68
5.1. Theoretical simulation for the free TPA molecule using StoBe Package 69
5.2. Experimental study of terephthalic acid adsorbed on the rutile TiO_2(110) surface 70
5.3. Conclusion 74
6. Investigation OF Tetracene thin films on Al_2O_3/Ni_3Al(111) substrate 75
6.1. Simulation of the tetracene NEXAFS spectrum in the gas phase 76
6.2. Experimental part 78
6.3 Results for multilayer tetracene films 81
6.4. Results for monolayer tetracene films 84
7. NEXAFS/XPS study of azobenzene adsorbed on rutile TiO_2 (110) surface 90
7.1. Calculation of NEXAFS spectra for cis- and trans- isomers of azobenzene 91
7.2. Experimental results 94
7.3. Conclusion 100
Conclusions 102
References 104

Appendix A 113

Use of the StoBe package for the simulation of NEXAFS spectra of the free molecules on example of benzene: 113

Example of the StoBe input file for benzene molecule 118

TABLE OF FIGURES

Fig. 1.1: Crystallographic structures of TiO_2: (A) rutile; (B) anatase. 6
Fig. 1.2: Structure of TiO_2(110) surface. 6
Fig. 1.3: Single crystals of rutile annealed at different temperatures and time: 1 – 19 h at 1273 K; 2 - 21 h 40 minutes at 1450 K, after reoxidation in the air at 1450 K; 3- 4 h 55 minutes at 1450 K; 4 – annealed at 1450 K for 35 minutes; 5 - annealed for 1h 10 minutes at 1350 K. The Figure is taken from [10]. 8
Fig. 1.4: Model for formic acid adsorbed on rutile TiO_2(110). Formic acid dissociates at the surface with formation of two formate ions. Adopted from [7]. 10
Fig. 1.5: Model for bi-isonicotinic acid adsorbed on rutile TiO_2(110) adopted from [7]. . 11
Fig. 1.6: Adsorption configuration of terephthalic acid on rutile TiO_2(110) surface suggested by Tekiel et al. [25]. 12
Fig. 1.7: Adsorption configuration of terephthalic acid on rutile TiO_2(110) surface suggested by Watkins et al. [27]. 12
Fig. 1.8: A model of azobenzene interaction with rutile TiO_2(110) proposed by Li et al. Adopted from [28]. 13
Fig. 1.9: Ni_3Al unit cell. 14
Fig.1.10: LEED pattern of clean Ni_3Al(111) (a), and Al_2O_3/Ni_3Al(111) (b) reproduced from [33]; (c) Model of the Ni_3Al(111) surface taken from [34], (d) one of the proposed models of Al_2O_3 thin films grown on Ni_3Al(111) [35]. 15
Fig.1.11: Models of tetracene thin films as suggested by Sokolowski [43] (left) and Soubatch [45] (right) as deposited (a), after annealing to 280 K with subsequent cooling to 100 K (b). 18
Fig. 2.1: Simplified schematic view of a synchrotron. 20
Fig. 2.2: E_σ and E_π components of the electrical vector of the linear polarized synchrotron radiation. 23
Fig. 2.3: The intensities of electrical vector components I_π and I_σ versus opening angle ψ theoretical (lines) and experimental (points) [51]. 24
Fig. 2.4: Synchrotron facility BESSY II in Berlin: schematic view (left) and real view from the top (right). Copied with modifications from BESSY II webpage [52]. 25
Fig. 2.5: Principle of XPS 27
Fig. 2.6: Standard geometry of the XPS experiment at the HE-SGM beamline. 27
Fig. 2.7: Scheme of the X-ray absorption process. 29
Fig.2.8: The MO diagram of the hydrogen molecule. Two 1s atomic orbitals form two σ molecular orbitals. 31
Fig. 2.9: MO diagram for benzene. 31
Fig. 2.10: Diatomic subunit with corresponding 1s→π* and 1s→σ* transitions and typical NEXAFS spectrum profile. Modified from [55]. 33
Fig. 2.11: Coordination system of the NEXAFS experiment. The direction of π* or σ* molecular orbitals is defined by the vector O, which is defined by polar angle α and azimuthal angle ϕ. 35

Fig. 2.12: NEXAFS spectra obtained for HOPG measured using standard geometry for various incidence angles θ varying from 30^0 to 90^0. 37
Fig. 2.13: Photon penetration depth D (depends on absorption coefficient μ and radiation incidence angle θ) and inelastic mean free pass L of Auger electrons. Adopted from [56] 38
Fig. 2.14: Energy level diagram and schematic photoemission spectra for different photon energies. Solid sample containing atoms with two core levels adsorbate A and substrate B [56]: (a) $h\nu_1$ below excitation threshold of core level of shell A; (b) $h\nu_2$ just above the absorption threshold of shell A. (c) $h\nu_3$ above the absorption threshold of shell A. 39
Fig.2.15: Typical LEED experiment. 42
Fig.2.16: The simplest approximation model for the LEED experiment. 42
Fig. 3.1.: Schematic view of HE-SGM beamline [52] 43
Fig. 3.2.: Flux curves for various monochromator gratings [52]. 44
Fig. 3.3 Transmission curve measured on the gold wafer after oxygen plasma treatment of the HE-SGM beamline components. 44
Fig. 3.4.: Two geometries used in the experiment for determination of the polarization degree on HE-SGM beamline. (a) standard geometry (only $E_{\parallel}$ component contributes to the spectrum), (b) special geometry (only $E_{\perp}$ component contributes to the spectrum). 46
Fig. 3.5.: Sample in the analysis chamber placed in the special geometry (only $E_{\perp}$ component of electrical vector contributes to the spectrum). 46
Fig. 3.6.: NEXAFS C K-edge spectra measured for HOPG in standard geometry (only $E_{\parallel}$ component contributes to the spectrum), and special geometry (only $E_{\perp}$ component contributes to the spectrum). 47
Fig. 3.7.: NEXAFS/XPS system 1-load lock chamber, 2-preparation chamber, 3-evaporators, 4-LEED system, 5-analysis chamber, 6-electron analyzer Scienta 3000, 7-distribution chamber, 8-park station from [57]. 49
Fig. 3.8.: NEXAFS/XPS endstation attached to HE-SGM beamline. 49
Fig. 3.9.: View of the sample holders which are used on the station: A - standard sample holder (no heater), B - sample holder with a resistive heating, C - sample holder with electron bombardment heating (copied from PREVAC manual). 50
Fig. 3.10.: Schematic view of the sample holder (redrawn with modification from PREVAC manual). 50
Fig. 3.11.: Schematic view of the cooling system in the analysis chamber (PREVAC manual). 51
Fig. 3.12.: Results of the cooling test with liquid helium supported with nitrogen cooling. 52
Fig. 3.13.: Schematic view of NEXAFS detector. 53
Fig. 3.14.: Schematic view of the NEXAFS measurement. 54
Fig. 3.15.: Flow diagram of the NEXAFS spectra processing procedure. 57

Fig. 4.1.: Simulated C K-edge NEXAFS spectra computed using StoBe for different free molecules: benzene, aniline, fluorobenzene. 63
Fig. 4.2.: TATA platform cation (left). TATA platform cation functionalized with azobenzene in trans isomerization (right). 65
Fig. 4.3.: Different components of the TATA cation functionalized with azobenzene (left). Simulated C K-edge NEXAFS spectrum of the TATA platform functionalized with azobenzene in trans-isomerization. Presentation of the contribution from the different components of the molecule. 65
Fig. 4.4.: Comparison of simulated C K-edge NEXAFS spectra of the TATA platform functionalized with azobenzene in cis- and trans- isomerization with the experimental C K-edge NEXAFS spectrum of the same system on Au (111) measured at 55 degrees 66
Fig. 4.5.: Comparison of simulated N K-edge NEXAFS spectra of TATA platform functionalized with Azobenzene in cis- and trans- isomerization with the experimental N K-edge spectrum for the same system on Au (111) measured at 55 degrees. 67
Fig. 5.1.: StoBe-simulated C K-edge NEXAFS spectrum of TPA in the gas phase. 69
Fig. 5.2.: NEXAFS spectra: (left panel) the TPA/TiO_2(110) system for different TPA coverages at an incident angle of $\theta = 20°$. The signal around the C K absorption edge is multiplied by a factor of 10, and the curves for 0.5 and 1 ML are shifted for clarity; (right panel) C K-/Ti $L_{2,3}$- intensity ratio dependence on deposition time. 72
Fig. 5.3.: C K-edge NEXAFS spectra for TPA on TiO_2: (a) 1.0 ML of TPA (left panel) and 0.07 ML of TPA (right panel); (b) difference of the NEXAFS spectra measured at $\theta = 90°$ and $\theta = 20°$ (linear dichroism). 73
Fig. 6.1.: StoBe simulation for the free tetracene molecule: (A) calculated total NEXAFS spectrum for free tetracene molecule, (B) Calculation of the C 1s→LUMO, LUMO+1… LUMO+n transitions for each nonequivalent atom. 77
Fig. 6.2.: StoBe simulation for free tetracene molecule compared with experimental result obtained for the tetracene adsorbed on Ag (111). 78
Fig. 6.3.: LEED patterns: clean Ni_3Al (111) surface (left), oxidized Ni_3Al (111) surface (right); images were taken at 93 eV primary energy. 79
Fig. 6.4.: XPS data recorded for the oxidized Ni_3Al (111) surface measured at different electron take-off angles. Excitation energy 400 eV. 80
Fig. 6.5.: XPS data for Tc multilayer coverage measured@100 K: (a) C1s directly after Tc deposition (black) , after annealing to 280 K (red); (b) Al2s, Ni3s after Tc deposition (black) , after annealing to 280 K (red); 83
Fig. 6.6.: C K-edge NEXAFS spectra for multilayer measured@100 K: directly after Tc deposition (solid lines), after annealing to 280 K (dashed lines). 83
Fig. 6.7.: The angle dependence of the first π^* resonance intensity recorded for the tetracene monolayer before and after annealing (green triangles and red diamonds respectively) and multilayer before annealing (blue squares) with corresponding fitting curves 84

Fig. 6.8.: XPS data for Tc monolayer coverage measured@100 K: (a) C1s directly after Tc deposition (black) , after annealing to 280 K (red); (b) Al2s, Ni3s lines after Tc deposition (black) , after annealing to 280 K (red); 85
Fig. 6.9: C K-edge NEXAFS spectra for monolayer: (a) before annealing to 280 K and measured@100 K; (b) after annealing to 280 K measured@100 K. 86
Fig. 7.1.: Azobenzene in trans- (a) and cis- configuration (b). 90
Fig. 7.2.: Simulated C K-edge NEXAFS spectrum of azobenzene in trans- configuration. 92
Fig. 7.3.: Comparison of simulated C K-edge (a) and N K-edge (b) NEXAFS spectra of azobenzene in cis- and trans- configuration with experimental spectra of azobenzene measured at 55 degrees. The photon energy scale of the StoBe simulated spectra was shifted 1 eV in the direction of low photon energies. 93
Fig. 7.4.: Calculated C K-edge NEXAFS spectrum (a) and N K-edge NEXAFS spectrum (b) of free aniline molecule. 94
Fig. 7.5.: Scheme of the sublimation set-up.....94
Fig. 7.6.: LEED image of the freshly prepared rutile TiO_2(110) surface measured at 109 eV (a), model of the same LEED image (b). 95
Fig. 7.7.: C K-edge NEXAFS of azobenzene adsorbed on rutile TiO_2(110) at different incidence angles recorded at 100 K. 96
Fig. 7.8.: N K-edge NEXAFS spectra of azobenzene adsorbed on rutile TiO_2(110) at different incidence angles recorded at the temperature 100 K. 97
Fig. 7.9.: NEXAFS N K-edge spectra of azobenzene adsorbed on rutile TiO_2(110) measured in the temperature range of 126 - 210 K and at 55 ° radiation incidence...97
Fig. 7.10.: NEXAFS C K-edge spectra of azobenzene adsorbed on rutile TiO_2(110) at 100 K after heating to 290 K. 98
Fig. 7.11.: XPS of Ti2p (a) and O1s (b) lines of azobenzene monolayer adsorbed on rutile TiO_2(110). 99
Fig. 7.12.: XPS of C1s and N1s lines of azobenzene monolayer adsorbed on rutile TiO_2(110). 100

LIST OF ABBREVIATIONS

a.u.	arbitrary units
AEY	Auger electron yield
AFM	atomic force microscopy
DFT	density functional theory
HE-SGM	high energy spherical grating monochromator
HOPG	highly ordered pyrolytic graphite
HREELS	high resolution electron energy loss spectroscopy
LCAO	linear combination of atomic orbitals
LEED	low-energy electron diffraction
LUMO	lowest unoccupied molecular orbital
MCP	microchannel plate
ML	monolayer
MO	molecular orbitals
NEXAFS	near edge X-ray absorption fine structure spectroscopy
PEY	partial electron yield
SAM	self-assembled monolayers
SCF	self-consistent field
STM	scanning tunneling microscope
TATA	triazatriangulenium
TDM	transition dipole moment
TEY	total electron yield
TPA	terephthalic acid
TPD	thermal programmed desorption
UHV	ultra-high vacuum
XPS	X-ray photoelectron spectroscopy

NOTATION LIST

E	electron energy
m	particle mass
c	velocity of light
R	the trajectory radius
$\boldsymbol{E}$	electric field vector
I	intensity of electromagnetic field
h	Planck constant
ϕ	Work function
F	Frequency
e	unit vector of electric field
σ_x	absorption cross section
O	transition dipole moment
W	power of electromagnetic radiation
Ψ	wave function
P	polarization factor
λ	Wavelength
$n(\mathbf{r})$	density of electrons at a point in space

1. INTRODUCTION

Nanoscience, the study of materials behavior on the nanometer scale, is considered to be one of the most promising research directions in the 21th century. Being a multidisciplinary field, nanoscience involves the collaborative effort of scientist practicing conventional disciplines like chemistry, physics, material science, biology and engineering. Surface science is a field of nanoscience, which concentrates on the study of physical and chemical phenomena occurring at the interface of two phases. Modern surface science includes such concepts as heterogeneous catalysis, semiconductor device fabrication, fuel cells, self-assembled monolayers, adhesives, etc.

One of the research goals of surface science is to probe and understand chemical reactions on well-defined, single crystalline surfaces at the molecular level for the needs of heterogeneous catalysis. The detailed understanding of these surface phenomena will help to develop and improve effective catalysts on the industrial scale.

Another field for which surface science studies are relevant is organic electronics. This field of materials science involves the use of small organic semiconducting molecules for the formation of electronic devices, in contrast to traditional electronics, which is based on inorganic conductors and semiconductors like copper and silicon. Over the last years, this field has attracted a huge interest from the scientific communities and the tremendous progress in the fabrication and design of organic electronic devices has been achieved. Today organic electronics is considered to be one of most promising technologies that can bring revolutionary improvements to human life.

This experimental thesis is dedicated to the study of organic species interacting with metal oxide single crystal surfaces using different types of photoelectron spectroscopy.

The surfaces of metal oxides play a crucial role in an extremely wide range of phenomena, including environmental degradation, organic electronics and catalysis. Metal oxides are the most common supports for dispersed metal catalysts, and in certain cases they can have a profound effect on the chemisorption and catalytic properties of the supported metal particles.

This thesis consists of seven chapters. Chapter 1 provides a review on metal oxides and previous works on functionalization of metal oxide surfaces with organic molecules. Chapter 2 is devoted to the experimental methods used in this work. The experimental equipment is described in Chapter 3. Chapter 4 is dedicated to the calculation of the NEXAFS spectra of the free molecules using StoBe package. Chapters 5-7 describe the experimental results obtained during the spectroscopic studies of three different systems: terephthalic acid on rutile TiO_2(110), azobenzene on rutile TiO_2(110) and tetracene on Al_2O_3/Ni_3Al(111).

1.1. Metal Oxides

Oxides are a very diverse and extensively studied class of compounds. The electronegativity of oxygen facilitates the formation of stable chemical bonds with almost all elements to yield the corresponding oxide. Most metals readily oxidize under ambient conditions, therefore the abundance of metal oxides in nature is also high. The variety of different chemical and physical properties of metal oxides such as optical, magnetic or electronic properties provides broad research opportunities for chemistry, material science and physics. Metal oxides have found a lot of applications in different industrial branches including thin film technology, protective coating, and gas sensors. Oxides also play a key role in heterogeneous catalysis being an active catalyst as well as a support for metal

clusters. Due to the variety of surface sites and complexes as well as the ability of the surface metal cations to exist in many different oxidation states, metal oxides provide a broad range of selectivities and activities [1].

The fundamental understanding of heterogeneous catalysis phenomena requires theoretical and experimental knowledge about structures and properties of metal oxide surfaces as well as comprehension of their interaction with different chemical species such as molecules or metal clusters. The surface science of metal oxides is a very rapidly developing field. Different surfaces of oxide single crystals, in particular semiconducting TiO_2, ZnO as well as isolating Al_2O_3, SiO_2, MgO, are extensively studied by different research groups using multiple techniques and approaches.

Together with single crystal surfaces, also metal oxide thin films grown on different substrates are being extensively studied. Owing to their isolating or semiconducting nature, most metal oxides are difficult to investigate using surface science techniques, which usually require a sufficient electrical conductivity of the sample. To overcome this experimental problem, very thin epitaxial films of metal oxides can be grown on a suitable conducting substrate. Such films will retain most properties of oxide single crystal surface and at the same time will be sufficiently conductive to enable the use of surface science techniques. These epitaxial films can be grown by metal evaporation in oxygen atmosphere on different metal substrates or as a result of surface oxidation under ultra-high vacuum (UHV) conditions. The interest in ultrathin metal oxide films shows a steady growth due to the many potential applications. An example of such oxide films can be TiO_2 ultrathin films on different substrates [2-4]. Some attempts to develop electronic devices based on ZnO ultrathin films are also known in the literature [5]. Another example is Al_2O_3 thin films, which found numerous applications as a support for

heterogeneous catalysis or a substrate for adsorption of organic species [33-35].

Since in this thesis the interaction of organic molecules with rutile TiO_2(110) and ultrathin Al_2O_3 film on Ni_3Al(111) was investigated, these two metal oxides are reviewed in detail.

1.2. Titanium dioxide

For many years TiO_2 has been considered to be one of the most investigated metal oxides attracting attention of researchers from all over the world [6,7]. This can be explained by the large number of potential applications including solar cells production, gas sensors, catalysis, and fabrication of medical implants [6-9]. Presently, research in this field centers on two main topics: synthesis of novel TiO_2 based structures and fabrication of new devices like solar cells and fundamental research on different TiO_2 single crystal surfaces at the atomic scale, including reactions of adsorbates on the surfaces. The aim of these experimental and theoretical studies is to obtain the fundamental understanding of the titania surface interaction with different adsorbates like metal atoms or organic molecules. The chemical reactions occurring on TiO_2 single crystal surfaces are studied both experimentally usually under UHV conditions and theoretically applying different approaches of theoretical chemistry, in particular the density functional theory (DFT).

The TiO_2 topic is quite well covered in the literature. The most thorough and comprehensive review on TiO_2 bulk structures and TiO_2 single crystal surfaces has been provided by Diebold [7]. In addition, there are a few more focused reviews [8, 9]. Based on the above mentioned publications and references therein, a small review summarizing a current state of knowledge about adsorption of organic molecules on TiO_2 single crystal

surfaces is presented below.

1.2.1 Structure of TiO_2 crystal

TiO_2 exists in three different modifications: rutile, anatase, and brookite. Rutile has a tetragonal unit cell (D_{4h}^{14} - $P4_2/mnm$, $a = b = 4.58\text{Å}, c = 2.953\text{Å}$), anatase has a tetragonal unit cell (D_{4h}^{19} - $I4_1/amd$, $a = b = 3.782\text{Å}$ $c = 9.502\text{Å}$) and brookite a rhombohedral unit cell (D_{2h}^{15} - Pbca, $a = 5.436\text{Å}$, $b = 9.166\text{Å}$, $c = 5.135\text{Å}$) [7,9]. In addition to rutile, anatase and brookite, three metastable phases of TiO_2 can be produced synthetically (monoclinic, tetragonal and orthorombic). Additionally, five high pressure phases (α-PbO_2-like, baddeleyite-like, cotunnite-like, orthorhombic, and cubic) are known. Among all these modifications, however, only rutile and anatase are widely used in surface science and most studies involve these two modifications. The crystallographic structures of rutile and anatase are presented in Fig. 1.1.

1.2.2 Rutile TiO_2 surface

For the rutile modification, the thermodynamic stability of (110), (001), (100) surfaces has been investigated both theoretically and experimentally. It was shown that the TiO_2(110) is the most stable and most investigated one, therefore it is often used as a model system [6-9]. A ball model of the rutile TiO_2(110) is presented in Fig. 1.2. This surface consists of Ti_{5c} five-fold coordinated atoms extending along [001] direction. The rows of twofold coordinated O_{2c} atoms, also known as bridge-bonded oxygen, separate rows of titanium atoms. In terms of the Lewis acid-base concept Ti_{5c} atoms can be regarded as Lewis acid sites for the adsorption of lone-pair molecules, while oxygen atoms are the Bronsted base capable accepting hydrogen atoms from the adsorbates [6].

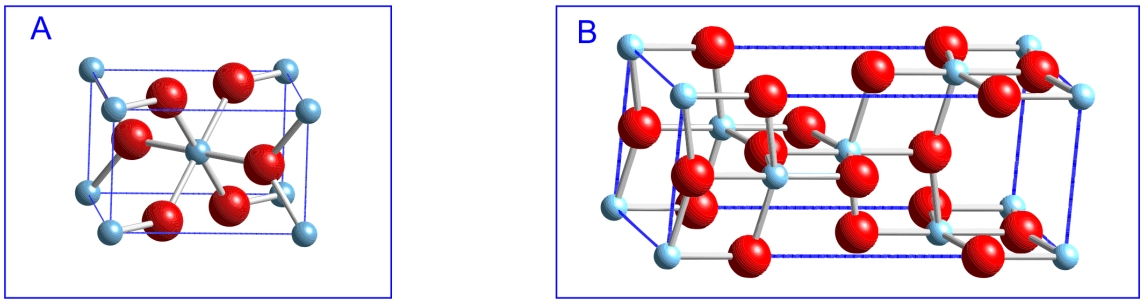

Fig. 1.1: Crystallographic structures of TiO_2: (A) rutile; (B) anatase.

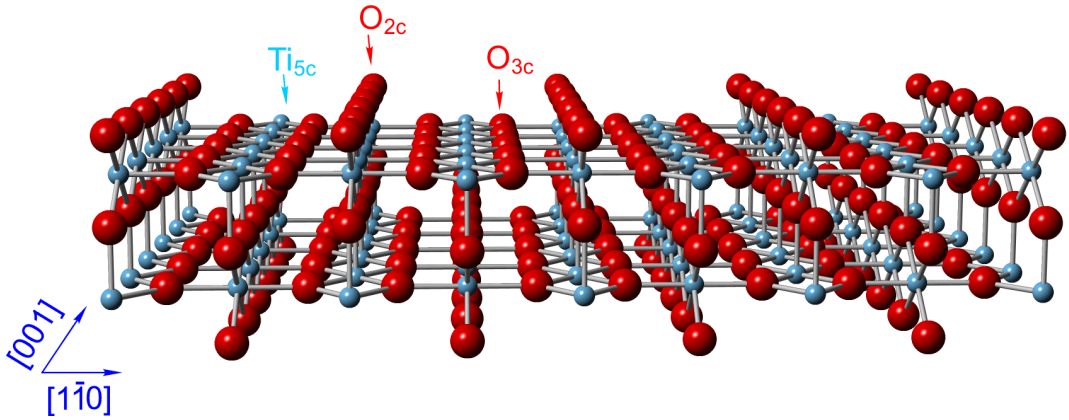

Fig. 1.2: Structure of TiO_2(110) surface.

1.2.3 Surface structure of stoichiometric, reduced and reoxidized rutile TiO_2(110)

After a typical UHV cleaning procedure which consists of argon sputtering and heating cycles, the rutile TiO_2(110) surface exhibits a (1×1) structure as has been demonstrated by many LEED and STM studies (see [7] and references provided therein). The typical heating temperature is around 900 K. Higher temperatures may lead to the loss of oxygen and surface reduction. The optimal preparation parameters like argon pressure, accelerating voltage of the sputter gun may depend on the dimensions of the UHV chamber, the construction of the sample holder, the type of the sputter gun, the distance from the sputter gun to the sample etc, but typically the argon pressure was ~$1x10^{-4}$ mbar and accelerating voltage 1 kV. Two methods, low-energy electron diffraction (LEED) and X-ray photoelectron spectroscopy (XPS), were used for the

surface quality control. XPS was mainly used to control the amount of carbon impurities as well as the stoichiometry of the surface and to determine Ti oxidation states.

The TiO_2(110) single crystal surface can be easily reduced by heating it above 900 K, as the oxygen is lost, the surface becomes more metallic and Ti atoms can exist in a number of oxidation states. The reduction of the crystal is accompanied by a crystal color change: the stoichiometric rutile crystal is transparent, however upon annealing at elevated temperature the number of oxygen vacancies is increased and optical properties are changed. The appearance of TiO_2 crystal varies from light blue and transparent (stoichiometric crystal) to more dark blue (partially reduced crystal), and finally black and opaque for fully reduced crystals. A detailed study of the rutile crystal color change with increasing annealing temperature was performed by Li [10]. Pictures taken for rutile TiO_2(110) single crystals annealed in a high temperature oven at different temperatures are presented in Fig. 1.3. The reduced rutile TiO_2(110) surface can be reoxidized by exposure to oxygen gas at elevated temperatures. Typically the reoxidation leads to (1×2) surface reconstruction with formation of additional oxygen rows. This reconstruction is explained by Ti interstitials diffusing to the surface at elevated temperatures and formation of additional Ti_xO_y structures [7-9].

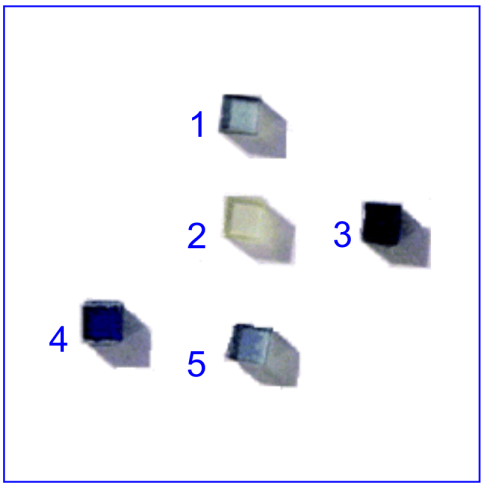

Fig. 1.3: Single crystals of rutile annealed at different temperatures and time: 1 – 19 h at 1273 K; 2 - 21 h 40 minutes at 1450 K, after reoxidation in the air at 1450 K; 3- 4 h 55 minutes at 1450 K; 4 – annealed at 1450 K for 35 minutes; 5 - annealed for 1h 10 minutes at 1350 K. The Figure is taken from [10].

1.2.4 Interaction of organic molecules with rutile TiO_2(110) surface

Adsorption of acenes. The interaction between acenes and TiO_2(110) surface was studied by Reiss in the context of his PhD project [11]. In reference [12] Reiss et al. presented a study about benzene, naphthalene, and anthracene adsorbed on the TiO_2(110) surface with near-edge X-ray absorption fine structure spectroscopy (NEXAFS), XPS and temperature programmed desorption (TPD). The interpretation of the data was aided by ab initio calculations of the molecular adsorption geometry. It was shown that all three molecules adsorb in a preferably flat configuration with a tilt angle between 24° and 28°. It was also found that the interaction between adsorbate and substrate is weak compared to that between benzene and transition metal surface [11, 12].

Adsorption of pyridine. The adsorption of pyridine (C_5H_5N) on rutile TiO_2(110) surface was reviewed in [9]. Earlier, pyridine was generally considered to be a Lewis base with its N atom acting as an electron donor and accordingly, the formation of weak N-Ti bond was expected [9, 13]. However, the results of this study were inconsistent with

previous observations. The determination of the adsorbate orientation showed that pyridine adsorbs with its ring parallel to the surface analogous to benzene. Moreover, STM, TDS and XPS studies revealed that pyridine is physisorbed on the rutile TiO_2(110) surface [13]. The XPS N 1s line of pyridine showed no shift and TDS revealed the absence of N-Ti bond. A further atomically resolved STM study of the rutile TiO_2(110) surface showed that the molecules are rather mobile on the surface and preferably attach to four-fold coordinated Ti atoms at step edges [14].

Adsorption of acids. A large number of papers [15-22] on rutile TiO_2(110) functionalization are devoted to the adsorption of different carboxylic acids. Formic acid (HCCOH) is one of the most frequently studied organic adsorbates on rutile TiO_2(110) [7]. The system was studied using a large variety of different techniques including NEXAFS, scanning tunneling microscopy (STM), atomic force microscopy (AFM), high resolution electron energy loss spectroscopy (HREELS), and DFT calculations [15-17]. It was found that formic acid dissociates on a rutile TiO_2 surface. The formate ion resulting from the proton abstraction binds to two fivefold coordinated Ti atoms in a bi-dentate fashion. The adsorption geometry of the dissociation products was determined by X-ray diffraction and NEXAFS. A model for formic acid adsorbed on rutile TiO_2(110) is presented in Fig. 1.4.

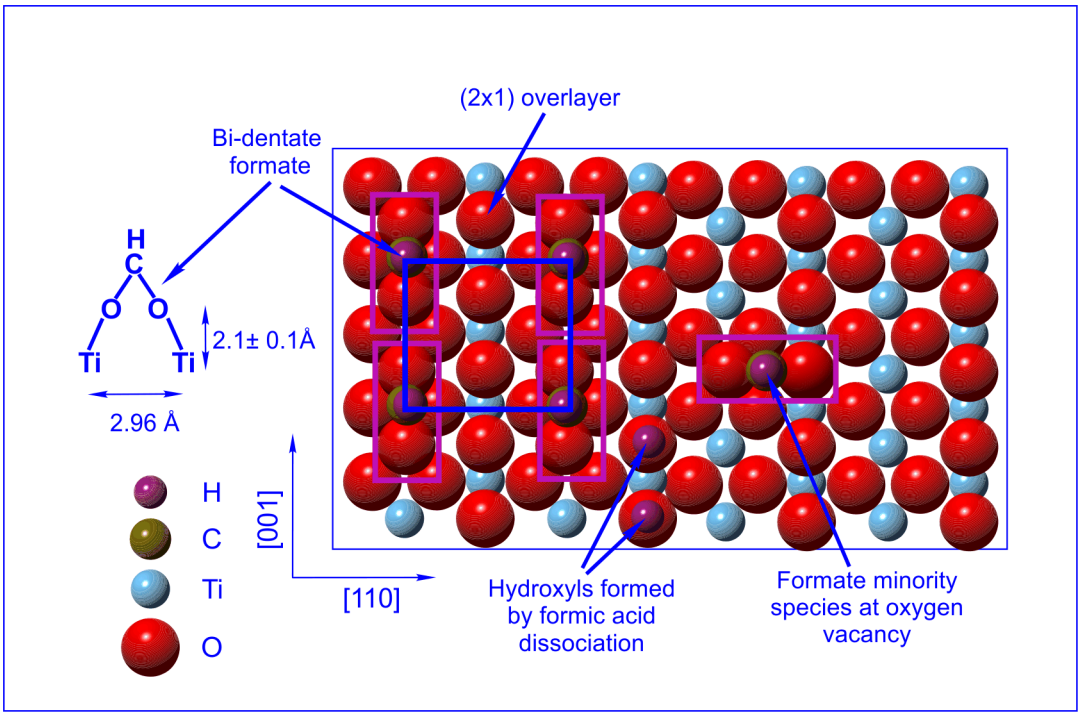

Fig. 1.4: Model for formic acid adsorbed on rutile TiO_2(110). Formic acid dissociates at the surface with formation of two formate ions. Adopted from [7].

The behavior of acetic acid on rutile TiO_2(110) is similar to that of formic acid. At room temperature, acetic acid adsorbs on TiO_2(110) in the form of acetate ions H_3CCOO^- in a (2x1) structure with the two O atoms bonded in a bridging (bi-dentate) configuration across two fivefold coordinated Ti atoms with the C–C bond perpendicular to the surface. This puts the H atoms in the methyl group parallel to the surface plane [18-20]. Adsorption of benzoic acid (C_6H_5COOH) at room temperature was studied by electron stimulated desorption in ion angular distributions, LEED as well as by STM. It was found that this organic acid adsorbs in a dissociative fashion with the two oxygen atoms bridge-bonded to fivefold coordinated Ti atoms [20]. STM data indicate on dimerization of the benzoate rings along the [110] direction.

The adsorption of a more complex organic acid, bi-isonicotinic acid (2,2'-bipyridine-4,4'-dicarboxylic acid), was studied with XPS/NEXAFS supported by theoretical calculations [21, 22]. The proposed adsorption model is similar to that of

formate and benzoate**;** a bi-isonicotonic acid molecule binds to two neighboring Ti rows through the dehydroxylated oxygen atoms. The proposed adsorption geometry, derived from the calculations and consistent with the experimental data, is shown in Fig. 1.5. N1s NEXAFS spectra were successfully modeled in a cluster model using this adsorption geometry [22].

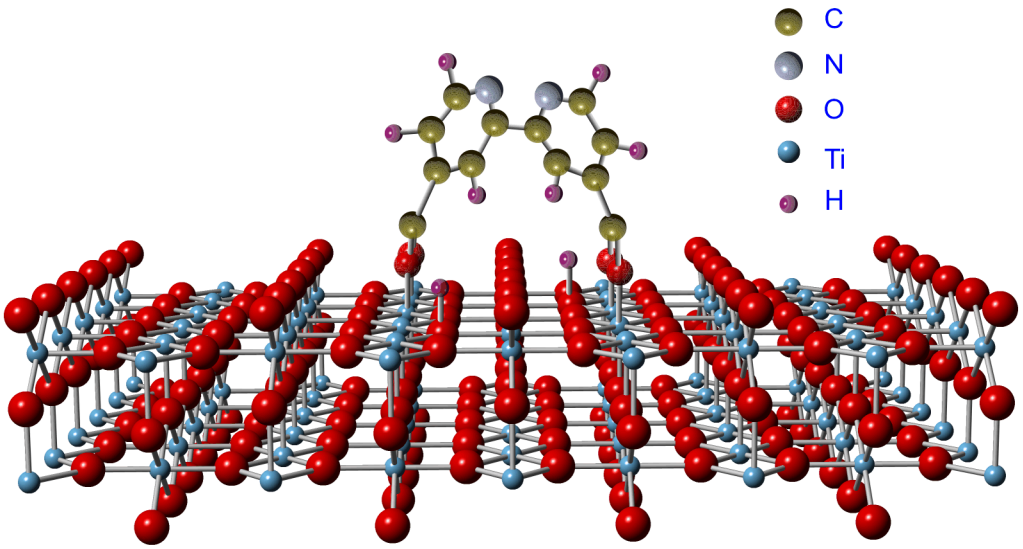

Fig. 1.5: Model for bi-isonicotinic acid adsorbed on rutile TiO_2(110) adopted from [7].

One of the most promising systems for metal oxide surface functionalization is terephthalic acid (TPA, $C_6H_4(COOH)_2$). Terephthalic acid is a molecular linker which has received considerable attention as a linking component for metal organic frameworks [23]. The functionalization of the TiO_2(110) surface with TPA may result in the formation of a layer of upright oriented carboxyl terminated molecules. This kind of structure may find an application similar to carboxyl-terminated self-assembled monolayers (SAMs) [24]. Tekiel et al. studied the structure of a complete monolayer of TPA on TiO_2(110) by means of scanning tunneling microscopy (STM) and non-contact atomic force microscopy (NC-AFM) [25, 26]. The STM study suggested that, at a coverage of one monolayer the TPA molecules are oriented up-right on the TiO_2(110)

surface with a formation of dimer rows along the [001] direction. However, direct evidence of this up-standing orientation was not presented in this publication. In contrast, theoretical calculations based on DFT theory presented in the paper by Watkins et al. [27] suggested that the molecule lies flat on the surface. The models suggested by Tekiel and Watkins are presented in Fig. 1.6 and Fig. 1.7, respectively.

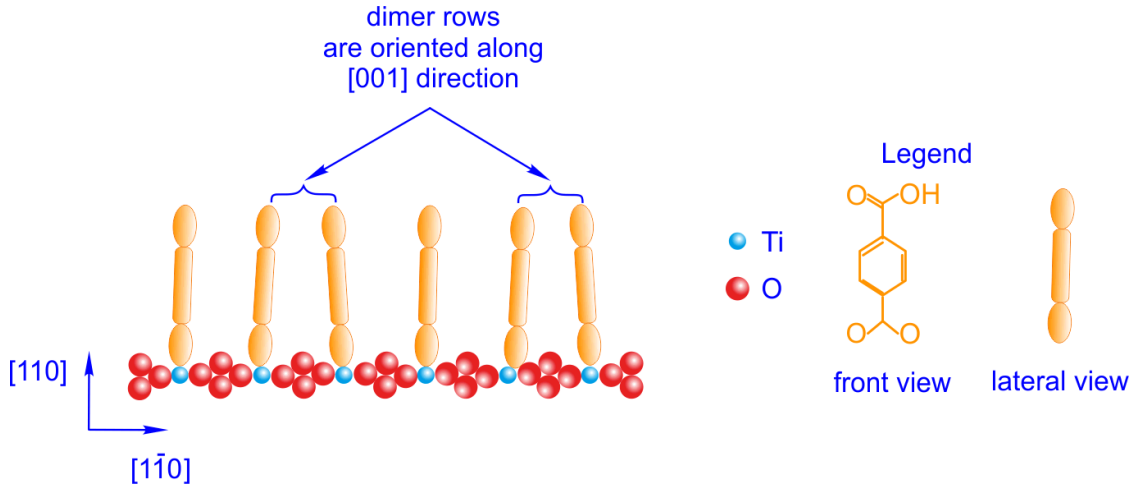

Fig. 1.6: Adsorption configuration of terephthalic acid on rutile TiO_2(110) surface suggested by Tekiel et al. [25].

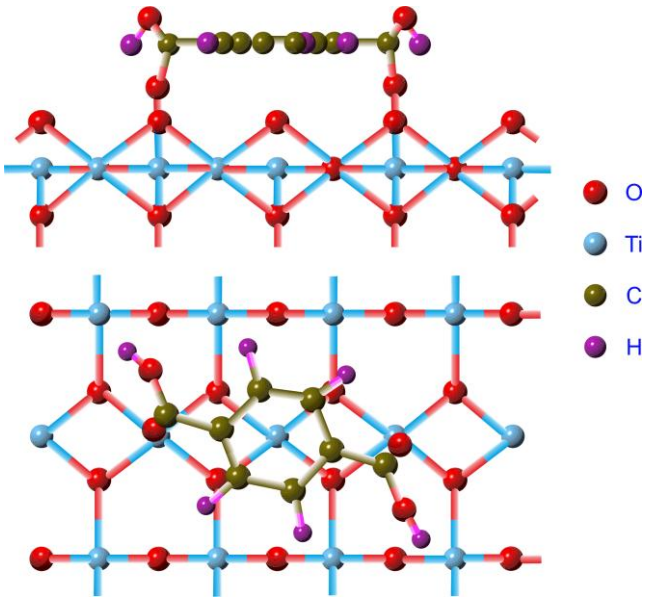

Fig. 1.7: Adsorption configuration of terephthalic acid on rutile TiO_2(110) surface suggested by Watkins et al. [27].

Azobenzene on rutile TiO_2 (110). Interaction of azobenzene with the rutile TiO_2 (110) surface has been studied by Li et al. [28]. The experimental results presented in [29], were the starting point for this study, where TiO_2 was used as an active catalyst for the selective formation of aromatic azo compounds. The main motivation for the study [28] was to demonstrate on a single crystal surface that TiO_2 is capable of facilitating the catalytic reaction and therefore can be used for aniline synthesis. The adsorption of azobenzene was studied both on rutile and anatase surfaces at room temperature.

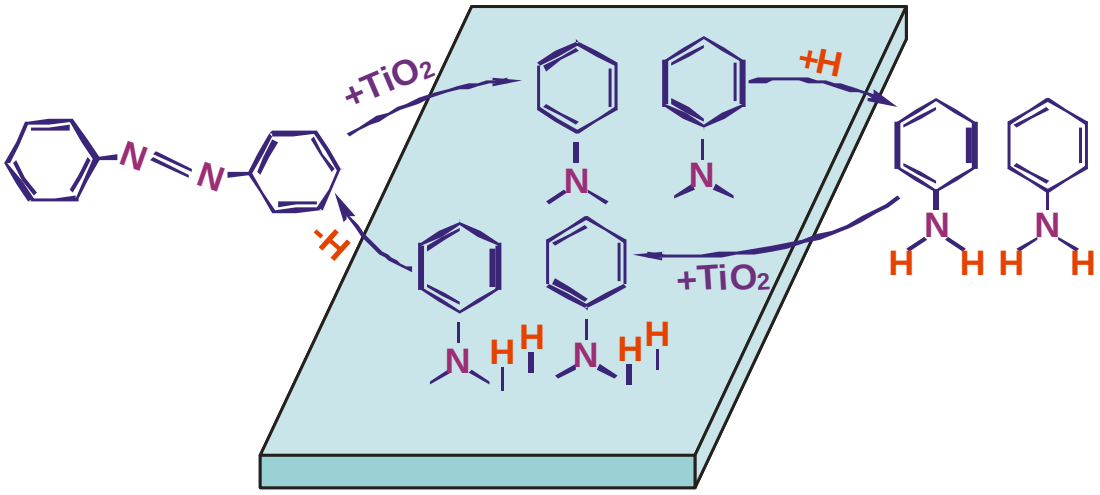

Fig. 1.8: A model of azobenzene interaction with rutile TiO_2(110) proposed by Li et al. Adopted from [28].

Results obtained from STM, XPS and LEED techniques provided evidence that the TiO_2 surface is capable of cleaving the N=N azobenzene double bond. As a result, the molecule dissociates, leading to the formation of phenyl imide (C_6H_5N) species at saturated coverage. STM studies performed on the anatase surface showed that, at very low coverage (0.02 ML), azobenzene remains intact and lies flat on the surface. The model of the proposed interaction of aniline/azobenzene with TiO_2 is presented in Fig.°1.8. These experimental results were also confirmed by theoretical calculations [30,31].

1.3. Thin Al_2O_3 films grown on Ni_3Al (111)

In recent years Al_2O_3 films grown on Ni_3Al (111) have received considerable attention (see [35] and references provided therein) due to the diversity of potential applications in different branches of science including heterogeneous catalysis and electronics. Below a small review concerning this system including its applications is provided.

1.3.1 Growth of an ultrathin layer of Al_2O_3 on Ni_3Al (111) and its structure

The elemental unit cell of Ni_3Al alloy is presented in Fig. 1.9. Its structure is a Cu_3Au type structure; in the cubic unit cell Al atoms occupy the corners, while Ni atoms are located in the center of each phase. The lattice constant as determined by using diffraction methods has a value of 3.5 Å [32].

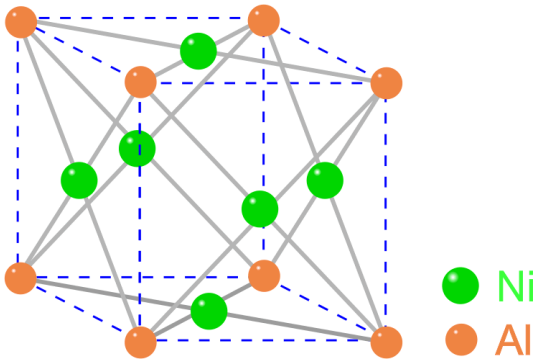

Fig. 1.9: Ni_3Al unit cell.

Ni_3Al (111) is commonly prepared by mechanical polishing and subsequent cleaning in vacuum using argon sputtering. The quality of the surface is monitored by XPS and LEED. The structure of the Ni_3Al(111) surface along with its corresponding LEED pattern obtained in one of the studies [33] is presented in Fig. 1.10 (a) and Fig. 1.10 (c), respectively. The oxide layer is usually prepared by exposing the clean surface to oxygen in UHV with a typical dosage of 40-80 L. In Fig. 1.10 (b) a LEED

pattern corresponding to the oxidized $Ni_3Al(111)$ surface is presented. Fig. 1.10 (d) represents one of the atomic models of oxide structure, as proposed in the literature [35].

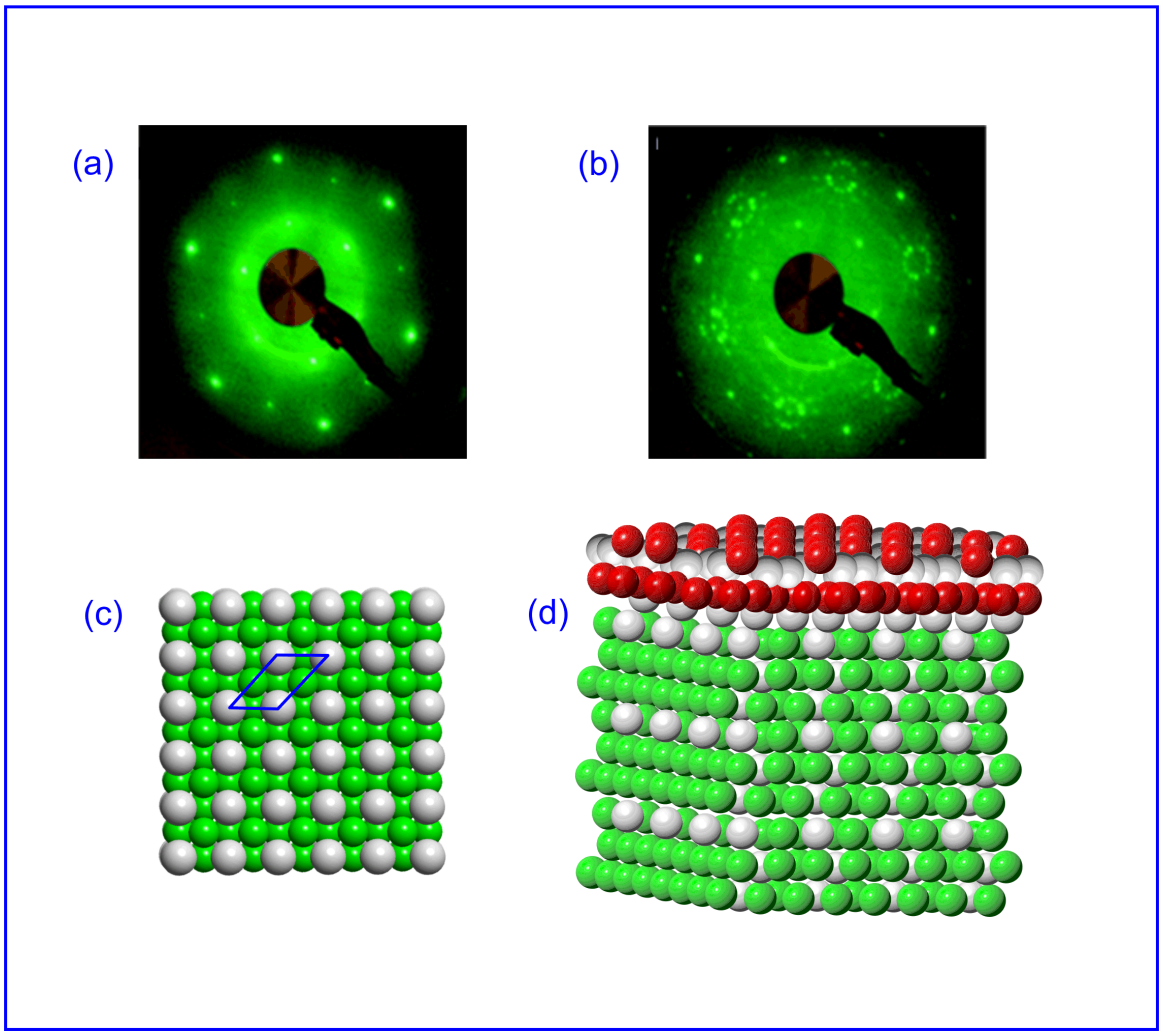

Fig. 1.10: LEED pattern of clean $Ni_3Al(111)$ (a), and $Al_2O_3/Ni_3Al(111)$ (b) reproduced from [33]; (c) Model of the $Ni_3Al(111)$ surface taken from [34], (d) one of the proposed models of Al_2O_3 thin films grown on $Ni_3Al(111)$ [35].

1.3.2 Applications of ultrathin films Al_2O_3 grown on $Ni_3Al(111)$

For several decades, ultrathin alumina films grown on $Ni_3Al(111)$ have gained enormous popularity, due to the large number of possible applications. In the first place, a detailed investigation of the system could be beneficial for pure fundamental research where the point of interest is the structure and other physical properties of Al_2O_3 surfaces.

It is necessary to mention that in contrast to the bulk Al_2O_3 crystal which is an insulator, ultrathin Al_2O_3 films allow studying the properties of alumina with techniques requiring electrically conductive samples [35]. The other potential application of Al_2O_3 thin film is microelectronics, where alumina films have received attention as potential replacements for SiO_2 as gate dielectric material in complementary metal oxide semiconductor (CMOS) technology [36]. $Al_2O_3/Ni_3Al(111)$ is a naturally nanostructured surface and it is an ideal template for the growth of inorganic and organic matter. The system has also found its applications in heterogeneous catalysis [35]. $Al_2O_3/Ni_3Al(111)$ can be used as a support for the preparation of well-ordered, equal sized metal nanoclusters deposited using vapor deposition. Ordered arrangement of such metal nanoclusters with a controllable size will definitely be a great achievement in the field of catalytic research [36]. In the literature there are a great number of publications, where metals like silver, manganese, copper and vanadium were deposited on $Al_2O_3/Ni_3Al(111)$ substrates [36-39].

One example of a systematic study of organic thin films grown on $Al_2O_3/Ni_3Al(111)$ is described by Casu et al. [40]. Mono- and multilayer of perylene grown on $Al_2O_3/Ni_3Al(111)$ was studied with NEXAFS spectroscopy. This investigation revealed the existence of different molecular orientations depending on the thin film growth parameters like deposition rate and substrate temperature. The result of this study is of relevance for the question whether perylene can be used in organic field effect transistors.

1.3.3 Deposition of tetracene on Al_2O_3/Ni_3Al (111)

Organic semiconductors attract considerable attention due to their promising potential as active material in the construction of electronic devices. The class of organic

semiconductors known as polyacenes, polycyclic aromatic hydrocarbons made up of linearly fused benzene rings, is especially interesting, because of the high charge carrier mobilities in their crystalline phase and, accordingly, there is a high potential for the fabrication of organic field effect transistors (OFETs) and organic light emitting diodes (OLEDs) [41]. One of them tetracene, also called naphthacene, is a polycyclic aromatic hydrocarbon. Tetracene is the four-ringed member of the series of acenes, the previous one being anthracene and the next one being pentacene. It has the appearance of a pale orange powder.

OLEDs are used to create digital displays in devices such as television screens, computer monitors, screens of mobile phones, etc. The control over the optical properties of the fluorescent organic layer plays a key role. Particularly, it concerns the problem of electronic coupling with substrate and optical quenching on metal surfaces [42-44]. The common way to isolate an organic layer from a conductive surface is a thin insulating barrier. Being an isolator, Al_2O_3 thin films grown on Ni_3Al can serve as isolation barrier between organic adlayers and surface and can control the fluorescent properties of adsorbed tetracene molecules. However, this method often fails. For instance, the luminescence of tetracene thin films deposited on $AlO_x/Ni_3Al(111)$ at low temperature was found to be quenched despite the presence of a thin insulating alumina layer. Surprisingly, fluorescence reappeared upon annealing at 280 K [44]. To explain the observed behavior, spot-profile-analysis low energy electron diffraction, (SPA-LEED) as well as XPS and high resolution electron energy loss spectroscopy, (HREELS) were recently used [45]. The results suggest that the tetracene layer undergoes a structural transformation upon postdeposition annealing: initially flat-lying molecules adopt an upright standing orientation. It was proposed that they form a compact organic layer which dewets and forms separate islands.

The optical properties of the interface are changed accordingly: if tetracene molecules are oriented parallel to the substrate surface, they retain an electronic coupling with Ni_3Al metal states due to extended π-orbitals oriented perpendicular to the molecular plane and, thus, partly penetrating through the thin alumina slab inducing optical quenching; contrary, if molecules adopt an upward direction, they become well-isolated from the metal substrate and show the luminescent properties of free tetracene. The structural models suggested in studies [43] and [45] are presented in Fig. 1.11. Although these simple models can explain the observed behavior, so far there is no direct evidence that the molecule reorientation is indeed responsible for the observed optical behavior.

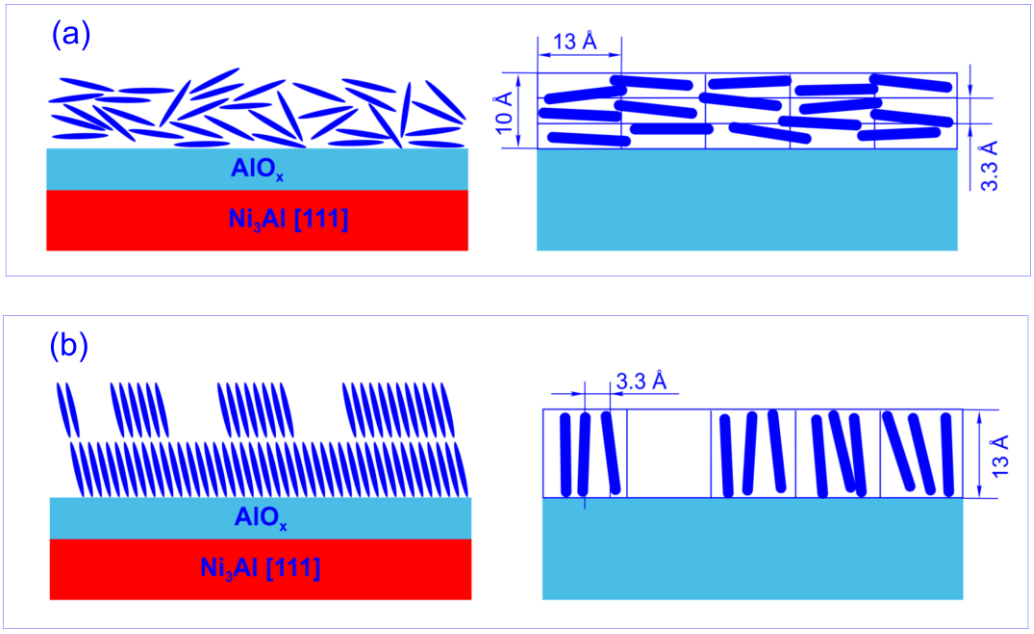

Fig.1.11: Models of tetracene thin films as suggested by Sokolowski [43] (left) and Soubatch [45] (right) as deposited (a), after annealing to 280 K with subsequent cooling to 100 K (b).

2. EXPERIMENTAL TECHNIQUES

Surface science, as any other research field, uses a set of techniques and approaches. Studies of surface properties involve both physical and chemical analysis under predefined and controlled conditions. The experiments are usually conducted in ultra-high vacuum (the pressure is about 10^{-10} mbar).

Spectroscopy plays one of the key roles in surface science research. It uses electromagnetic radiation of a broad spectral range to study the physical and chemical properties of surfaces. The experimental data presented in this thesis were acquired using X-ray photoelectron spectroscopy (XPS) and near edge X-ray absorption fine structure spectroscopy (NEXAFS). Low energy electron diffraction (LEED) was used as auxiliary method to asses the surface structure and quality. Since all experiments presented here were conducted using X-ray radiation obtained from the synchrotron source, a brief review covering properties of synchrotron radiation is provided.

2.1 Synchrotron radiation

2.1.1 Synchrotrons

A synchrotron is a machine where charged particles such as electrons, protons, etc are accelerated by electromagnetic fields and are forced to move on a confined circular orbit. The accelerated charged particles following the circular trajectory emit highly collimated electromagnetic radiation, called synchrotron radiation in tangential direction [46]. The simplest scheme of the synchrotron is presented in Fig. 2.1. The electrons emerging from the electron gun (1) are accelerated in two stages: in the first stage electrons are accelerated in the linear accelerator (2) to energies in the range of

Megaelectronvolts. In the second stage, they are accelerated to an energy range of Gigaelectronvolts in the booster (3). Then electrons enter the storage ring (4) where their kinetic energy is kept constant. When electrons pass through the strong magnetic field induced by the bending magnet, the synchrotron radiation is emitted tangentially to the electron orbit. The radiation propagates through the ports called beamlines (5) to the endstation (6), where it can be used for the various experiments. Synchrotrons of the third generation use also insertion devices such as wigglers and undulators to generate the radiation. In these cases the electrons are forced to move on a wavelike trajectory by a magnet array. The radiation produced this way has much higher brilliance and photon flux than that emerging from a bending magnet.

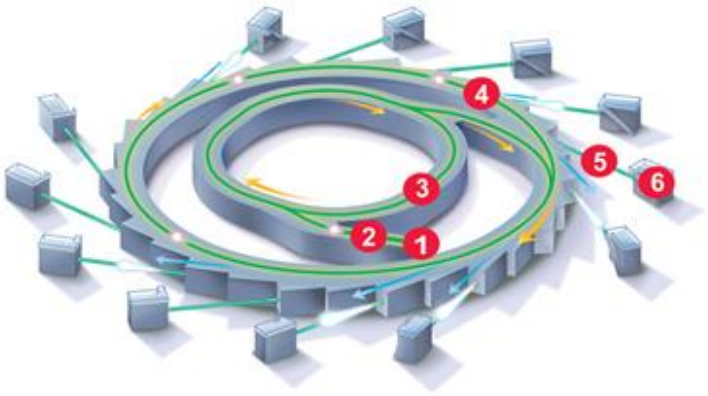

Fig. 2.1: Simplified schematic view of a synchrotron.

2.1.2 History of Synchrotrons

The history of the synchrotron radiation research starts in the 19th century. In 1873, James Clerk Maxwell postulated the theory of electromagnetism and changed the understanding of the light nature. In 1897, Larmor derived an expression for the instantaneous total power radiated by an accelerated charged particle. Liénard extended this result to the case of a relativistic particle undergoing centripetal acceleration in a

circular trajectory. The Liénard's formula predicts that the radiated power is proportional to $\frac{1}{R^2}\left(\frac{E}{mc^2}\right)^4$, where E is the particle energy, m is the rest mass, and R is the trajectory radius. Another important milestone was the discovery of X-rays by Röntgen in 1895. X-rays remain the main form of radiation produced by the synchrotrons until now [47,48]. A decade later in 1907, Schott reported his attempt to explain the discrete nature of atomic spectra by treating the motion of a relativistic electron in a homogeneous magnetic field. Schott managed to derive the expressions for the radiation angular distribution as a function of the orbital frequency harmonic. He wrote a book-length essay on the subject in 1912. In 1905 it was shown that X-rays passing through gas can be used for compositional analysis [49]. In 1912 Max Laue presented a break through work where X-ray radiation was used for determination of crystal structures [50]. The first synchrotron built in 1946 was used for the study of high energy particle collisions. It was also noticed that synchrotrons produce as a byproduct a very bright radiation which was considered as a problem for particle physics being the reason of major energy loss. The first experiments using synchrotron radiation were conducted in 1956 at Cornell University in the USA. Since then the electromagnetic radiation produced by synchrotrons originally built for the needs of the high energy particles study was used in a parasitic mode until 1980 when the first synchrotron dedicated especially for light experiments was built in the United Kingdom. Today, the synchrotron technique has become a unique tool to be used in many branches of science including material science, chemistry, biology, medicine, environmental science and others, with more than 50 light sources operating around the world.

2.1.3 Properties of synchrotron radiation

There are several properties which make synchrotron radiation unique and advantageous over X-ray radiation emitted from laboratory sources [49, 50]:

1. The brilliance of the X-rays produced by the synchrotron (~10^{15} photons/s·mrad^2·mm^2·0.1%BW, where BW is a bandwidth, for the 2nd synchrotron generation and ~10^{20} photons/s·mrad^2·mm^2·0.1%BW for the 3rd synchrotron generation) is several orders of magnitude higher than the brilliance of the radiation from the conventional laboratory X-ray source (~10^7 photons/s·mrad^2·mm^2·0.1%BW).

2. Synchrotron sources provide radiation in a continuous spectral range spreading from the near infrared up to the γ radiation.

3. Polarization of the synchrotron radiation.

4. Natural narrow angular collimation of the beam.

2.1.4 Polarization of the synchrotron radiation

As already mentioned above the polarization of the synchrotron radiation is a property which makes it distinguishable from that emitted by ordinary laboratory sources and is exploited in different synchrotron research techniques together with tunability of the radiation. Synchrotron radiation from the bending magnet has a linear polarization, however elliptical/circular polarization can be obtained using modern insertion devices like undulators. Most of experimental results presented in this thesis deal with NEXAFS spectroscopy which requires linearly polarized radiation. Since all the experiments were conducted at the beamline located on the bending magnet the properties of the synchrotron radiation emerging from the bending magnet are reviewed.

In Fig. 2.2 the electron forced to move on a circular trajectory by the applied magnetic field is presented. The radiation emitted tangentially to the electron orbit is suppressed in a narrow cone which is characterized by the vertical half-opening angle $\psi = mc^2/E$, where E is the electron energy. The direction of the wave propagation is defined by the wave vector k. The linear polarization is defined by two polarization vectors $\mathbf{E}_\sigma$ and $\mathbf{E}_\pi$. The $\mathbf{E}_\sigma$ component lies in the plane of the electron orbit. The $\mathbf{E}_\pi$ component is perpendicular to the $\mathbf{E}_\sigma$ component and is parallel to the external magnetic field vector $\mathbf{H}_0$. For the synchrotron radiation above and below the electron orbit ($\psi \neq 0$) both $\mathbf{E}_\sigma$ and $\mathbf{E}_\pi$ with a phase shift of $\pi/2$ are present meaning that radiation is circularly polarized. The synchrotron radiation emitted in the electron orbit plane ($\psi = 0$) is considered to be fully linearly polarized. This is illustrated in Fig. 2.3, where both theoretically calculated and experimentally obtained intensities of the $\mathbf{E}_\pi$ and $\mathbf{E}_\sigma$ components, which can be easily described as $I = |\mathbf{E}|^2$, are presented as a function of the opening angle ψ.

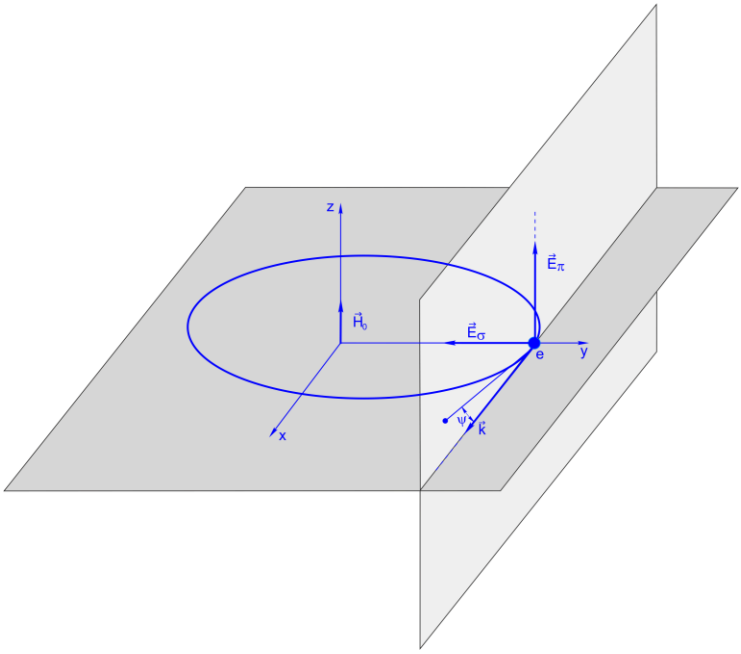

Fig. 2.2: $\mathbf{E}_\sigma$ and $\mathbf{E}_\pi$ components of the electrical vector of the linear polarized synchrotron radiation.

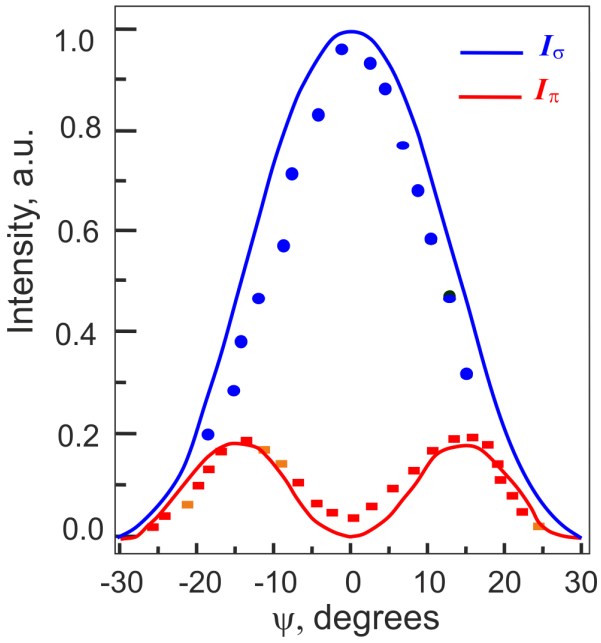

Fig. 2.3: The intensities of electrical vector components I_π and I_σ versus opening angle ψ theoretical (lines) and experimental (points) [51].

In contrast to the theoretical calculations, experiments show that the I_π component does not turn to zero for the angle $\psi = 0$. This is explained by the fact that the electron trajectory is not absolutely perfect and the electron will vibrate with respect to its orbit. The linear polarization of the synchrotron radiation is characterized by the polarization factor

$$P = \frac{I_\sigma - I_\pi}{I_\sigma + I_\pi}$$

where I_σ is the intensity of the component in the plane of the electron orbit and I_π is the intensity of the component perpendicular to the orbit. The real experimental value on the contemporary beamlines approaches 99%. The polarization factor is an important parameter, which is used in spectroscopy for the determination of molecular orientation. The polarization factor for the HE-SGM beamline was experimentally determined in the framework of this thesis and will be discussed in Section 3.1.

2.1.4. BESSY II

All experiments presented in this thesis were conducted using the UHV endstation attached to the HE-SGM beamline of the synchrotron facility BESSY II in Berlin. BESSY II is a third generation synchrotron, where the electrons are first accelerated to 1.7 GeV and then are injected into the storage ring. The synchrotron facility BESSY II, presented in Fig. 2.4, has a circumference of 240 m, provides 46 beamlines, and offers a broad range of experimental opportunities due to the availability of different radiation sources like undulators, wigglers and bending magnets with excellent energy resolution.

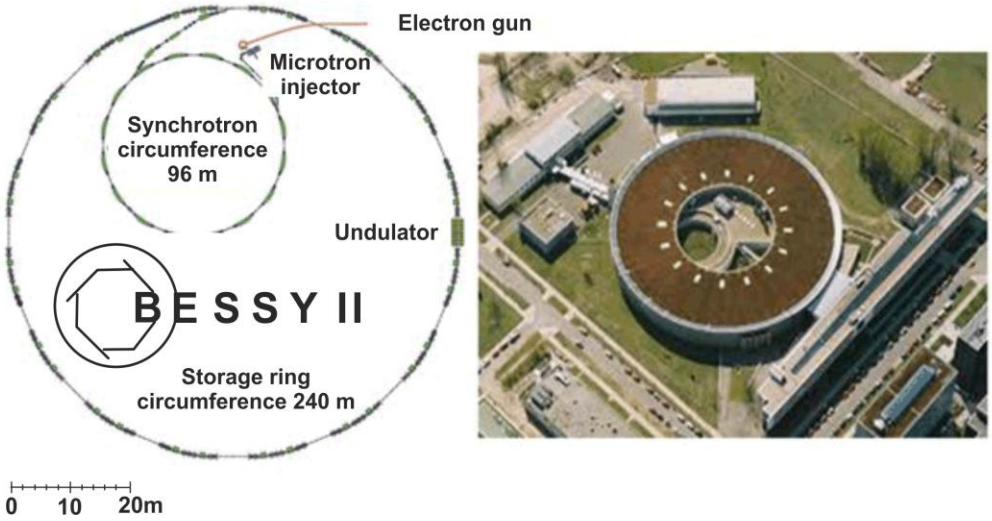

Fig. 2.4: Synchrotron facility BESSY II in Berlin: schematic view (left) and real view from the top (right). Copied with modifications from BESSY II webpage [52].

2.2 The X-ray photoelectron spectroscopy (XPS)

2.2.1 Principle of XPS

The X-ray photoelectron spectroscopy (XPS), also known as electron spectroscopy for chemical analysis (ESCA) is a method routinely used in surface science [53]. The XPS technique is suitable for identifying chemical elements and their chemical states. To

obtain XPS data, a sample is irradiated with X-rays of a constant wavelength. Photons penetrate into the material and excite electrons from the core levels to vacuum states. These electrons appear as a result of a direct photoemission process, or the radiationless de-excitation of an ionized atom known as Auger emission process (see Fig. 2.5).

The kinetic energy of emitted photoelectrons can be calculated using the Einstein equation:

$$E_{kin} = h\nu - E_{bind} - F - A$$

where $h\nu$ is a photon energy, E_{kin} is the kinetic energy of the electron, E_{bind} is the binding energy of the electron, F is the work function of the analyzer and A is a work function of the sample under study. For the Auger process the kinetic energy of the emitted electron don't depend on the photon excitation energy. The kinetic energy of a KLL Auger electron (Fig. 2.5 right) is approximately equal to the difference between the energy of the core hole and the energy levels of the two outer electrons; this can be described by the following equation:

$$E_{KLL} = E_K - E_{L3} - E_{L2} - F - A$$

where E_K is the energy of core hole, E_{L3} and E_{L2} are the energies of outer level, F is the work function of the analyzer, A is a work function of the sample under study.

The simplified scheme of the XPS experiment conducted at the HE-SGM beamline is presented in Fig. 2.6. The synchrotron radiation source, electron energy analyzer and sample under study are located in the ultra-high vacuum chamber. If the standard experimental geometry is used the synchrotron beam falls on the sample at an angle of 45^0 while the electron take-off angle is 90^0.

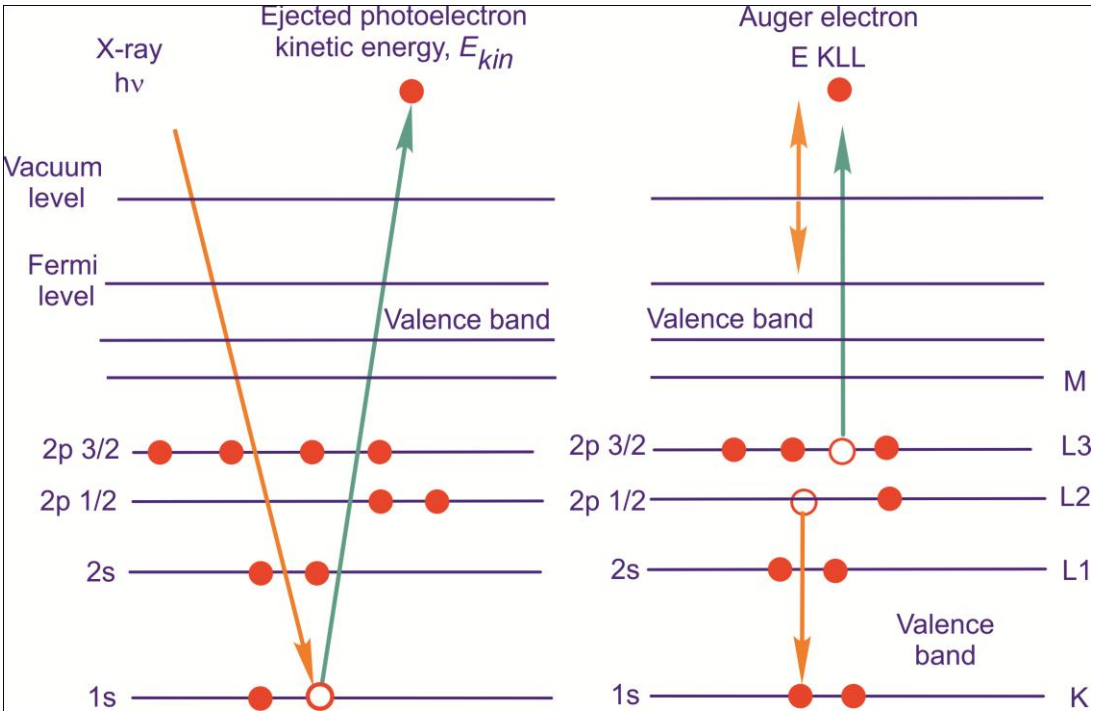

Fig. 2.5: Principle of XPS: photoelectron emission (left) and Auger electron emission (right).

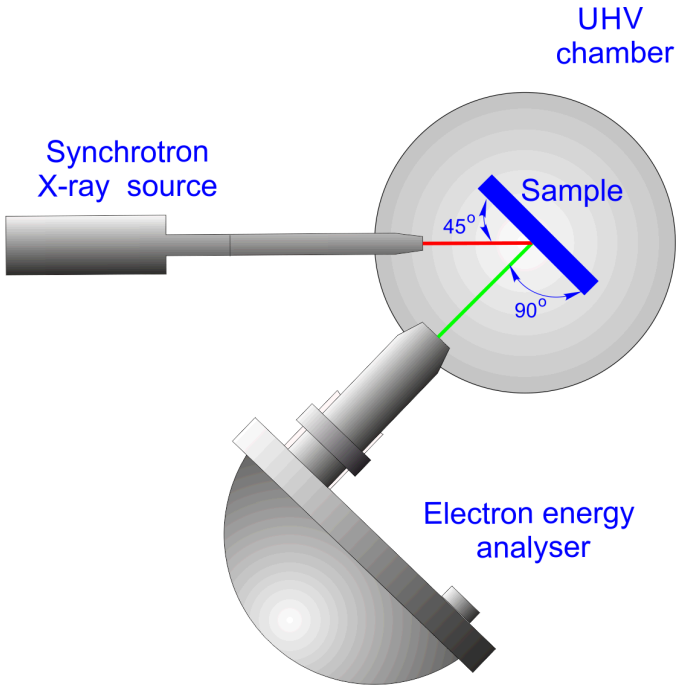

Fig. 2.6: Standard geometry of the XPS experiment at the HE-SGM beamline.

2.2.2 Advantages of the synchrotron based XPS

The synchrotron radiation has certain properties, which make it more effective and convenient for collecting XPS data compared to radiation from a conventional laboratory source. The high brilliance of the synchrotron radiation as well as the possibility to vary the photon energy makes the XPS measurements conducted at the synchrotron more advantageous. High intensity of the excitation photon radiation may allow decreasing the conventional laboratory source can usually provide X-rays of fixed energy with 1486.6 eV or 1253.4 eV depending on the anode type (Al Kα or Mg Kα respectively). The excitation energy of the synchrotron can be varied in a broad range and tuned to the specific core level threshold. Surface sensitivity refers to another advantage of the tunability. The use of excitation energies of 30-50 eV above the ionization threshold will result in a small mean free pass of the ejected electrons and therefore the surface sensitivity will be increased. For instance, if a thin organic film on some substrate is analyzed it will be possible to probe a layer as thin as 5 Å. Consequently, the unnecessary signal from the substrate is suppressed and only the topmost layer is probed. The interpretation of the XPS data is sometimes complicated by the overlap of Auger and XPS lines, which makes the proper assignments of the peaks difficult. Since the kinetic energy of the Auger electron doesn't depend on the photon energy (see equation in 2.2.1) the position of the Auger lines in the spectrum will shift in response to the change of the excitation energy if a kinetic energy scale is used. This will help to avoid the misinterpretation of the XPS data caused by overlapping of the Auger and XPS lines [54].

2.3 Near edge X-ray absorption fine structure spectroscopy (NEXAFS)

2.3.1 Principle of NEXAFS

Near edge X-ray absorption fine structure spectroscopy (NEXAFS) is a technique which deals with a detailed analysis of the spectra obtained in X-ray absorption spectroscopy experiments in the region close to an ionization potential. NEXAFS was originally developed and used for the study of molecules adsorbed on surfaces. In NEXAFS experiments the atoms are ionized by the tunable radiation, which promotes the core electrons to empty states below the ionization threshold, or to the continuum states above the ionization threshold.

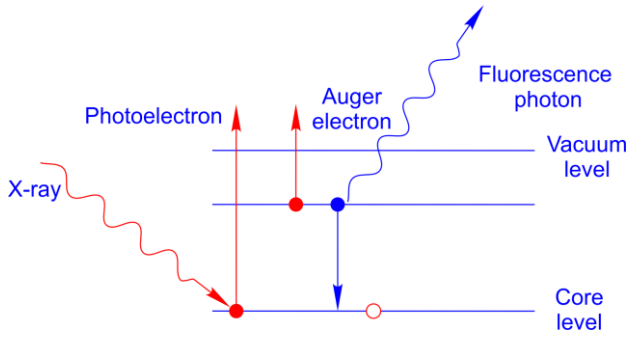

Fig. 2.7: Scheme of the X-ray absorption process.

The scheme of the X-ray absorption process is presented in Fig. 2.7. As a consequence of the core shell excitation, the photoelectrons are emitted. These photoelectrons are the direct measure of the number of created core holes and are considered to be the primary channel to monitor the absorption cross section. However the detection of the photoelectrons is considered to be insufficient to get information about the fine structure, since all the structure below ionization potential will be lost. For this reason the secondary excitation channel, which consists of the Auger electrons or fluorescent photons appearing as a result of the core hole annihilation is being monitored. NEXAFS deals mostly with the absorption edges of low Z elements such as carbon

(285 eV), nitrogen (400 eV) and oxygen (530 eV), the L-shells excitations of the elements with higher Z can also be studied. Auger decay is faster and, therefore, dominant for the K-shell excitations of low Z atoms and for L-shells excitations of all atoms with Z < 90 [56]. Therefore, to record NEXAFS spectra of the organic molecules the Auger electrons are collected. The property which makes the NEXAFS technique such a powerful tool for the analysis of molecular electronic structure is the possibility to distinguish between molecular orbital types and define molecular orbital orientation and therefore a chance to define the orientation of the organic molecule adsorbed on the surface and interfaces.

2.3.2 Molecular orbitals

Before going into details concerning the characterization of different molecules with the NEXAFS technique I will provide a brief discussion on molecular orbitals (MO) and molecular orbital theory. MO is a wave function describing the electron distribution around nuclei. According to molecular orbital theory, the bonding between atoms is facilitated by the formation of molecular orbitals via combination of their atomic orbitals. The electrons are not assigned to one particular atomic bond, but considered to be distributed across the whole molecule. Each MO can be filled by maximum two valence electrons with opposite spins. Like in the case of atomic orbitals the MO with the lowest energy are filled first. Molecular orbitals are subdivided into different types according to their symmetry. σ orbitals are molecular orbitals that are symmetrical about the axis of the bond. The diagram of the simplest MO diagram for the hydrogen atom is presented in Fig. 2.8. The 1s orbitals of two hydrogen atoms form correspondingly one bonding σ orbital and one antibonding σ* orbital.

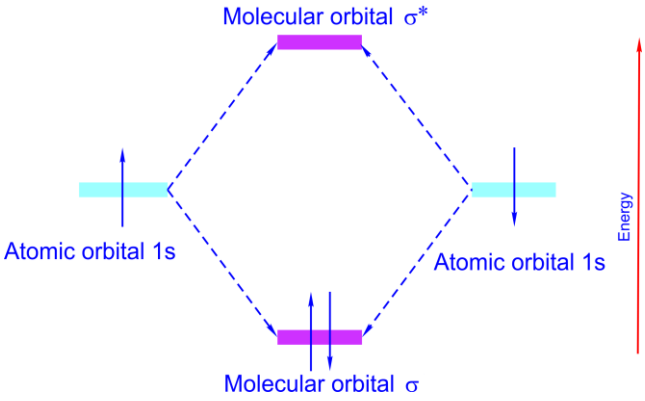

Fig.2.8: The MO diagram of the hydrogen molecule. Two 1s atomic orbitals form two σ molecular orbitals.

In contrast to σ orbitals, π are asymmetrical with respect to rotation about the axis which joins two nuclei.

Fig. 2.9 presents the molecular diagram for benzene. Benzene has 6 planar sp^2 carbons, and therefore each carbon has an unhybridized 2p orbital. The lowest energy MO, π_1, is entirely bonding, with zero nodes. All the lobes above the plane of carbon atoms interfere constructively, as do the lobes below the plane of carbon atoms.

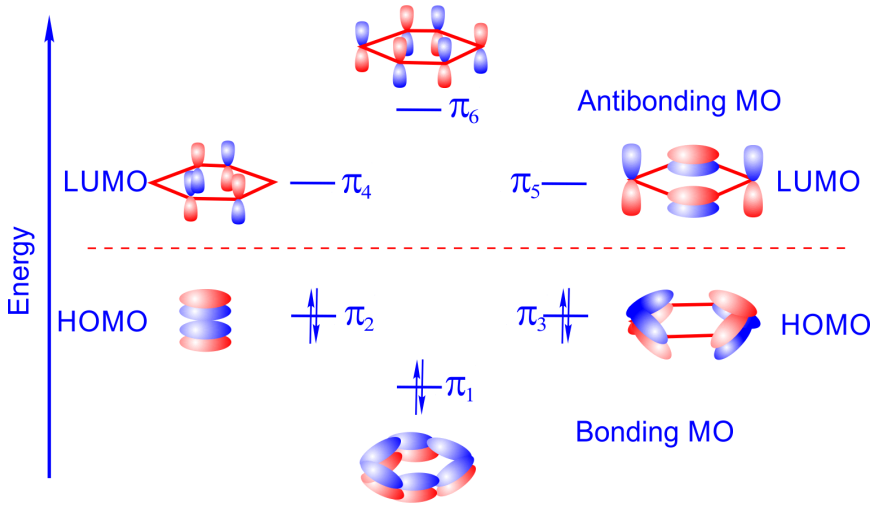

Fig. 2.9: MO diagram for benzene.

The six p orbitals overlap to form a continuously bonding ring of electron density. It is of very low energy because of the 6 bonding interactions, and the electrons are equally delocalized over the six carbons. The MOs of the next higher energy are π_2 and π_3. They

both comprise of 4 bonding interactions and two antibonding interactions (and one nodal plane). They both have the same energy (overall two net bonding interactions) and are overall bonding, but not as bonding (i.e. of low energy) as π_1*. The next two higher energy MO's are π_4* and π_5*. These are also degenerate orbitals with overall two net antibonding interaction (π_4* has two non-bonding interactions, and two anti-bonding interactions; π_5* has two bonding and 4 anti-bonding interactions). They contain two nodal planes. The MO's of π_4* and π_5* are as antibonding as π_2 and π_3 are bonding. The highest energy MO is π_6* and contains 6 anti-bonding interactions (and three nodal planes).

2.3.3. NEXAFS sensitivity to molecular orbitals

One of the greatest assets of NEXAFS is the possibility to retrieve the information concerning molecular orbital types present in the molecule. Fig. 2.10 presents the X-ray absorption scheme for a molecular subunit consisting of two atoms and its corresponding typical NEXAFS K-edge spectrum. The scheme is built using a very simple approximation considering the excitation process for a diatomic subunit. The Auger electron emerging as a result of the electron transitions to the MO orbitals π* or σ* and subsequent annihilation of the resulted core hole can be detected. A typical NEXAFS spectrum is shown in Fig. 2.10. The resonances corresponding to the 1s→π* transitions lie in the lower energy region and have a sharp shape. The resonances corresponding to 1s→σ* transitions have a broader shape and will usually appear at higher energies above the absorption edge. Rydberg resonances are usually seen between the π* resonances and the absorption edge carrying no information concerning molecular orbitals [56]. Of course, the 1s→π* transitions cannot be observed for molecules with a single bond, but will be visible for the molecules with a double and triple bonding. The width of the

resonances depends on the lifetime of the excited states and increases as the location of the final orbital approaches continuum.

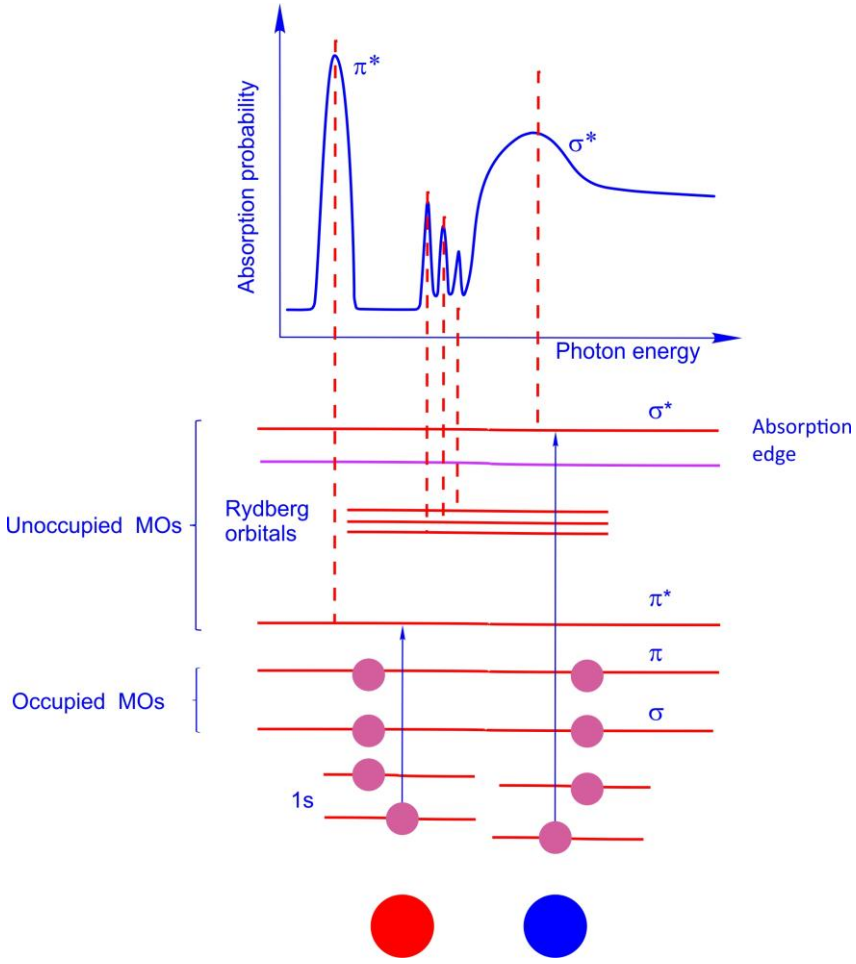

Fig. 2.10: Diatomic subunit with corresponding 1s→π* and 1s→σ* transitions and typical NEXAFS spectrum profile. Modified from [55].

2.3.4. Angular dependence of resonance intensities

The single electron excitation can be described using Fermi's golden rule expressed by the equation

$$\sigma \propto \left|\langle \Psi_f \left| \mathbf{e}\cdot\mathbf{p} \right| \Psi_i \rangle\right|^2 \rho_f(E)$$

where σ is an absorption cross section, Ψ_i and Ψ_f are the wave functions of initial and final states, respectively, **e** is a unit electric field vector and **p** is a dipole transition

operator, with $\rho_f(E)$ being the density of final states. The σ* orbitals have a maximum of orbital amplitude along the bond axis, while the π* orbitals have maximum amplitude normal to the bond direction. For a case of linearly polarized light the expression for the 1s initial transition intensity looks as follows:

$$I \propto |\mathbf{e}\langle \Psi_f | \mathbf{p} | \Psi_{1s} \rangle|^2 \propto |\mathbf{eO}|^2 \propto \cos^2 \delta$$

In this expression **e** is the electrical field vector and **O** is the direction of the final state orbital or transition dipole moment (TDM), while δ is an angle between these two vectors [56].

This direct dependence of the intensity on the angle between electrical vector and TDM is the foundation of another great strength of NEXAFS spectroscopy. The intensity of the resonances corresponding to particular molecular orbitals will depend strongly on the orientation with respect to the electrical field vector. Since there is a direct dependence between the spatial orientation of the orbital and the molecular geometry, it is possible to determine the orientation and structure of the molecule as well as that of single molecular fragments.

For a molecule adsorbed on a surface, the transition intensities depend on the orientation of the electrical field vector components $E_{\parallel}$ and $E_{\perp}$ with respect to the molecule. Fig. 2.11 represents the vector description of π and σ orbitals. The MO orientation, i.e. vector is defined by the polar angle α and azimuthal angle ϕ. The X-rays are incident in the orbit plane (x, z), which contains the major electrical field vector component. The X-ray incidence angle θ can be changed by rotating the crystal about the y axis. The intensity for $E_{\parallel}$ and $E_{\perp}$ components can be written as

$$I = A\left[PI_{\parallel} + (1-P) I_{\perp} \right]$$

$$I_{\parallel} = \cos^2\theta\cos^2\alpha + \sin^2\theta\sin^2\alpha\cos^2\phi + 2\sin\alpha\cos\alpha\sin\theta\cos\theta\cos\phi$$

and

$$I_{\perp} = \sin^2\alpha\sin^2\phi.$$

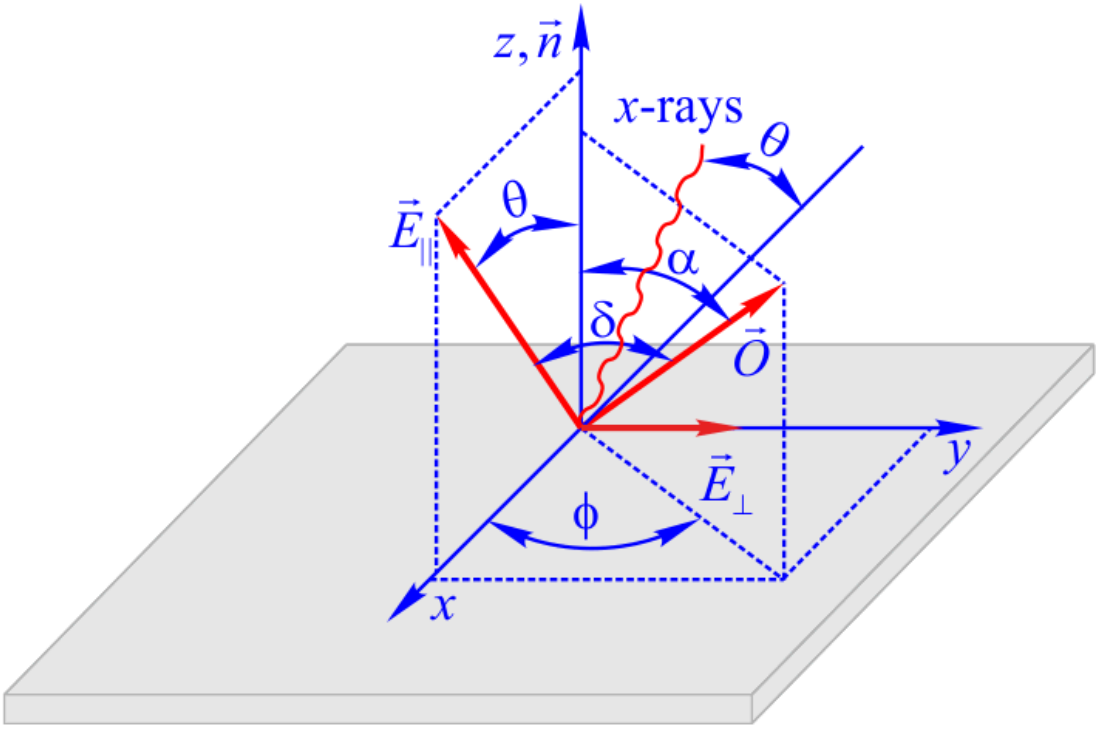

Fig. 2. 11: Coordination system of the NEXAFS experiment. The direction of π* or σ* molecular orbitals is defined by the vector **O**, which is defined by polar angle α and azimuthal angle ϕ.

The azimuthal dependence on the angle ϕ can be reduced or eliminated for the higher substrate symmetry. For twofold or higher order symmetry the expression can be simplified and takes the following form:

$$I_{\parallel} = \cos^2\theta\cos^2\alpha + \sin^2\theta\sin^2\alpha\cos^2\phi$$

and

$$I_{\perp} = \frac{1}{2}\sin^2\alpha.$$

For the threefold and higher symmetry the dependence on the azimuthal angle can be eliminated.

$$I_{\parallel} = \cos^2\theta\cos^2\alpha + \frac{1}{2}\sin^2\theta\sin^2\alpha$$

and

$$I_{\perp} = \frac{1}{2}\sin^2\alpha.$$

In order to determine the orientation of the molecule the experimentally obtained values of π* and σ* resonance intensity are plotted as a function of the incidence angle. The obtained dependence is compared to the curve calculated by equations provided above.

The common way to illustrate the angular dependence of NEXAFS spectra resonance intensity is to display the NEXAFS data measured for highly ordered pyrolytic graphite (HOPG) at different incidence angles. This selection of this system is explained by the highest degree of three-dimensional ordering of the graphite. The network of carbon atoms are connected in a honeycomb structure forming planes which are connected by π bonds forming a lamellar structure. Fig. 2.12 (a) shows the standard measurement geometry of the NEXAFS experiment at HE-SMG beamline. NEXAFS data for HOPG measured at different incidence angles θ is presented in Fig. 2.12 (b). The intensity of the resonance corresponding to the π* transition at 285.7 eV shows a clear dependence on the photon incidence angle. The maximal intensity is observed at grazing incidence and minimum intensity at normal incidence. At the same time, the σ* resonance

shows the opposite behavior: the highest intensity is observed at normal incidence and lowest intensity at grazing incidence. This is an excellent prove of the theoretical assumptions listed above.

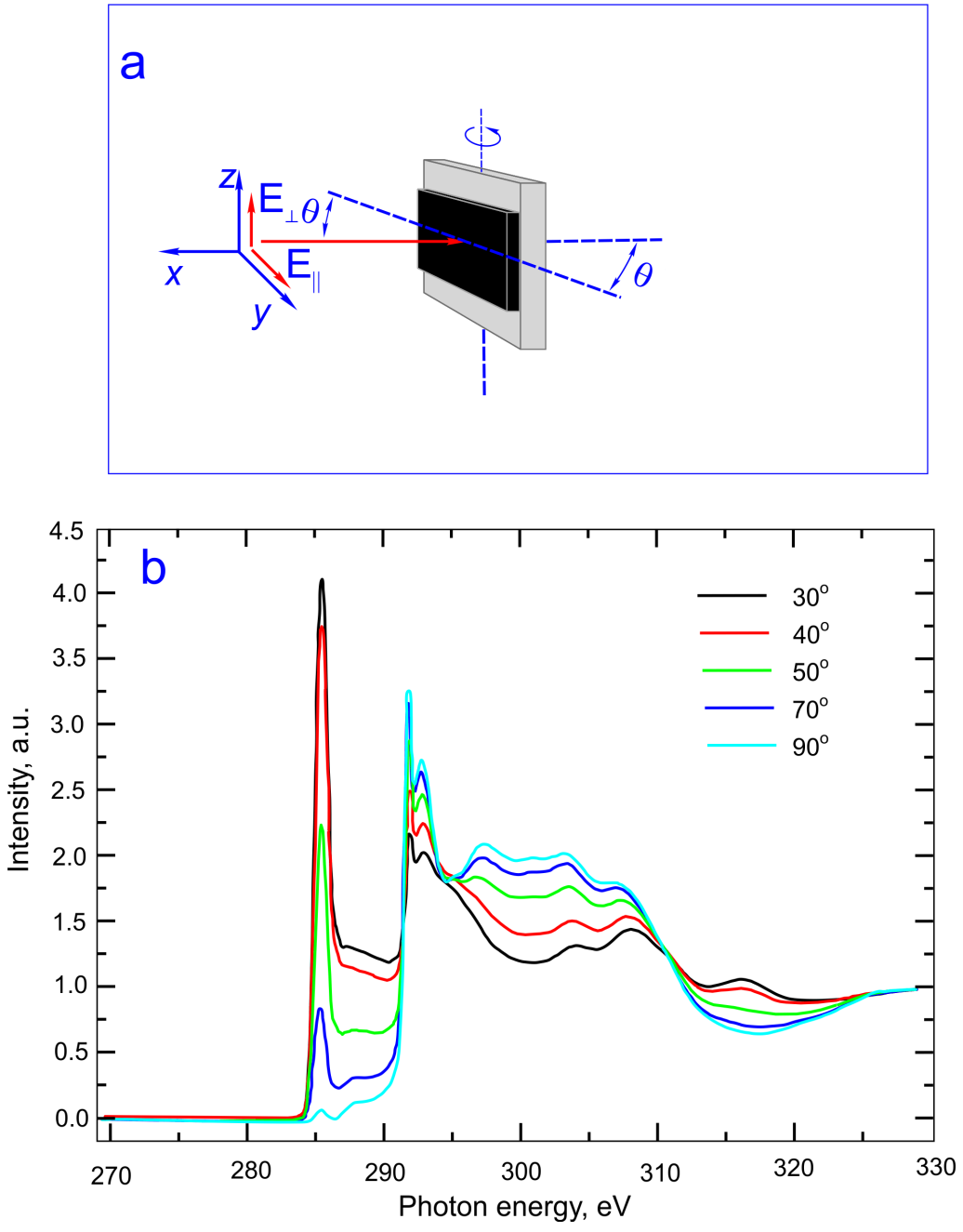

Fig. 2.12: NEXAFS spectra obtained for HOPG measured using standard geometry for various incidence angles θ varying from 30° to 90°.

2.3.5 Acquisition of the NEXAFS spectra

The photon absorption process occurring on the sample consisting of adsorbate and substrate which leads to emission of electrons is presented in Fig. 2.13, where the photons are shown to penetrate the adsorbate and the substrate. The incident X-ray photons penetrate quite deep into the sample (about 1 μm for the soft X-rays). The absorbed X-rays generate photoelectrons and Auger electrons. On the way to the surface these electrons will be scattered inelastically due to electron-electron interaction. The inelastic scattering of the electrons forms an electron cascade. When the cascade reaches the surface, only the electron with sufficient energy higher than the work function of the sample will escape into vacuum.

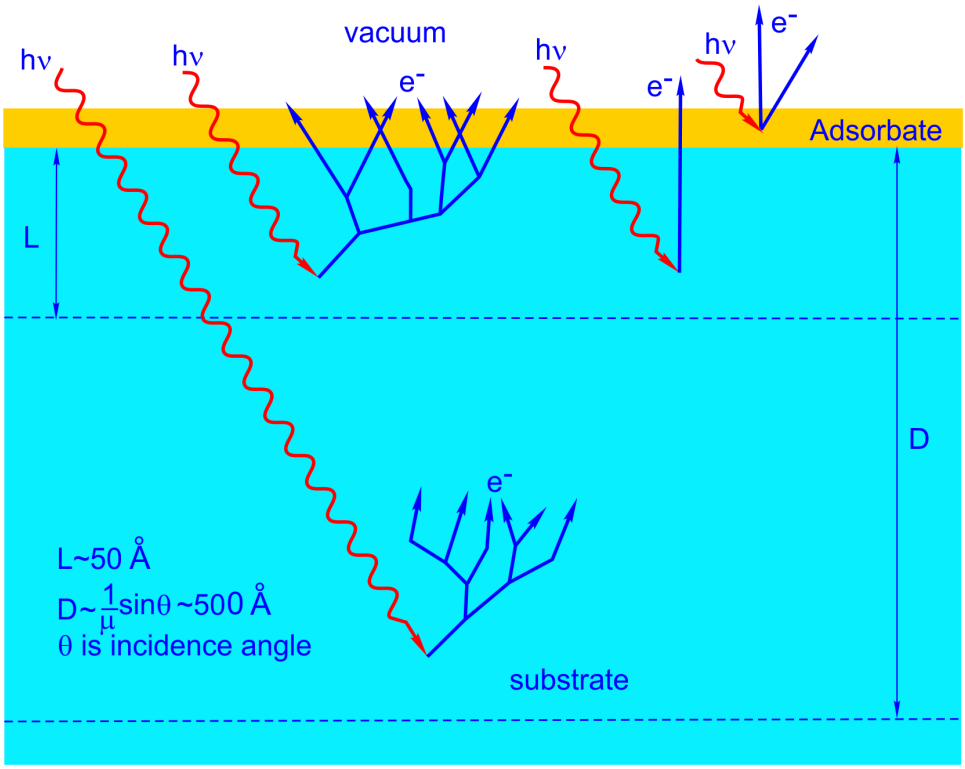

Fig. 2.13: Photon penetration depth D (depends on absorption coefficient μ and radiation incidence angle θ) and inelastic mean free pass L of Auger electrons. Adopted from [56].

As it was highlighted above, in NEXAFS experiments performed on organic

adsorbates, the electrons emerging from the surface are detected. To get the optimal signal from the sample it is important to optimize the signal-to-noise ratio by removing the unwanted background signal. In order to illustrate the photoemission events after absorption of X-rays in solids, the schematic photoemission energy level diagram for the solid sample which consists of substrate and adsorbate is presented in Fig. 2.14. The atoms from the adsorbate and substrate have the core levels A and B respectively, while the valence level of the adsorbate atoms overlap the substrate valence band. The Fermi level E_F is separated from the vacuum level E_V by the work function ϕ.

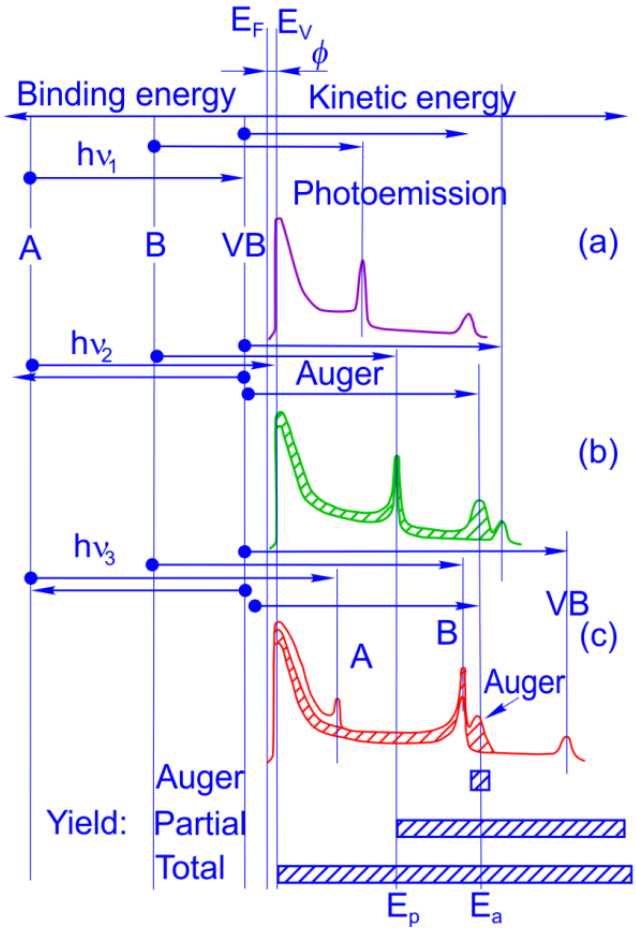

Fig. 2.14: Energy level diagram and schematic photoemission spectra for different photon energies. Solid sample containing atoms with two core levels adsorbate A and substrate B [56]: (a) $h\nu_1$ below excitation threshold of core level of shell A; (b) $h\nu_2$ just above the absorption threshold of shell A. (c) $h\nu_3$ above the absorption threshold of shell A.

The photon energy $h\upsilon_1$ lies below the excitation threshold of the atom A but high enough to ionize atom B. The energy is increased to $h\nu_2$ which is still below the photoemission threshold of atom A. This means that the photoelectron excited from the adsorbate shell A doesn't have sufficient energy to overcome the work function and leave the sample, however there is enough energy to promote the electron to the valence band. As a consequence the Auger electron and the corresponding Auger peak appear as a result of the decay of an adsorbate valence electron into the core hole in shell A. Since the photoelectron kinetic energy depends on the photon excitation energy the photoemission peak from atom B will move on the kinetic energy scale. If the photon energy is further increased to $h\nu_3$ level, both photoemission peaks corresponding to level A and levels B as well as the Auger peak are observed. The energy of the Auger peak remains fixed. The intensity of the Auger peak changes with changing of the photon energy and follows the X-ray absorption cross section of peak A. Using an electron analyzer it is possible to set a proper energy window corresponding to the fixed energy E_a. of the Auger peak. This measurement mode is known as the Auger electron yield (AEY). The AEY mode to detect NEXAFS signal requires an electron energy analyzer and is considered to be the most surface sensitive mode.

A fraction of the Auger electrons from the adsorbate loses energy and emerges from the sample with energy less than E_a. Because the primary Auger kinetic energy is independent of the photon energy $h\nu$, the energy distribution of the inelastic electrons is shown as hatched area in Fig. 2.14. For this reason the inelastic Auger intensity will follow the elastic one. This fact is employed in partial electron yield (PEY), where only the electrons with sufficient kinetic energy are detected while the electrons with kinetic energy less than E_p are being cut. The PEY mode can be realized by using the electron analyzer or by applying a retarding voltage to the electron detector. The total electron

yield (TEY) mode, in which the electrons of all energies are collected integrally, can also be used. In the TEY mode dominating contribution is defined by low energy electrons with kinetic energy less than 20 eV. These electrons are inelastically scattered Auger electrons from the adsorbate. This fraction of electrons is known as an inelastic tail. The TEY mode will give a high total count rate, however the signal to noise ratio will be poor.

2.4. Low energy electron diffraction (LEED)

The Low-energy electron diffraction (LEED) is a technique routinely used in surface science for the determination of the surface structure by probing the surface with a collimated beam of low energy electrons (20–200 eV) and observation of diffracted electrons as spots on a fluorescent screen [59]. LEED allows both qualitative and quantitative analysis of the surface. The scheme of the typical LEED experiment is presented in Fig. 2.15. A beam of low energy electrons with known energy falls normally on a single crystal surface. The diffraction pattern of back scattered electrons is observed on the screen. The wavelength range of electrons in LEED experiments is selected to be comparable with atomic spacing, which is the necessary condition for diffraction effects associated with atomic structure to be observed.

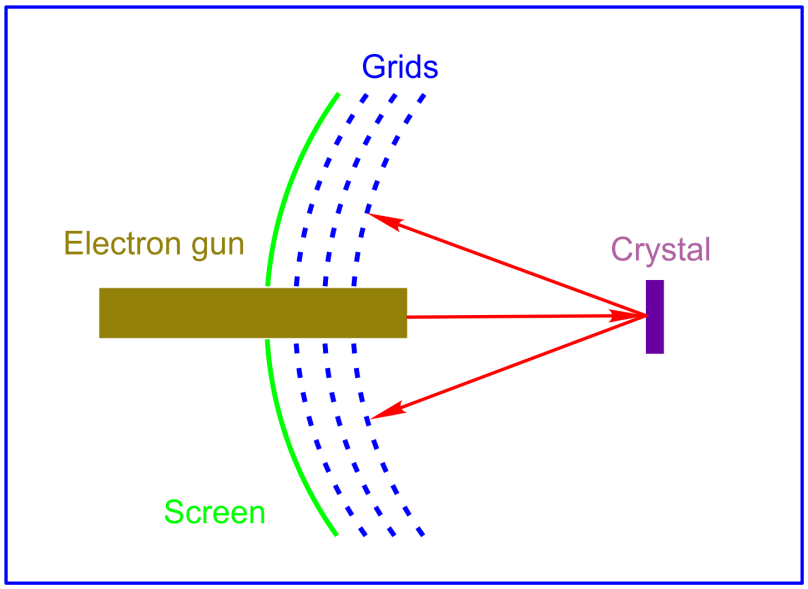

Fig. 2.15: Typical LEED experiment.

The simplest model of the LEED experiment for a surface study is a 1-dimensional chain of the topmost layer of atoms with an interatomic distance is presented in Fig.2.16.

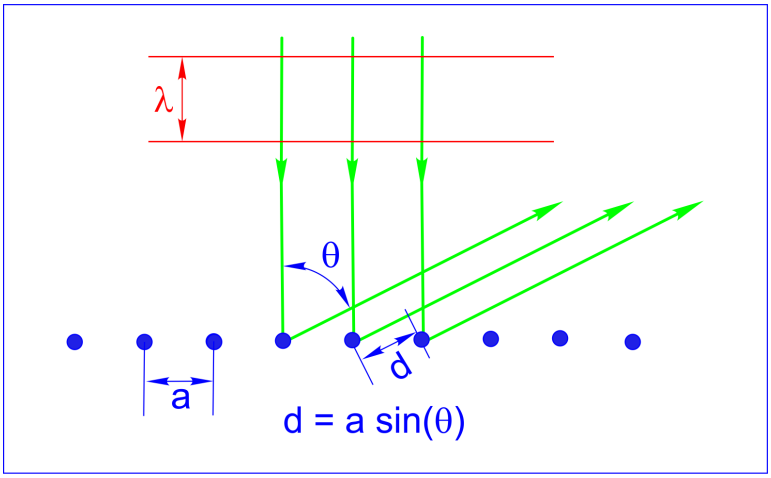

Fig. 2.16: The simplest approximation model for the LEED experiment**.**

The path difference *d* must be equal to an integer number of wavelengths for constructive interference to occur when the scattered beams interfere at the detector i.e.

$$d = a\sin\theta = n\lambda,$$

where λ is a wavelength of the electron.

3. EXPERIMENTAL EQUIPMENT

In the previous chapter the fundamentals of the experimental synchrotron techniques used in this thesis, namely NEXAFS and XPS, were briefly presented. The following chapter describes experimental UHV endstation attached to the HE-SGM beamline of the synchrotron facility BESSY II. The chapter also includes a more detailed description of the NEXAFS experiment as well as the proper procedure for acquiring and processing NEXAFS spectra.

3.1 HE-SGM Beamline

The schematic view of HE-SGM beamline, where the NEXAFS and XPS data contained in this thesis were acquired, is presented in Fig.3.1. The synchrotron light emerges from the dipole magnet and covering a broad range of wavelengths enters the beamline. After being focused by the toroidal mirror, the light radiation beam passes through the entrance slit. Then the radiation light is monochromatized by the spherical grating monochromator.

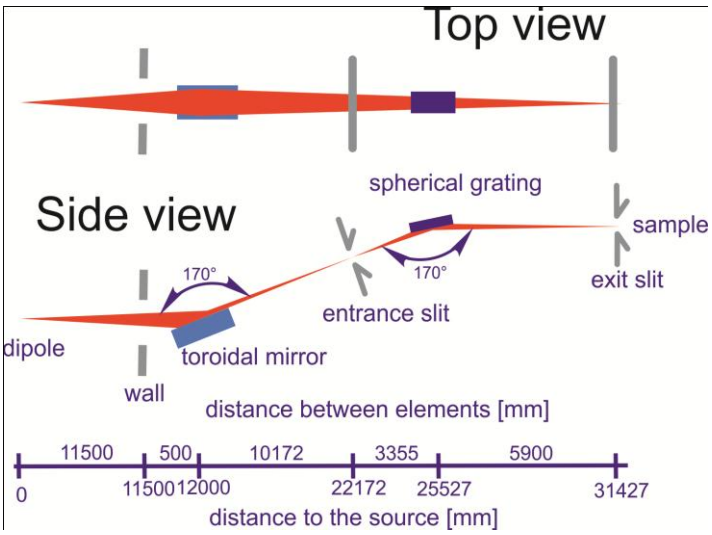

Fig. 3.1.: Schematic view of HE-SGM beamline [52].

Three available diffraction gratings allow selecting the radiation of the chosen wavelength in different spectral ranges. The flux curves for three diffraction gratings are presented in Fig. 3.2. All three flux curves are affected by a carbon contamination of the beamline components. Of course this is very undesirable for the measurements performed on the C K-edge. Fortunately, the contamination can be removed by the oxygen plasma treatment and this procedure was successfully accomplished for the HE-SGM beamline optics. Fig. 3.3 demonstrates the transmission function measured on the clean gold wafer, the curve is quite smooth and almost lineal.

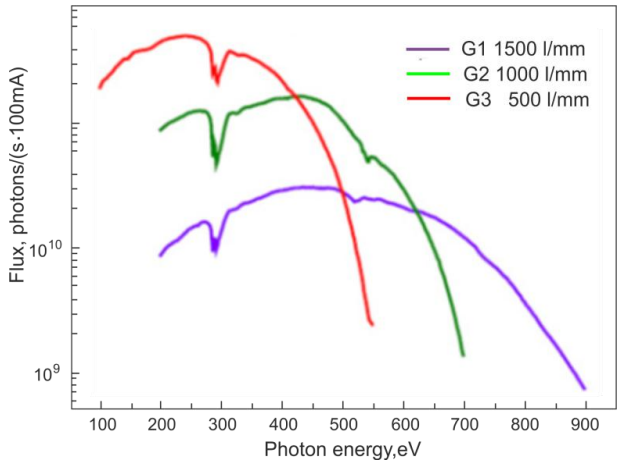

Fig. 3.2.: Flux curves for various monochromator gratings [52].

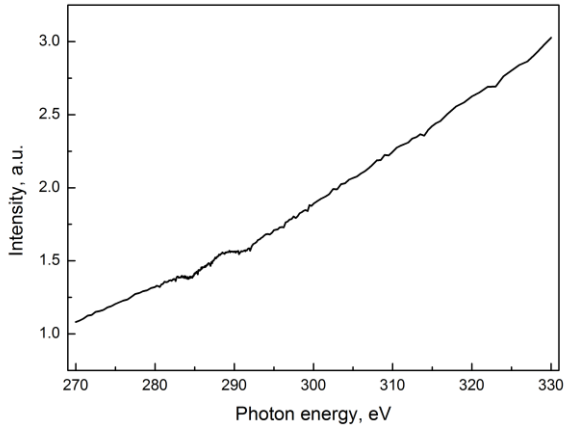

Fig. 3.3 Transmission curve measured on the gold wafer after oxygen plasma treatment of the HE-SGM beamline components.

3.1.1 Determination of the polarization factor of the HE-SGM beamline

In section 2.1.4 it was highlighted that the beamline polarization factor is an important component of the equation used to retrieve the MO average orientation from NEXAFS data. The procedure to determine the polarization factor of the HE-SGM beamline using the experimental NEXAFS spectra measured for HOPG is described below. The polarization factor P can be calculated according to the equation:

$$P = \frac{I_{\parallel} - I_{\perp}}{I_{\parallel} + I_{\perp}} \tag{3.1}$$

where $I_{\parallel} = \left|E_{\parallel}\right|^2$ is the intensity of the parallel component and $I_{\perp} = \left|E_{\perp}\right|^2$ is the intensity of the perpendicular component of the electrical field vector.

It is necessary to obtain the intensity values for each component of the electrical field vector ($E_{\perp}$ and $E_{\parallel}$) separately. In the standard geometry of the NEXAFS experiment described in Section 2.3 it is not possible, since the $E_{\perp}$ component lies always in the plane of the graphite plate and only the $E_{\parallel}$ component contributes to the spectrum (Fig. 3.4 (a)). However, the placement of the HOPG sample in a special geometry (Fig. 3.4(b)) leads to the opposite case, where only $E_{\perp}$ component contributes to the spectrum. Fig. 3.5 shows the sample holder with a sample fixed in the special geometry in the analysis chamber as it should be during an experiment. NEXAFS spectra measured in two different geometries are presented in Fig. 3.6. It was found that the intensities of π* resonances obtained for parallel and perpendicular components are 7.19 and 0.71 respectively. After calculation according to equation 3.1 we determined the polarization factor P to be 0.91.

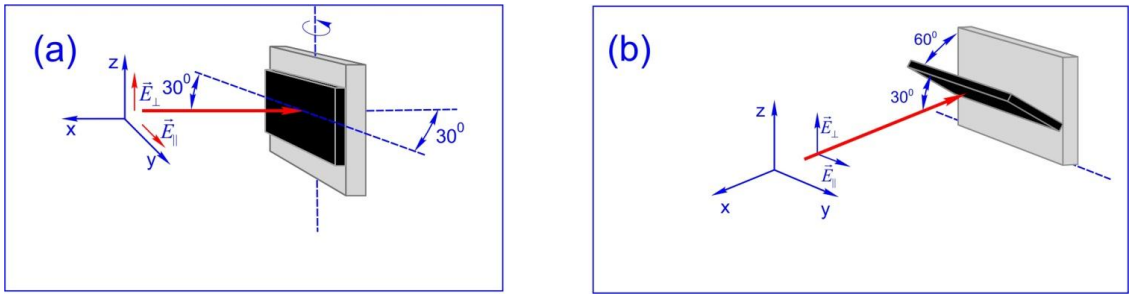

Fig. 3.4.: Two geometries used in the experiment for determination of the polarization degree on HE-SGM beamline. (a) standard geometry (only $E_{||}$ component contributes to the spectrum), (b) special geometry (only $E_\perp$ component contributes to the spectrum).

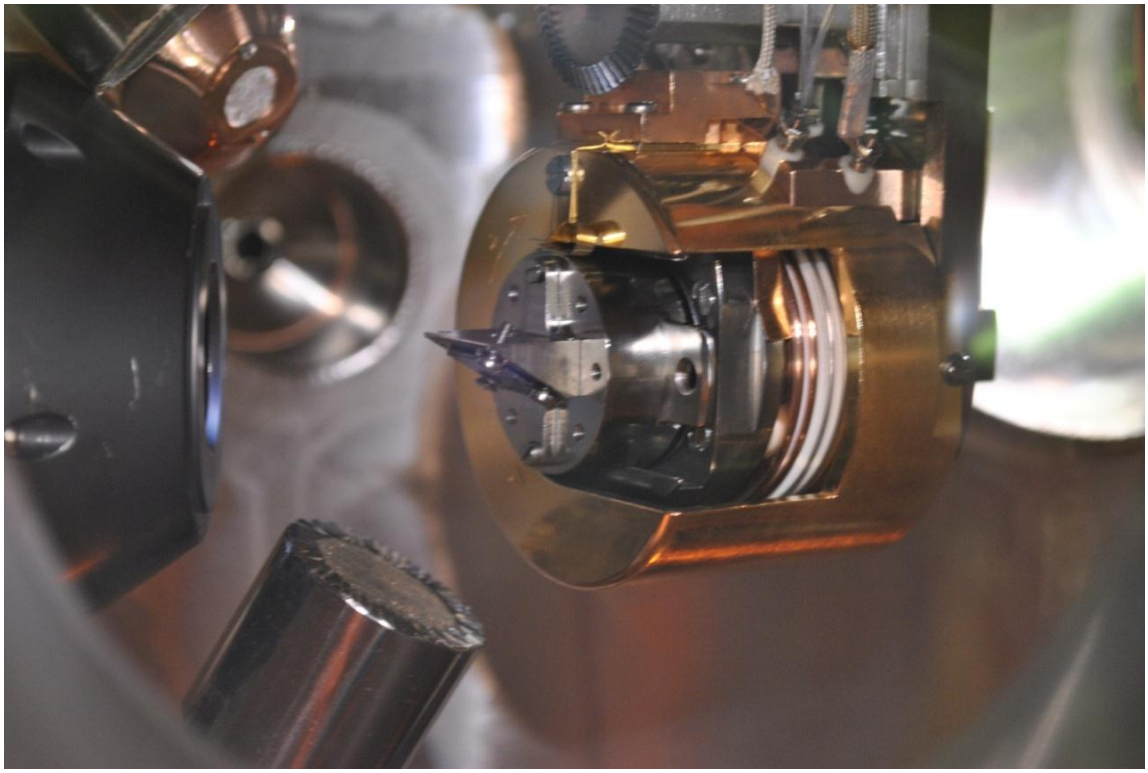

Fig. 3.5.: Sample in the analysis chamber placed in the special geometry (only $E_\perp$ component of electrical vector contributes to the spectrum).

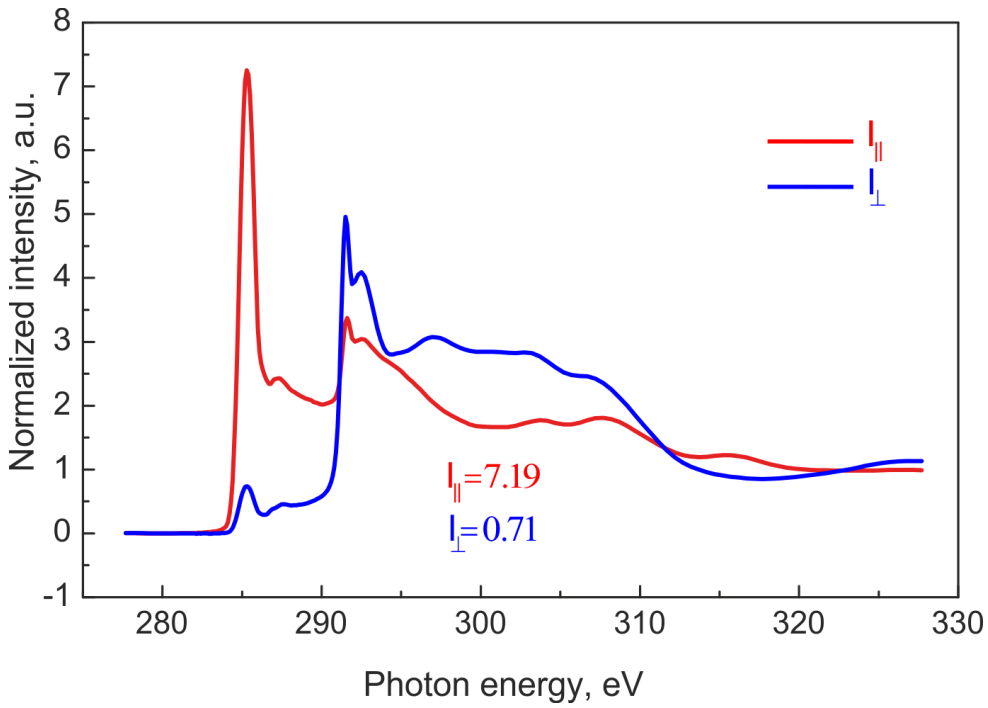

Fig. 3.6.: NEXAFS C K-edge spectra measured for HOPG in standard geometry (only $E_{\parallel}$ component contributes to the spectrum), and special geometry (only $E_{\perp}$ component contributes to the spectrum).

3.2 NEXAFS/XPS endstation at HE-SGM beamline at BESSY II

The new NEXAFS/XPS machine was developed and constructed by Prevac (Poland) and was installed and tested at the HE-SGM beamline at BESSY II. The machine works under ultrahigh vacuum conditions (pressure less than 10^{-10} mbar) and consists of the analysis chamber, the distribution chamber with the transfer system, the preparation chamber, and two load locks. The schematic view of the machine is presented in Fig. 3.7.

A quick sample transfer system can be useful for the low temperature deposition in the preparation chamber with subsequent low temperature measurement in the analysis chamber. To minimize temperature losses the sample is quickly transferred from the preparation chamber to the analysis chamber (1 minute).

The location of the preparation chamber with respect to the distribution chamber and the

analysis chamber provides the possibility to perform measurements and the preparation of samples independently. In the park station attached to the distribution chamber there is a place for six samples to be stored for an extended period of time without being exposed to the atmosphere.

The fully motorized and computer controlled manipulator makes it possible to measure XPS and NEXAFS spectra at various polar and azimuth angles. For recording NEXAFS spectra a microchannel plate (MCP) electron detector is used. For XPS measurements a Scienta R3000 electron analyzer is available, which also can be used as a NEXAFS detector. The sample can be cooled down to 40 K and heated up to 2000 K. In the preparation chamber, it is possible to clean the sample surface by ion sputtering. Up to three evaporators can be installed for molecular deposition. There is also the possibility to record LEED patterns. The general view of the endstation is presented in Fig. 3.8.

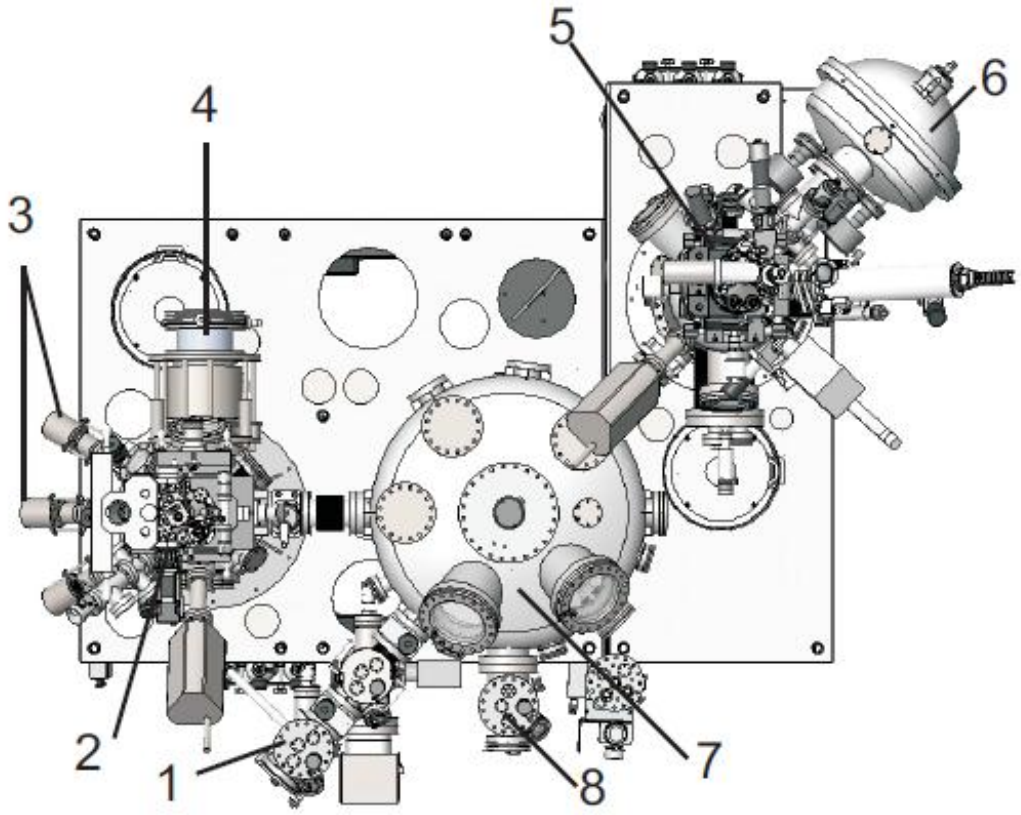

Fig. 3.7.: NEXAFS/XPS system 1-load lock chamber, 2-preparation chamber, 3-evaporators, 4-LEED system, 5-analysis chamber, 6-electron analyzer Scienta 3000, 7-distribution chamber, 8-park station from [57].

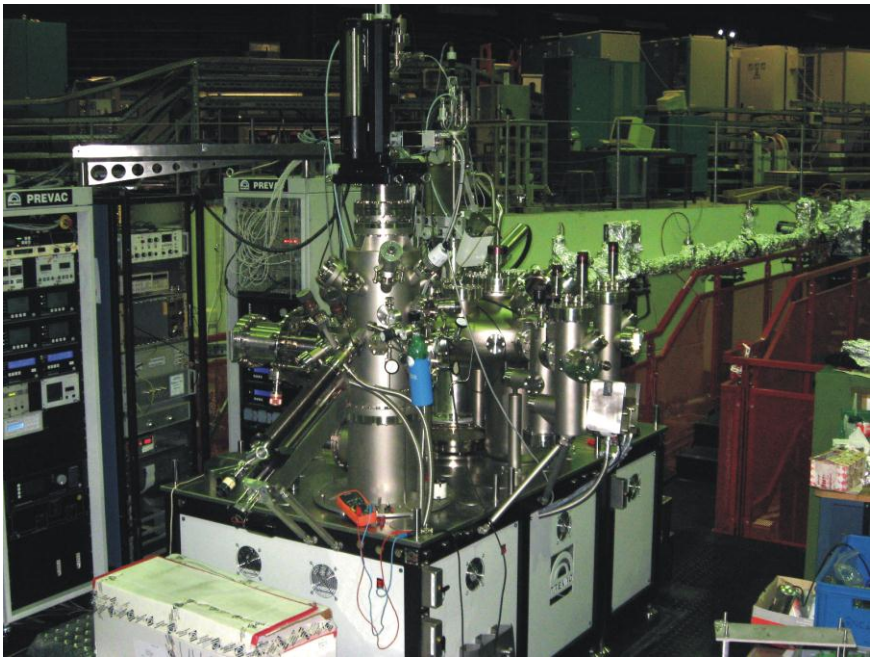

Fig. 3.8.: NEXAFS/XPS endstation attached to HE-SGM beamline.

3.3 Sample holders

Depending on the experimental requirements different sample holders can be used. In Fig. 3.9, three main types of the sample holders used in this work are presented. A standard sample holder has no heater and can be used for samples which do not require high temperature treatments. The holder with a resistance-type heater has a heating coil inside; its upper temperature limit amounts to 1000 K. For the experiments where even higher temperatures are required, the sample holder facilitating electron bombardment is used. The electrons are emitted from a tungsten filament and are accelerated toward a tantal plate on which the sample is mounted by applying a high voltage of up to 1 kV. Temperatures of up to 1300 K can be reached. Schematic views of the sample holders are presented in Fig.3.10. The electrical contacts corresponding to heating, bias, and thermoelement are also shown.

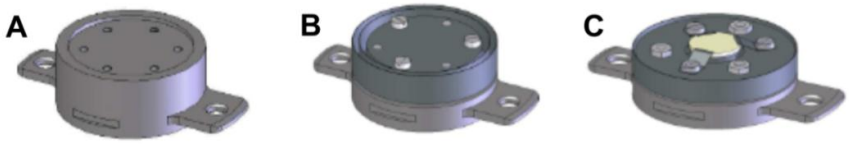

Fig. 3.9.: View of the sample holders which are used on the station: A - standard sample holder (no heater), B - sample holder with a resistive heating, C - sample holder with electron bombardment heating (copied from PREVAC manual).

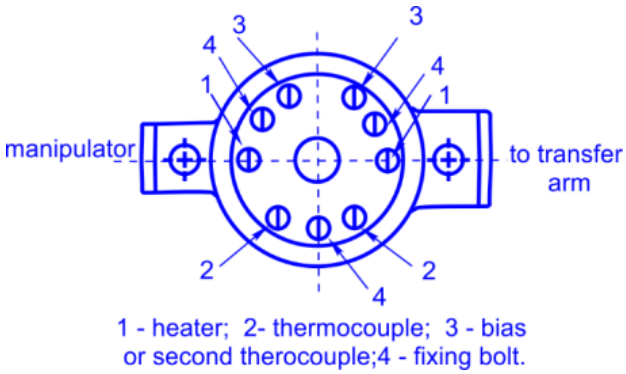

Fig. 3.10.: Schematic view of the sample holder (redrawn with modification from PREVAC manual).

3.4. Construction of the cooling system in the analysis chamber

Some of the experiments presented in this thesis require a sample temperature as low as 100 K. This temperature should not only be reached but also maintained during the whole measurement. For this reason an effective cooling system is a prerequisite for the sucessful experiment. The scheme of the cooling system is presented in Fig. 3.11. The cold finger of a cryostat is connected to a sample holder by means of the copper braid. During the experiments, the temperature is monitored at different points by two low temperature diodes denoted by A (located on the cold finger) and B (located near the sample holder and directly attached to the sapphire ball). The third point where the temperature is monitored by thermocouple is the sample holder.

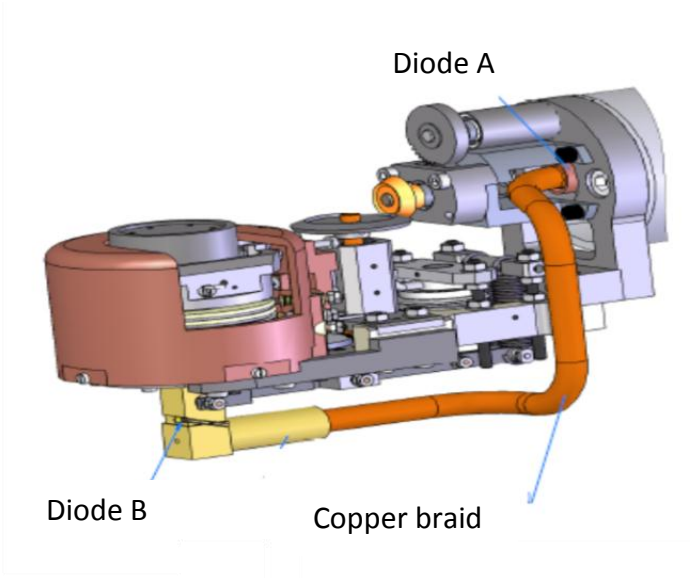

Fig. 3.11.: Schematic view of the cooling system in the analysis chamber (PREVAC manual).

Thus, it is possible to estimate the temperature at each point of the cooling system. In order to increase the cooling efficiency the copper shroud is additionally cooled with LN_2. The test of the cooling system was part of the overall test of the NEXAFS set-up. The cooling system of such a type had never been manufactured by PREVAC before.

Accordingly, we have carried out a careful test of the new equipment. The result of the cooling test is presented in Fig. 3.12. It was possible to read a temperature as low as 36 K on the sample within 40 minutes with the same temperature on the diode near the sample and 24 K at the diode near the cryostat. The result of the test demonstrated that the cooling system worked sufficiently well.

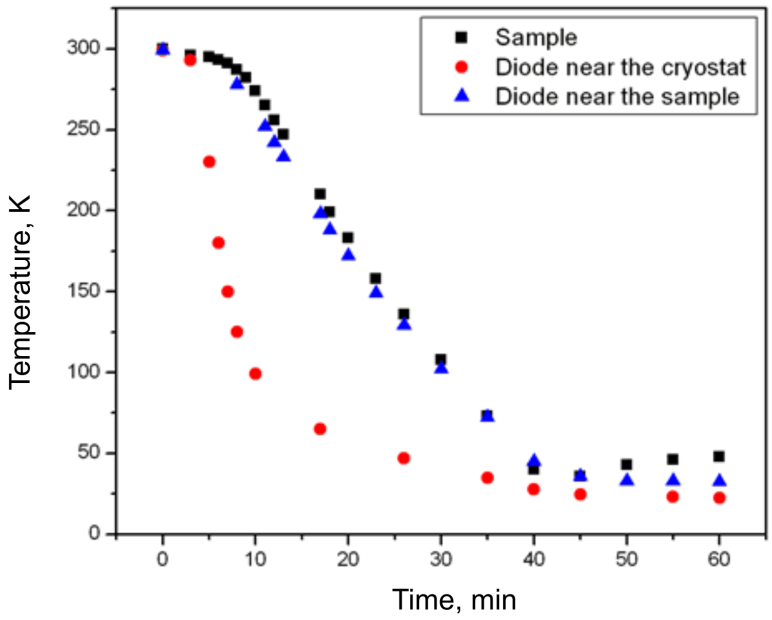

Fig. 3.12.: Results of the cooling test with liquid helium supported with nitrogen cooling.

3.5. NEXAFS detector

The MCP detector for the NEXAFS experiments used in this work is presented in Fig. 3.13. Electrons coming from the samples first pass through the metal grid, where the retarding voltage is applied to facilitate the partial electron yield mode described in the previous chapter. The electrons are accelerated and forced to move through a pair of microchannel plates (MCP), which are placed in a chevron configuration, by applying a

voltage of 2.1 kV to the anode and 0.2 kV to the cathode. The MCP is a component used for detection of particles like electrons or ions. The MCP is made from resistive material and has a thickness of about 0.5 mm with a regular array of tiny microchannels leading from one face to the opposite, and densely distributed over the whole surface. The channels are always inclined with respect to the plate surface. This ensures that electrons entering the channel will definitely collide with a wall resulting in an electron cascade. Thus, the original signal is being amplified by several orders of magnitude depending on the strength of the electrical field and the geometry of the micro-channel plates. To ensure that the current will flow, the high voltage on the collector is always a little higher than that applied to the cathode. The typical current after amplification lies in the range of 10-100 nA. This current can be recorded as a function of the photon excitation energy.

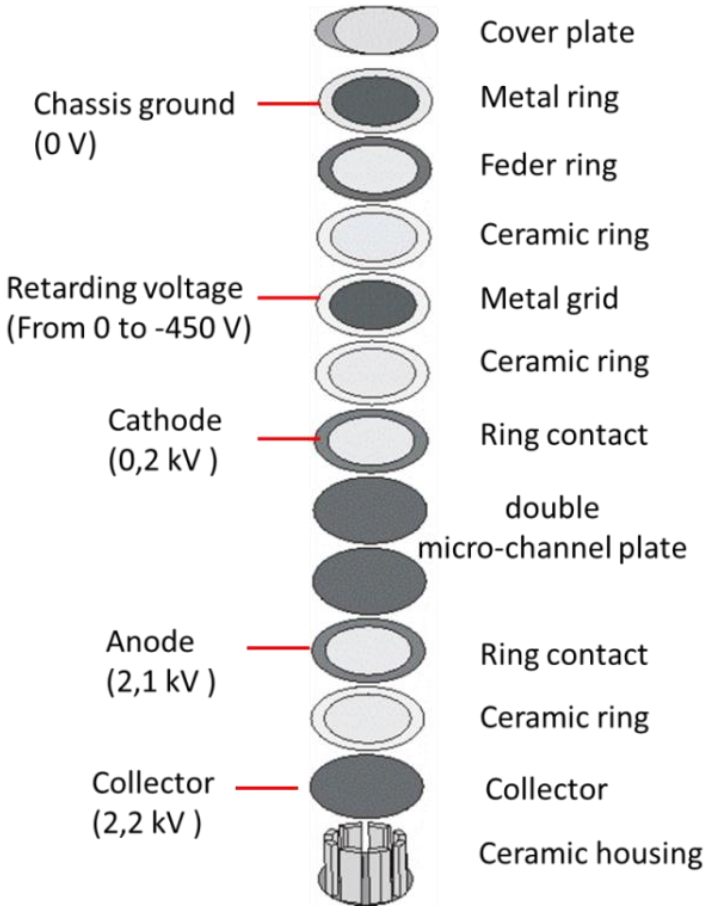

Fig. 3.13.: Schematic view of NEXAFS detector.

3.6. Processing of the NEXAFS spectra

The scheme of the NEXAFS experiment is presented in Fig. 3.14. The synchrotron radiation is monochromatized by the spherical grating monochromator and enters the analysis chamber. For the photon energy scale calibration a gold mesh is placed in the way of the beam propagation, just in front of the entrance to the analysis chamber. The drain current resulting from the gold mesh interaction with the radiation is measured with a multimeter and called the I_0 signal. The gold mesh always contains a certain amount of carbon contamination; therefore a strong signal corresponding to carbon is always present. The I_0 signal is always recorded simultaneously with a signal from the MCP NEXAFS detector as a function of photon energy. The raw NEXAFS data cannot be used to retrieve the MO average angles as described in section 2.3 for a number of reasons. The different thickness of the organic films will result in the different intensity of the obtained NEXAFS spectra. Angle resolved measurements will also lead to the intensity variation due to the different size of the radiation footprint at grazing and normal incidence.

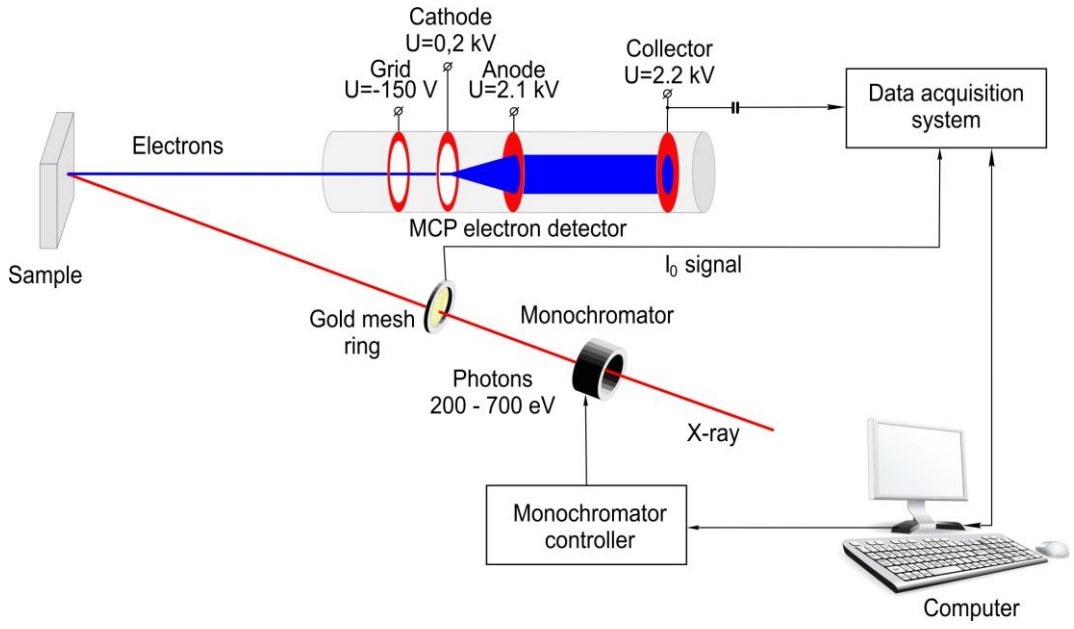

Fig. 3.14.: Schematic view of the NEXAFS measurement.

To obtain the comparable NEXAFS spectra, which are presented in the experimental part of this thesis, the raw data are subjected to a processing procedure presented below. The procedure can be subdivided in several steps.

a) Photon energy scale correction. The first fact to be considered is that the photon energy scale may shift from time to time. Since the electrons orbit has no constant trajectory, the radiation beam may fall on the monochromator each time under slightly different angle leading to slight variations in the photon energy of the monochromatized light. To control this shift the following procedure should be performed for every measured spectrum. The position of the resonance coming from the carbon contamintation on the gold mesh should be compared to the reference value of this resonance (284,81 eV). If the value of the carbon resonance on the gold grid of the measured spectrum doesn't match the reference value, the photon energy scale should be shifted accordingly to eliminate this difference.

It is also necessary from time to time to control the energy position of the carbon contamination on the gold grid. This can be done according to the following procedure. The NEXAFS spectrum for HOPG is measured together with I_0 signal coming from the gold mesh. The measured π^* resonance energy position of the graphite is compared to the reference value of this resonance (285.41 eV), which can be found for instance in [56]. If the position of the π^* resonance is different from the value reported in the literature the photon energy scale should be shifted to match this position exactly. This way the reference position of the resonance on the gold mesh is defined. This procedure should be performed at least once every 3 months to make sure that the reference value is still correct.

b) Background correction. For all measured spectra there is a background which should always be considered. This is usually a constant signal measured with a closed beam

shutter and stemming from the electronics, its value is normally very low (0,2-2% of the whole signal). However, if the amount of the adsorbed molecules is small even this background may have a significant influence on the spectra. This background constant signal must be subtracted from all spectra.

c) Substrate subtraction The NEXAFS spectra measured in the experiments presented in this thesis are a sum of the signal coming from both organic top layer and substrate. To isolate the signal from the organic adsorbate, the signal from the clean substrate should be measured separately and then subtracted from the signal measured for the substrate covered by adsorbate. To do this properly a normalization step is required. The signal from the substrate is multiplied by the some coefficient so that after subtraction the foot of the absorption jump will turn to zero.

d) Photon flux correction. The photon flux of the synchrotron is not constant, and depends on the wavelength as shown earlier (Fig. 3.2). Normalization can be carried out by measuring the transmission function (NEXAFS spectrum of a clean gold wafer). Then, the experimental NEXAFS data can be normalized dividing the spectrum by the transmission function. For convenience the maximum of the transmission function is normalized to 1.

e) Normalization to the height of absorption step. The NEXAFS data are collected for different incidence angles ranging from small incidence angles to a normal incidence angles. The size of the radiation spot will be bigger, if the samples are irradiated at grazing incidence and smaller if irradiated at normal incidence. To eliminate this difference, the spectra are normalized (i.e. multiplied by a factor) to yield an edge-step with a height equal to 1.

The flow diagram of the raw NEXAFS data processing on the example of azobenzene adsorbed on rutile TiO_2(110) is presented in Fig. 3.15.

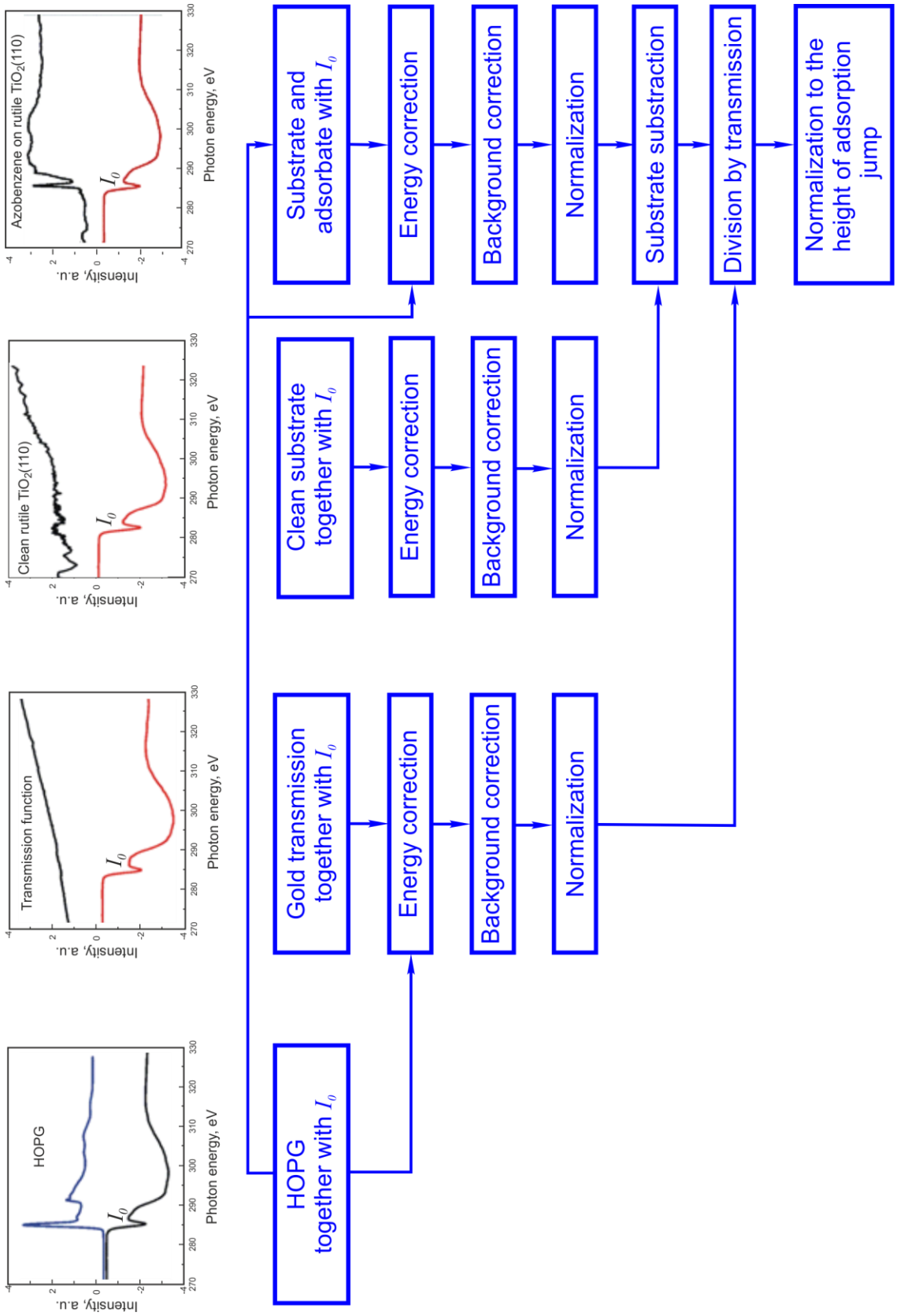

Fig. 3.15.: Flow diagram of the NEXAFS spectra processing procedure.

4. CALCULATIONS OF NEXAFS SPECTRA

The correct interpretation of the experimental NEXAFS spectra is important for drawing the appropriate conclusions about molecular structure, orientation, etc. To make a proper assignment of the resonances observed in the experimental spectra different methods and approaches can be used. Originally, for the analysis and interpretation of experimentally obtained NEXAFS spectra the empirical method known as "building block" principle was applied [58, 59]. This method assumes the decomposition of the NEXAFS spectrum of some complex molecule into small constituents parts (building blocks) with a known spectrum (measured and analyzed before). The building block principle may simplify the assignment of the observed resonances to the different chemical groups which are present in the molecule. However, due to the high complexity of some molecules and therefore different contributions from chemically shifted species, the X-ray absorption bands in the spectrum may overlap each other making the separation and assignment of different resonances a challenging task. For this reason the practical realization of the building block principle is not always possible. Another approach is to use different methods of computational quantum chemistry for the calculation of the NEXAFS spectra [59]. The most detailed and accurate result may be provided by ab initio electronic structure methods. For instance in paper [12] the calculation of the NEXAFS spectrum for free benzene molecule as well as for the molecule adsorbed on r-TiO_2(110) surface was performed using ab initio methods. Unfortunately, ab initio methods often require a lot of computational space, a powerful computer cluster and are very time consuming. Another alternative is to conduct the calculation of the NEXAFS spectrum of the molecule in the gas phase using software which is based on the realization of the linear combination of gaussian type orbitals - MO solution of the Kohn-Sham DFT equations. The calculation is performed for each atom separately. The bonding of each

particular atom with its neighbor will define the presence and energy positions of π^* and σ^* resonances. The summation of the calculated spectra obtained for each atom will yield the spectrum of the whole molecule. This method is not so time consuming when compared with the ab initio calculation and requires less powerful computer cluster. In this thesis this particular approach was applied for the calculation of NEXAFS spectra using the computational software StoBe. Here the examples of the calculated spectra for both simple and more complex molecules are presented.

4.1. StoBe package

The interpretation of all experiments presented in this thesis was supported by the calculation of the free molecules in the gas phase by using the StoBe software package [64]. The software package StoBe is a numerical program package which allows to evaluate and analyze the electronic structure as well as spectroscopic and other properties of molecules and atom clusters. The approach is based on self-consistent solutions of the Kohn-Sham density functional theory equations using the linear combination of atomic orbitals (LCAO) approach [63, 64]. The package predicts the energy and the intensity of the electronic transitions from the core level to the lowest unoccupied molecular orbital (LUMO) for each atom separately. The sum of the transitions for each atom will result into the NEXAFS spectra of the molecule. The present StoBe version for Linux allows performing such computations for molecule clusters of up to 140 atoms. The StoBe input file consists of keywords. By calling a keyword the user can activate or deactivate the option(s) associated with that keyword. For certain options the user must also assign numbers, such as the convergence criteria for the self-consistent field procedure (SCF). The manual concerning StoBe usage can be found on the web [64]. A list of StoBe basic keywords and examples of StoBe input files are listed in Appendix A.

4.1.1 Density functional theory

Density functional theory (DFT) is a quantum mechanical method widely used to describe the electronic structure of microscopic systems consisting of a large number of interacting atoms. Such systems may include atoms, molecules, crystals etc. The property of the system is defined by the positions of the atoms' nuclei and their electrons. If a given set of electrons is moving in the field of nuclei, the lowest energy configuration of the electrons can be determined. The state with the lowest energy is called the ground state of the electrons.

Since nuclei are much heavier than electrons and are fixed in space, the Born-Oppenheimer approximation [61] can be applied. Then the coordinates of the nuclei can be treated as parameters. Let the position of electron in a system be defined by a vector $\mathbf{r_i}, i = 1, 2, ...N$. Then, the probability of N electrons to be coordinates, $\mathbf{r_1}, \mathbf{r_2}, ...\mathbf{r_N}$, is defined by

$$\Psi^*(\mathbf{r_1}, \mathbf{r_2}, ...\mathbf{r_N})\Psi(\mathbf{r_1}, \mathbf{r_2}, ...\mathbf{r_N}) = \left|\Psi(\mathbf{r_1}, \mathbf{r_2}, ...\mathbf{r_N})\right|^2$$

where $\Psi(\mathbf{r_1}, \mathbf{r_2}, ...\mathbf{r_N})$ is the wave function. The asterisk indicates a complex conjugate. This probability is closely related to the density of electrons at a point in space, $n(\mathbf{r})$. The density of electron can be written in terms of the individual electron wave functions as

$$n(\mathbf{r}) = 2\sum_i \Psi_i^*(\mathbf{r})\Psi_i(\mathbf{r})$$

where summation is carried out over all individual wave functions $\Psi_i(\mathbf{r})$ occupied by electrons. The term inside the summation defines the probability that an electron

having the wave function $\Psi_i(\mathbf{r})$ is located at position $\mathbf{r}$. It is important that the electron density, n(**r**), a function of three coordinates, contains the information in full wave function solution of the Schrödinger equation, which is a function of 3N coordinates.

The density functional theory rests on two mathematical theorems proved by Kohn and Hohenberg [60-63]. The first theorem states that the ground-state energy derived by solution of Schrödinger's equation is a unique functional of the electron density. Thus, this theorem states that there exists a unique mapping between the ground-state wave function and the ground-state electron density.

The second theorem defines an important property of the functional: the electron density that minimizes the energy of the overall functional is the true electron density corresponding to the full solution of the Schrodinger equation. If the true functional form was known, we could vary the electron density until the energy from the functional is minimized, giving us a possibility for finding the corresponding electron density.

The first step to solve the problem is to use the Hohenberg–Kohn equation for the single-electron wave functions, $\Psi_i(\mathbf{r})$ [63]. The energy functional can be written as

$$E\left[\{\Psi_i\}\right] = E_{known}\left[\{\Psi_i\}\right] + E_{XC}\left[\{\Psi_i\}\right]$$

where $E_{known}\left[\{\Psi_i\}\right]$ is a collection of terms we can write down in a simple analytical form, and $E_{XC}\left[\{\Psi_i\}\right]$includes all other terms. Thus, the Hohenberg–Kohn equation depends on the potential functionals V_{known} and V_{XC} which in turn depend on $n(\mathbf{r})$.

The problem may be solved by iteration using the following algorithm:

1. Define an initial, trial electron density, $n(\mathbf{r})$.

2. Solve the Kohn–Sham equations defined using the trial electron density to find the single-particle wave functions, Ψ_i.

3. Calculate the electron density $n_{KS}(\mathbf{r})$ defined by the Kohn–Sham single particle wave functions from step 2,

$$n_{KS}(\mathbf{r}) = 2\sum_i \Psi_i^*(\mathbf{r})\Psi_i(\mathbf{r}).$$

4. Compare the calculated electron density, $n_{KS}(\mathbf{r})$, with the initial electron density $n(\mathbf{r})$ used in solving the Kohn–Sham equations. If the two densities are the same, then this is the ground-state electron density, and it can be used to compute the total energy. If the two densities are different, then the trial electron density must be updated in some way. Once this is done, the process begins again from step 2.

4.2. Examples of StoBe calculation for simple aromatic molecules in the gas phase

As it has been mentioned at the beginning of the chapter, a building block principle is not always applicable for the interpretation of NEXAFS results. A good example of the building block principle limitation can be a π* resonance splitting observed for benzene derivatives and the absence of this splitting for benzene. NEXAFS spectra of aromatic molecules like aniline (C_6H_5NH) or monofluorobenzene (C_6H_5F) demonstrates a double resonance around 285.5 eV [56]. However, on the NEXAFS spectrum for benzene this resonance is single. It is not surprising because there are two degenerated LUMO orbitals with the same energy according to MO diagram for benzene (Fig. 2.9). In the case of aniline and monoflurobenzene a symmetry reduction leads to the separation of these orbitals in energy, and therefore a splitting of π* resonances is observed. Here, the StoBe simulated C K-edge NEXAFS spectra for benzene, aniline and fluorobenzene are

presented to prove this fact and to demonstrate the power of StoBe calculations. In Fig. 4.1 the simulated C K-edge spectrum of benzene shows two pronounced π^* resonances**.** The corresponding spectrum of aniline, shows a similar profile, but a distinct splitting of the first π^* is present. Calculated NEXAFS spectrum of the fluorobenzene molecule demonstrated the larger splitting of the first π^* resonance. The splitting of the second π^* resonance is not so apparent, but still visible if the NEXAFS spectrum of benzene is carefully compared with those of aniline and fluorobenzene. The results are in a very good agreement with experimental results presented in [56] and demonstrate a high reliability of the StoBe calculations.

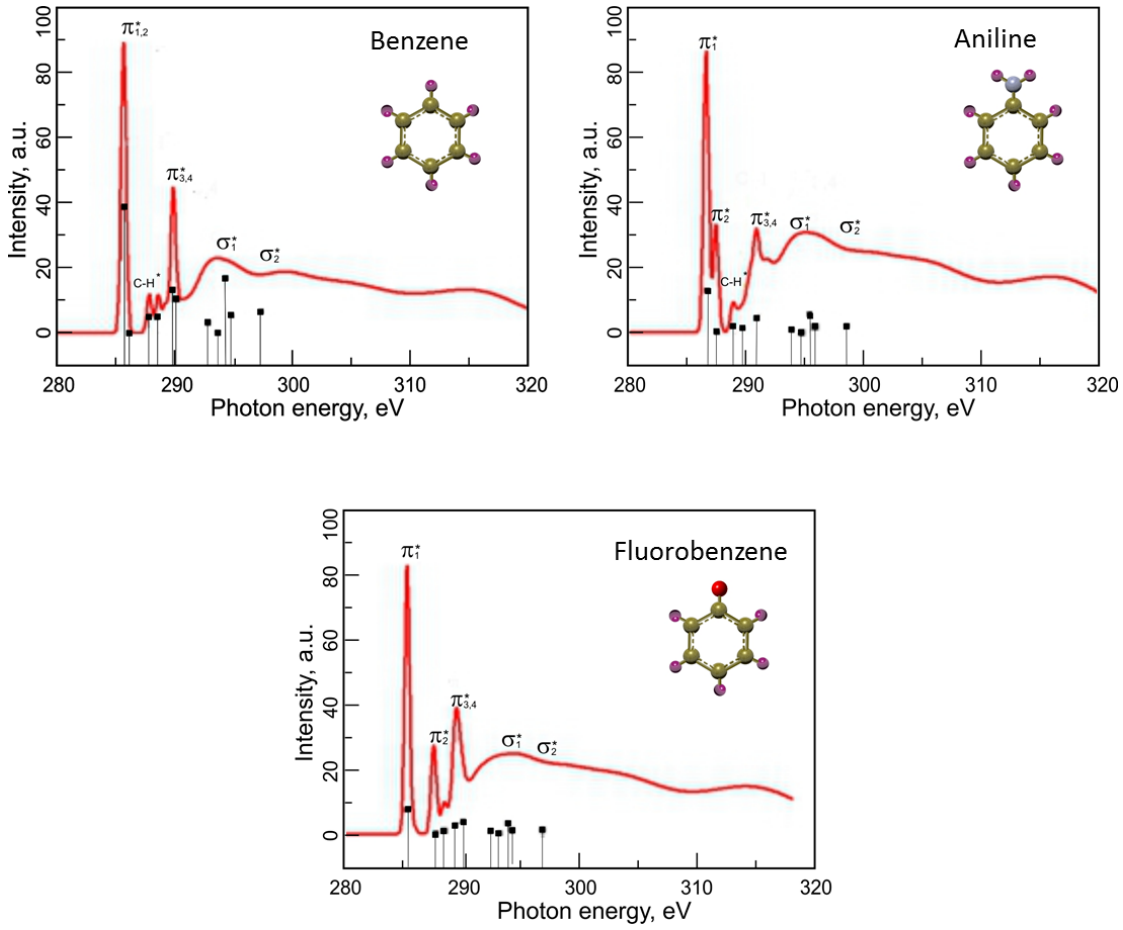

Fig. 4.1.: Simulated C K-edge NEXAFS spectra computed using StoBe for different free molecules: benzene, aniline, fluorobenzene.

4.2.1 Example of StoBe calculations for complicated molecules in the gas phase

The StoBe calculations were demonstrated to be effective for more complicated molecules. An interesting case is the triazatriangulenium molecule (TATA) platform functionalized with azobenzene employed for the preparation of azobenzene adlayers and its derivatives which are a promising approach for the photoswitching due to the possibility of azobenzene to exist in two isomers (trans-, cis-). Details concerning the TATA platform molecule functionalized with azobenzene including applications can be found in [67-69]. StoBe simulation of NEXAFS spectra of triazatriangulenium platform functionalized with azobenzene (Azo-TATA) were performed in context of this work. The models of the TATA platform ion and Azo-TATA are presented in Fig. 4.2. To simplify the interpretation of the calculated spectra the molecule was subdivided into 3 main components: TATA platform cation (platform), azobenzene (functional group) and a bridge between the TATA platform and azobenzene consisting of 2 carbon atoms joined with the triple bond (spacer). StoBe simulation of C K-edge NEXAFS spectra of Azo-TATA together with schematic presentation of different components of the molecule is presented in Fig.4.3. Six distinct resonances marked with A, B, C, D, E, F can be observed. On the curve below the corresponding resonances are marked with the same letter. Analysis of the obtained simulated data shows that the spectrum of Aza-TATA is dominated by the contribution from the azobenzene component. In particular resonances A and F originate from the azobenzene component only.

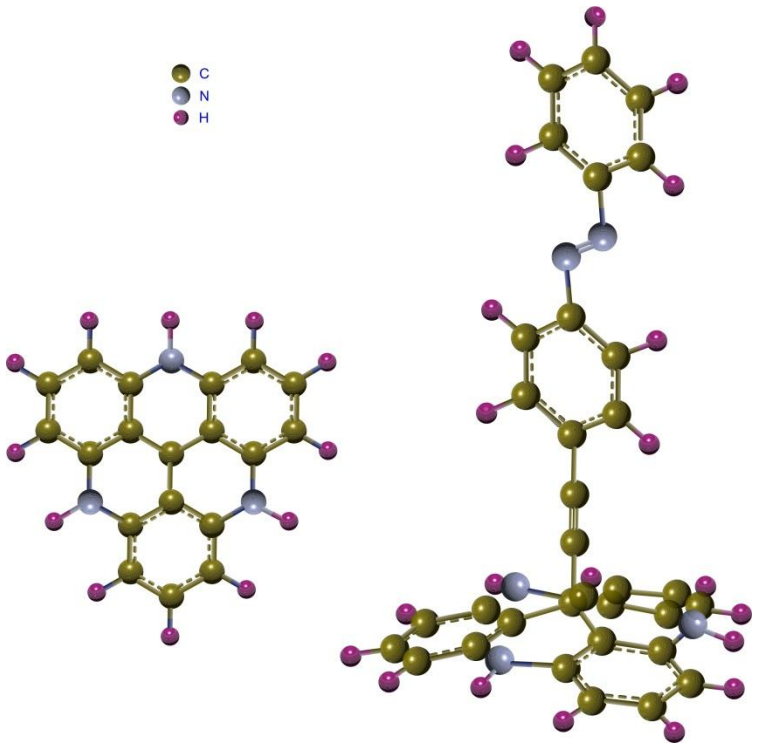

Fig. 4.2.: TATA platform cation (left). TATA platform cation functionalized with azobenzene in trans isomerization (right).

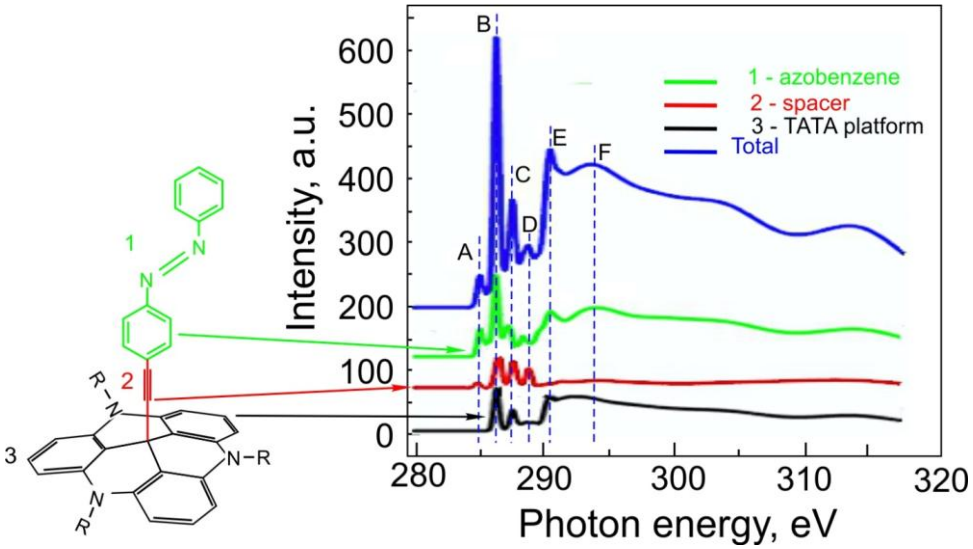

Fig. 4.3.: Different components of the TATA cation functionalized with azobenzene (left). Simulated C K-edge NEXAFS spectrum of the TATA platform functionalized with azobenzene in trans-isomerization. Presentation of the contribution from the different components of the molecule.

In Fig. 4.4 the comparison of simulated C K-edge NEXAFS spectra for azobenzene functionalized TATA cation with experimental results for this system is presented. The

simulated spectra of trans- and cis- configuration show almost no difference, except the position and shape of the small resonance around 284 eV. The simulation is in good agreement with experimental spectrum. Since the simulated spectrum of cis- isomerization resembles the experimental spectrum more, we assume that the molecule has a cis- configuration. Fig. 4.5 presents the N K-edge NEXAFS spectra of TATA platform functionalized with azobenzene in cis- and trans- isomerization with experimental NEXAFS spectrum of the same system. Although the spectra show similar profile of experimental the correspondence is not as strong as for C K-edge. This difference can be related to the TATA interaction with Au (111) substrate.

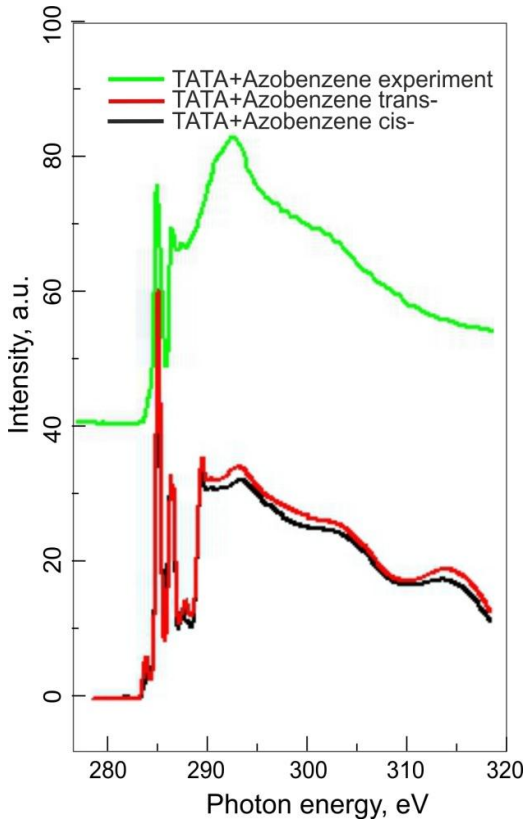

Fig. 4.4.: Comparison of simulated C K-edge NEXAFS spectra of the TATA platform functionalized with azobenzene in cis- and trans- isomerization with the experimental C K-edge NEXAFS spectrum of the same system on Au (111) measured at 55 degrees

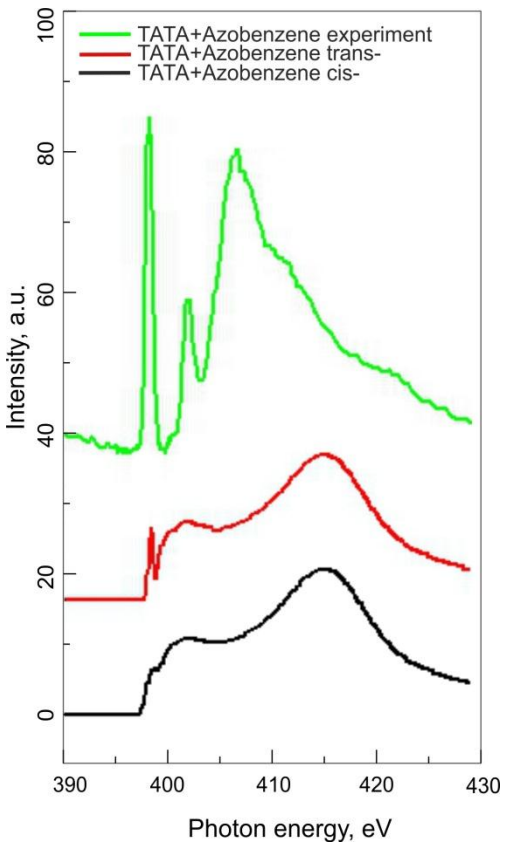

Fig. 4.5.: Comparison of simulated N K-edge NEXAFS spectra of TATA platform functionalized with Azobenzene in cis- and trans- isomerization with the experimental N K-edge spectrum for the same system on Au (111) measured at 55 degrees.

5. STUDY OF TEREPHTHALIC ACID ADSORBED ON RUTILE TiO_2(110) USING NEXAFS SPECTROSCOPY

Controlled chemical functionalization of the surface plays an important role in nano-science. The example of this functionalization can be self-assembled monolayers (SAMs) which refer to the most studied class of molecular assemblies. SAMs of organic molecules are molecular structure which are organized into relatively ordered domains and formed spontaneously on surfaces by adsorption. Most examples of the surface functionalization with organic molecules presented in the literature refer to metal surfaces like gold, silver, copper. However, only a few attempts have been made so far to create a chemically functionalized metal oxide surface by adsorption of organic molecules, even though metal oxide surfaces provide anisotropy and specific adsorption sites that lead to well-ordered monolayers. Terephthalic acid is a molecular linker which has received considerable attention as a linking component for metal organic frameworks. Previous studies on TPA adsorption on r-TiO_2(110) have been reviewed in chapter 1. Briefly, two adsorption models were proposed. Tekiel et al. studied the structure of a complete monolayer of TPA on rutile TiO_2(110) by means of scanning tunneling microscopy (STM) and noncontact atomic force microscopy (NC-AFM). These data indicate that the molecules are oriented upright at coverage of 1 monolayer (ML). The second group studied TPA/TiO_2(110) by means of ab initio DFT calculations. The result of the theoretical work indicates a flat-lying adsorption position of single TPA molecules on a stoichiometric rutile TiO_2(110) surface. Hear a coverage-dependent study of TPA adsorption and structure formation was performed using NEXAFS spectroscopy.

5.1. Theoretical simulation for the free TPA molecule using StoBe Package

Before conducting the experiments a simulation of NEXAFS spectra for the free TPA molecule was performed using StoBe software. The results of the calculation are presented in Fig. 5.1. The TPA molecule has 4 different types of carbon atoms indicated in the inset picture on the right upper side. The curves below, labeled C1, C2, C3, C4, represent the contribution from each separate atom. The curve labeled "Total" represents the whole NEXAFS spectrum for the TPA molecule. On the simulated curve six distinct transition marked with letters A, B, C, D, E, F can be seen. The peaks A, B, C and E are the result of the contribution of the atoms C1, C2, C3 which belong to the benzene ring. The peaks D and F are contributions from the carboxyl group carbon atom labelled C4.

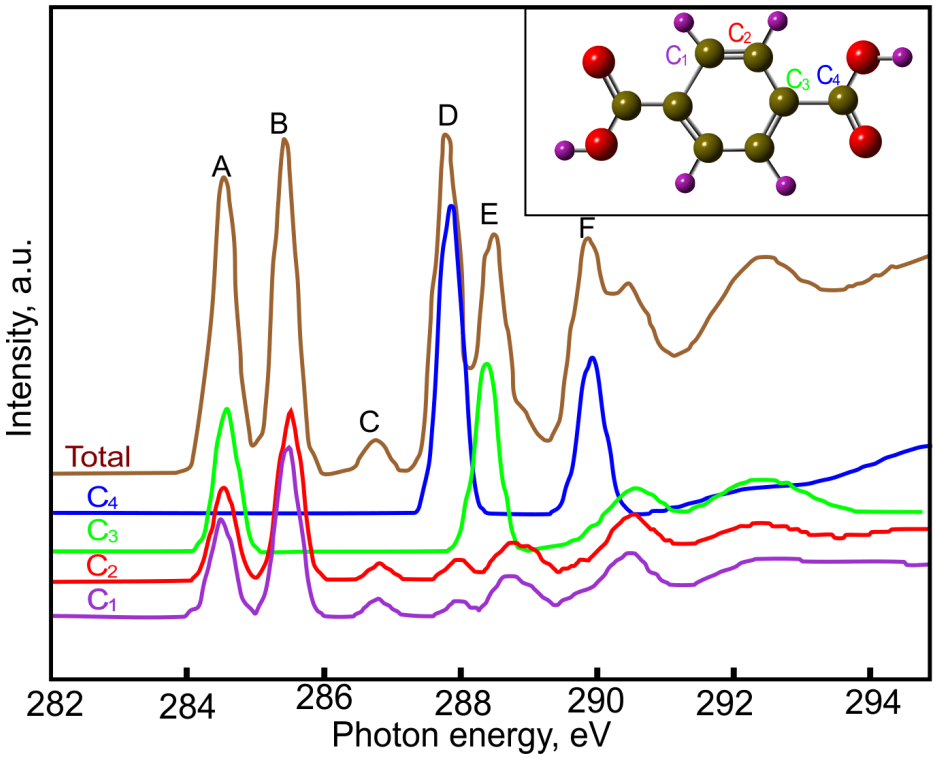

Fig. 5.1.: StoBe-simulated C K-edge NEXAFS spectrum of TPA in the gas phase.

The calculation for the free TPA molecule StoBe simulation simplifies the further interpretation of NEXAFS results and allows making a proper assignment of the observed

resonances. The splitting of the π* resonance around 285 eV coming from the symmetry reduction described in Chapter 4 is observed. Since the results for the StoBe calculation of the TPA ion had very similar appearance one can conclude that it is not possible to distinguish between the intact and deprotonated TPA molecule using NEXAFS spectroscopy as a tool.

5.2. Experimental study of terephthalic acid adsorbed on the rutile TiO_2(110) surface

The NEXAFS experiments were performed in the UHV chamber (see Chapter 3) with a base pressure better than $1x10^{-9}$ mbar. The terephthalic acid in the form of a powder was loaded into the evaporator. The evaporator was attached to the preparation chamber. The rutile TiO_2(110) was mounted on the sample holder with electron bombardment and transferred to the preparation chamber. The preparation procedure consisted of iterating heating and sputtering steps. During the sputtering step the argon pressure was raised to $1x10^{-4}$ mbar, while the accelerating voltage of the sputter gun was set to 1kV, the step lasted each time about 45 minutes. For the heating step the substrate temperature was raised to 1000 K and kept for about 20 minutes. After several heating-sputtering cycles the substrate was transferred to the analyses chamber, where the NEXAFS measurement on the C K-edge was carried out and compared to the reference spectrum of the clean rutile TiO_2(110) surface. This cleaning procedure was continued until the carbon contamination has been completely removed from the surface, since even a small amount of carbon contamination on the surface may have a significant influence on the C K-edge NEXAFS spectrum. Therephthalic acid was deposited on the crystal surface from the gas phase in several steps each lasting 5-15 seconds. The deposition rate measured with a quartz crystal microbalance was set to 0.07 Å/s. The NEXAFS spectra

were recorded after each deposition step for photon incidence angles of 20°, 30°, 55°, 70° and 90°. This made possible to follow the molecular orientation at different coverage starting from the low coverage of 0.07 ML and up to 1 ML. Measurements of the NEXAFS spectra for the C K absorption edge as well as a long spectrum including the C K-, Ti $L_{2,3}$-, and O K- edges at incidence angles θ equal to 20°, 55°, and 90°. By measuring these spectra, it is possible to monitor the increase in the film thickness by taking into account that the jump at the C K absorption edge, i.e. the difference of intensities measured before (E = 278 eV) and after (E =330 eV) the edge, is proportional to the total number of carbon atoms present on the surface. The result of these measurements is presented in Fig. 5.2. The lowest curve in Fig. 5.2 (left panel) presents the NEXAFS spectrum recorded for the pure TiO_2 surface. The absence of any peaks around the C K absorption edge reveals the presence of a very clean substrate prior to deposition of the TPA molecules. After the TPA deposition, the contribution from the TPA layer appears in the NEXAFS spectra (Fig. 5.2 (left panel), middle and topmost curve), while the jump on the Ti absorption edge, that is, the difference of intensities measured at energies 445 and 480 eV, remains the same and can be used for normalization. In Fig. 5.2 (right panel), the dependence of the C K-/Ti $L_{2,3}$-, intensity ratio on the deposition time is presented. We can clearly observe saturation after about 70 s deposition with the crucible at 445 K, which we assign to 1 ML of TPA. On the basis of the saturation behavior one can conclude that a second layer of TPA cannot be grown, or it is very unstable under these conditions.

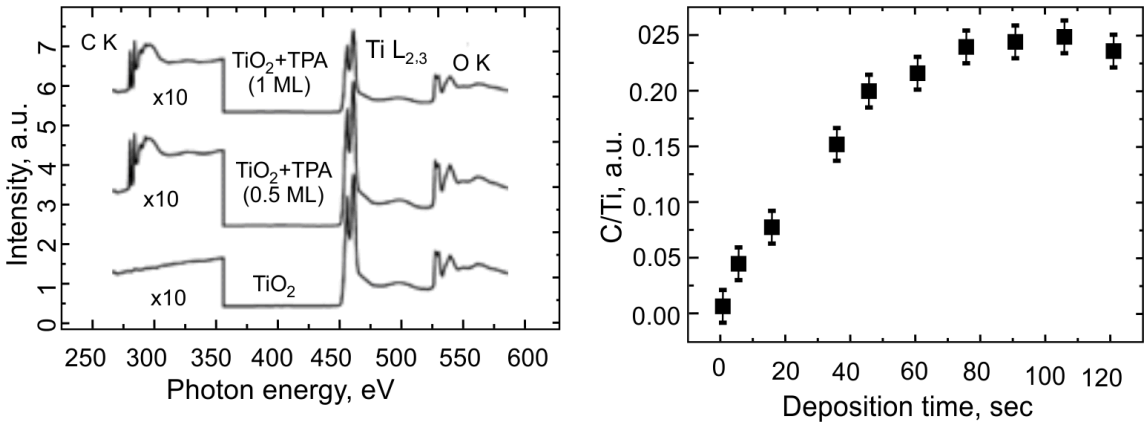

Fig. 5.2.: NEXAFS spectra: (left panel) the TPA/TiO_2(110) system for different TPA coverages at an incident angle of θ = 20°. The signal around the C K absorption edge is multiplied by a factor of 10, and the curves for 0.5 and 1 ML are shifted for clarity; (right panel) C K-/Ti $L_{2,3}$- intensity ratio dependence on deposition time.

In Fig. 5.3 (right panel) the NEXAFS spectra for different angles at the coverage of 0.07 ML are presented. Eight sharp, well-defined peaks are present at the carbon K-edge between 283 and 291 eV The first five peaks (at 284.9, 285.5, 286.8, 288.3, and 290.2 eV, respectively) are assigned to C 1s→π* transitions and the last three (293.2, 297.7, and 301 eV, respectively) to C 1s→σ* transitions [73,74]. The presented spectra demonstrate the clear dependence on resonance intensity of the incidence angle. The pronounced linear dichroism of the peaks at the energies of 284.9 and 285.5 eV, which are related to the phenyl ring, and of the peak at energy 288.3 eV which corresponds to the carbonyl group, indicates almost flat-lying molecules.

In ideal case for TPA molecules in a completely planar adsorption geometry, these peaks should vanish completely for θ = 90°. However, TPA molecules adsorbed at step edges, defect impurities or dislocation sites might have a more tilted geometry and contribute to the NEXAFS signal, as well. In addition, a dynamic tilt angle resulting from the thermal occupation of the low energy vibrations of the molecule might also contribute, as was discussed for the case of benzene adsorbed on the same surface [12].

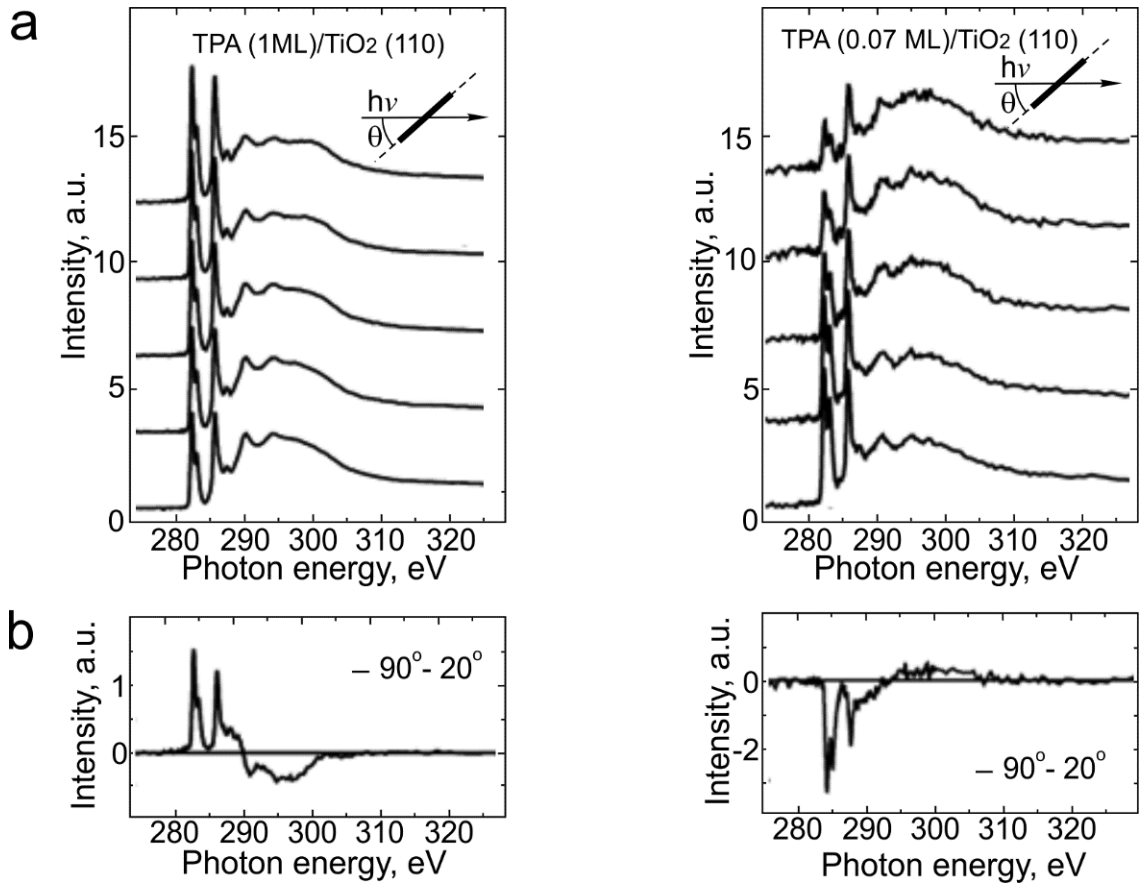

Fig. 5.3.: C K-edge NEXAFS spectra for TPA on TiO_2: (a) 1.0 ML of TPA (left panel) and 0.07 ML of TPA (right panel); (b) difference of the NEXAFS spectra measured at θ = 90° and θ = 20° (linear dichroism).

The NEXAFS spectra for the coverage of 1ML are presented in Fig. 5.3 (left panel). The same set of the resonances as for the low coverage is present. However, the resonance intensity dependence on the incidence angle looks different. The difference spectrum reproduced in Fig. 5.3b (left panel) demonstrates a positive signal for the π* resonances, providing clear evidence of an upright orientation of the TPA molecules on rutile TiO_2(110). Since the phenyl ring can rotate with respect to the carboxyl group, a random azimuthal orientation of the TPA molecules was suggested. According to this model we assumed. Using this model, we calculated an average tilt angle of the molecules of 70 °.

Unfortunately, NEXAFS spectroscopy is blind to the deprotonation of the carboxylic acid group. Therefore, the question as to whether a (bidentate) carboxylate or a protonated

carboxylic acid group binds to the surface cannot be answered on the basis of the present data. The acquisition of XPS O1s data, which are sensitive to the deprotonation is not possible, since the background arising from the substrate oxygen atoms is very high, so this question has to be left unanswered. Since the dissociated hydrogen atoms might diffuse into the bulk and lead to a doping of the substrate the precise mode of adsorption should be determined using vibrational spectroscopy.

5.3. Conclusion

The adsorption of TPA on the rutile TiO_2(110) was investigated using NEXAFS spectroscopy over a wide range of coverages, starting at very low values (a few percent of a monolayer) extending to the saturation coverage of 1 ML. The NEXAFS data reveal a nearly flat-lying geometry of TPA molecules at low coverages (up to ~0.3 ML). The molecules are immobile at room temperature, probably as a result of an anchoring to surface defect sites. Upon increasing molecular dose, the coverage saturates at 1 ML. When saturation coverage is reached, TPA adsorbs in an upright orientation. This makes this system promising for the further functionalization. Moreover the theoretical study of the TPA/TiO_2 by Zasada et al. [74] suggested that the growth of metal organic framework using TPA/TiO_2 system as a substrate should be possible. In addition STM measurements conducted for this system [25] revealed striped structure. This striped structure might be explained by a coverage-dependent interaction of the top carboxyl groups of two neighboring TPA molecules. This might also provide an explanation as to why the coverage saturates at 1 ML. Because of this bonding within the first monolayer, the binding energy to molecules in the second entire layer is expected to be substantially weakened, thus, suggesting why no second layer was observed in this study.

6. INVESTIGATION OF TETRACENE THIN FILMS ON $Al_2O_3/NI_3Al(111)$ SUBSTRATE

In recent years organic semiconductors (OSCs) attract considerable attention due to the still increasing interest in organic electronic devices [75]. Among the different OSC materials polyacenes, polycyclic aromatic hydrocarbons consisting of linearly fused benzene rings, are especially interesting because of their high charge carrier mobility in their crystalline phase. Pentacene, a five-ring polyacene, has been the subject of many works [76-81] but also tetracene (Tc) is of interest with regard to the fabrication of organic field effect transistors (OFETs) [82]. Because of their unique properties polyacenes have also found applications in the fabrication of organic light emitting diodes (OLEDs) [83]. The control over the optical properties of the fluorescent organic layer plays a key role. In this context, the electronic coupling of molecules within thin films to the substrate and in particular the optical quenching of excited states within the molecule by coupling to a supporting metal substrate have to be considered [42,43]. In order to avoid this unwanted quenching, it is common to isolate the organic layer from the metal substrate by a thin insulating oxide barrier [42-45]. In case of tetracene, for instance, a $Ni_3Al(111)$ substrate was oxidized prior to tetracene deposition [42-44] leading to the presence of a thin oxide layer with a thickness of about 0.5 nm. Unexpectedly, however, in this work the luminescence of the thin OSC films deposited on $AlOx/Ni_3Al(111)$ at low temperature was still found to be quenched. However, after annealing to 280 K and subsequent recooling to 100 K quenching was found to be absent [44]. The aim of the present study was to carry out a detailed orientation analysis of tetracene molecules deposited on thin oxide insulating film using NEXAFS and XPS.

6.1. Simulation of the tetracene NEXAFS spectrum in the gas phase

In order to understand the nature of each resonance appearing in NEXAFS spectrum the simulation for the free tetracene molecule was performed using StoBe package. The package is able to predict the transitions intensities between the core level and anti-bonding molecular orbitals π* or σ* for each nonequivalent atom separately. The Gauss View model of the tetracene molecule is presented in Fig. 6.1 (A) in inset and contains five different types of nonequivalent carbon atoms labeled C1, C2, C3, C4, C5. The calculation of the transition intensities for each atom separately is presented below in Fig. 6.1 (B). The summary of the resonance assignments is presented in Table 1.

Table 1: Assignment of the resonances in the NEXAFS spectrum of tetracene adsorbed on Ni_3Al/AlO_x.

Resonance type	Photon energy
π^*_1	284 eV
π^*_2	286 eV
mixed R/h resonances	287-289 eV
σ*	289-325 eV

The NEXAFS spectra are dominated by several pronounced feature: two strong and sharp π* resonances are observed at the energy 284 eV and 286 eV. The peaks observed

in the photon energy region 287-289 eV, refered hear as R/h resonances, are the mixture of resonances coming from Rydber orbitals and hydrogen derived σ* orbitals (C-H bonds) [85]. The broad features observed between 294 and 325 eV refers to the superposition of σ* resonances. The resulting NEXAFS spectrum presented on Fig. 6.1 (A) is compared with an experimental spectrum measured for the tetracene adsorbed on Ag (111) at 55 degrees demonstrating quite a good correspondence Fig. 6.2.

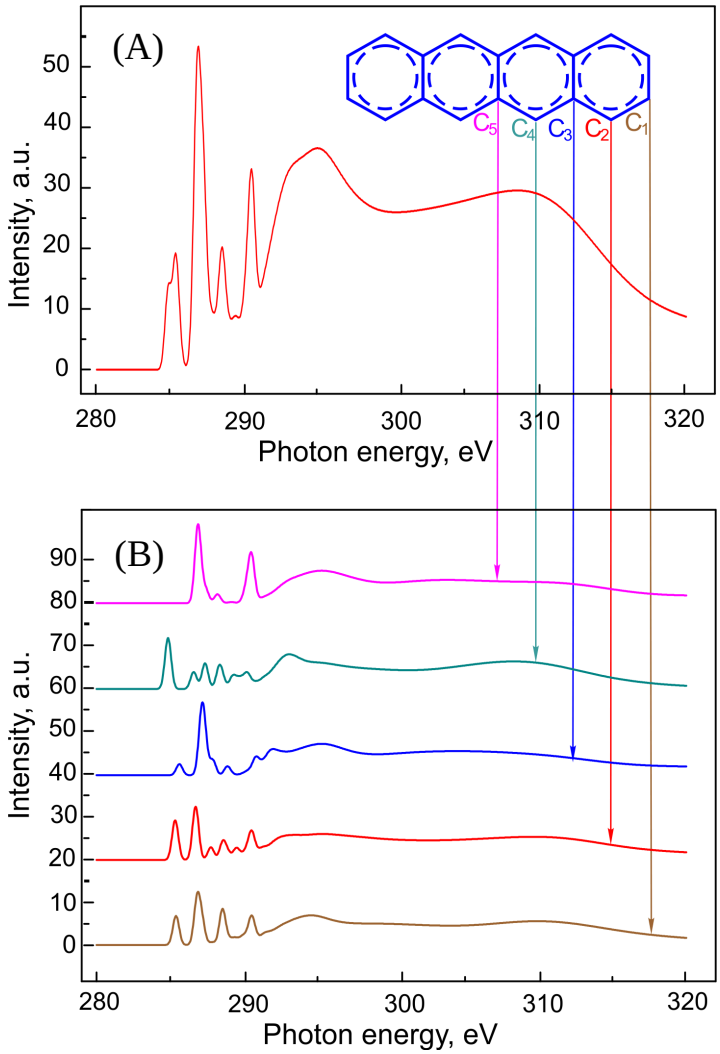

Fig. 6.1.: StoBe simulation for the free tetracene molecule: (A) calculated total NEXAFS spectrum for free tetracene molecule, (B) Calculation of the C 1s→LUMO, LUMO+1… LUMO+n transitions for each nonequivalent atom.

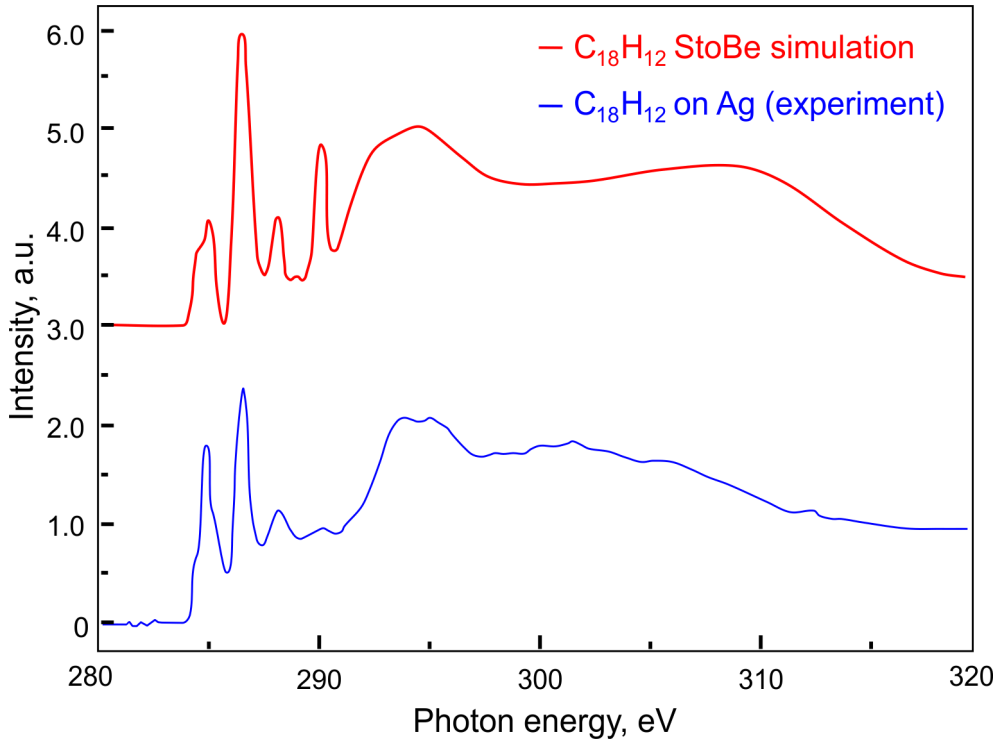

Fig. 6.2.: StoBe simulation for free tetracene molecule compared with experimental result obtained for the tetracene adsorbed on Ag (111).

6.2. Experimental part

The experiments were carried out using the experimental set-up described in Chapter 3. The base pressure both in analysis and preparation chambers was better than 7 x 10^{-10} mbar. The $Ni_3Al(111)$ crystal was cleaned by repeated Ar^+ sputtering and annealing cycles. The AlO_x thin film was grown by exposing the crystal surface to 40 L of oxygen under the temperature of 1050 K in the preparation chamber. These preparation conditions are known to guarantee a well-defined two layer AlO_x thin film with a thickness of 0.5 nm. After AlO_x thin film growth the substrate was characterized by LEED in the preparation chamber and XPS in the analysis chamber. In Fig. 6.3 (a) the sharp LEED pattern recorded for the clean $Ni_3Al(111)$ substrate after the substrate cleaning procedure (several Ar^+ sputtering cycles) is shown. The LEED pattern corresponding to the oxidized surface is presented in Fig. 6.3 (b) and shows additional

diffraction spots which correspond to Al_2O_3 superstructure with a typical for Al_2O_3 unit cell parameters (a = 18.0 Å, b = 10.6 Å, γ = 91.15°). Then we control AlO_x/Ni_3Al substrate with XPS. The data recorded at different electron takeoff angles of 0°, 15° and 45° for Ni3s and Al2s lines are presented in Fig. 6.4. The Al2s peak is split in two components placed at 116.6 eV and 119.6 eV. The peak at 116.6 eV decreases with increasing electron takeoff angle together with a Ni3s line and is assigned to Al atoms within the Ni_3Al bulk while the peak at 119.6 eV is assigned to the Al^{3+} ions in the AlO_x oxide layer, in accordance with data presented in [45].

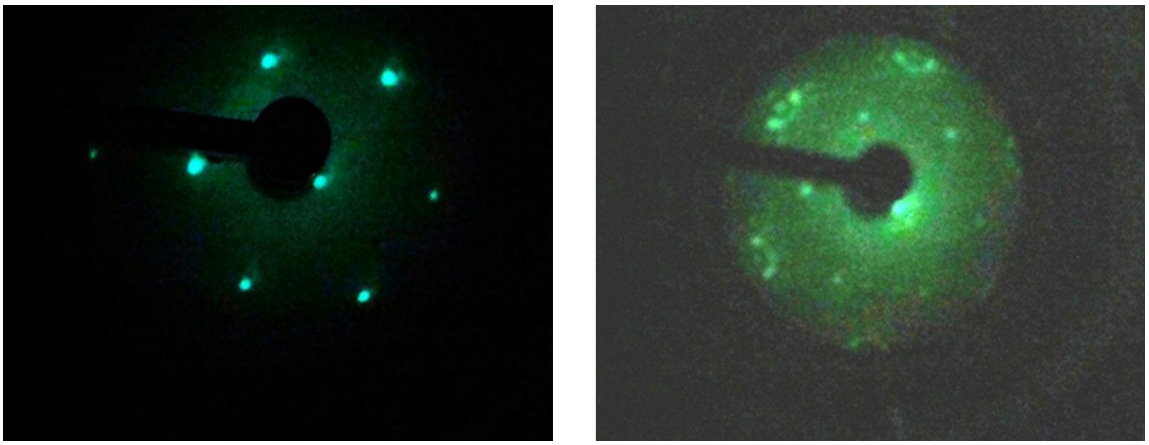

Fig. 6.3.: LEED patterns: clean Ni_3Al (111) surface (left), oxidized Ni_3Al (111) surface (right); images were taken at 93 eV primary energy.

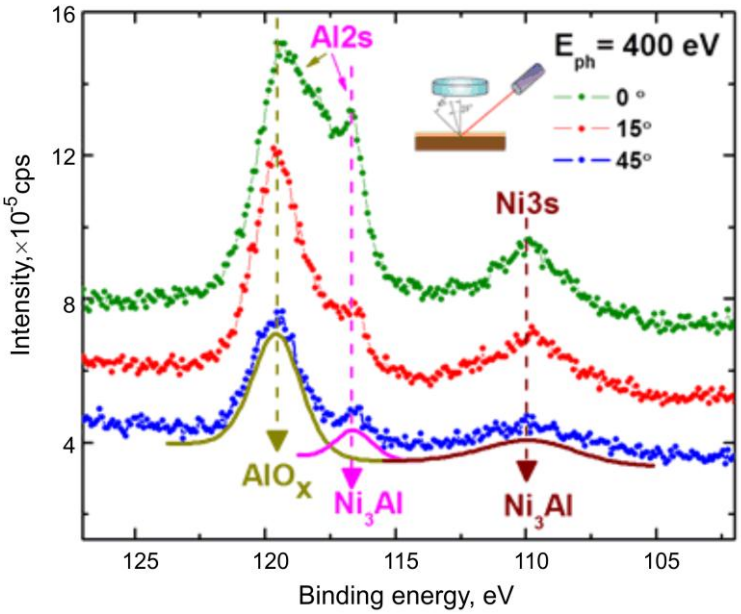

Fig. 6.4.: XPS data recorded for the oxidized Ni_3Al (111) surface measured at different electron take-off angles. Excitation energy 400 eV.

Tetracene (Sigma-Aldrich, 99% purity) was sublimated from a resistively heated quartz crucible and molecular films of different thickness were deposited onto cold (T = 100 K) $AlO_x/Ni_3Al(111)$ substrate. It was shown in previous studies that on oxide-free metal substrates like Ag(111) Tc monolayer forms structures with a long range order, referred to as the a-phase [87]. On $AlO_x/Ni_3Al(111)$, however, no ordered structures showing long-range order have been observed in previous work [45]. For this reason the conditions of Tc monolayer deposition could not be determined on the base of LEED image. Instead, for the preparation of Tc films we applied a deposition protocol (temperature of Knudsen cell, deposition time) developed for ordered monolayer of tetracene on Ag(111), assuming that the sticking coefficient is similar for $AlO_x/Ni_3Al(111)$ and Ag(111) substrate. This protocol was tested in previous NEXAFS experiments in the same UHV system for Tc deposition on Ag(111) [85], where this

procedure was found to be highly reproducible. After tetracene was deposited onto the cold $AlO_x/Ni_3Al(111)$ substrate, the sample was transferred to the analysis chamber. The transfer system of the NEXAFS/XPS set-up with precooled receiving station allows performing a transfer in a very short period of time, so that the temperature of the sample rises only about 18-20 K during transfer. In the analysis chamber the sample was characterized with XPS (excitation energy of 400 eV) and NEXAFS (C-K edge) at the substrate temperature of 100 K. A second set of NEXAFS and XPS data was collected after sample annealing to 280 K and cooling back to 100 K.

6.3 Results for multilayer tetracene films

Firstly we evaporated the tetracene at 150° C for 90 seconds. These parameters should approximately correspond to the growth of Tc multilayer with a thickness of ~3 nm. After deposition the sample was characterized by XPS. The presence of the tetracene multilayer on the surface is evidenced by an intense C1s XPS peak at 285.05 eV (Fig.6.5 (a), black curve). The peak shape and position are in good agreement with previously published results [45]. Upon annealing at 280 K a shift of C1s XPS peak from 285.05 eV to 285.3 eV with significant decrease of the intensity is observed (Fig.6.5 (a), red curve). The decrease of the intensity is explained by the partial desorption of the tetracene upon annealing, while the shift is explained by the higher surface binding energy of the remaining tetracene layer. The XPS Ni3s and Al2s lines are completely suppressed for the freshly deposited multilayer (Fig.6.5 (b), black curve). From this observation the thickness of the tetracene adlayer can be estimated to be larger than 2.1 nm according to NIST electron effective-attenuation-length database [84]. That is in a good agreement with our estimation of the Tc film thickness. Upon annealing of the sample at 280 K, Ni°3s and Al2s XPS peaks reappear in the spectrum (Fig.6.5 (b), red curve). This is

another evidence that a significant portion of tetracene desorbs upon annealing. Although the sublimation temperature of the tetracene is much higher (390 K), the desorption can still be explained by the local heating.

To clarify the question of the molecular orientation for Tc multilayer we used NEXAFS spetroscopy. The corresponding spectra are presented in Fig.6.6 (solid lines). The plots show the typical NEXAFS absorption resonances of tetracene, the positions of which correlate with results obtained for Tc in previous works [85,22].

The NEXAFS spectra are dominated by several pronounced features: two strong π* resonances with an observed fine structure, which are a superposition of at least four C1s→π* transitions at the photon energy range 283-287 eV. The peaks observed in the photon energy region 287-289 eV, are refered here as R/h resonances and are the mixture of resonances coming from Rydberg orbitals and hydrogen derived σ* orbitals (C-H bonds) [85]. The broad features observed between 289 and 325 eV refers to the superposition of σ* resonances. The spectra measured after annealing at 280 K and cooling to 100 K have a very similar appearance and presented in Fig. 6.6 as a dotted lines for 90° and 30° only.

A quantitative analysis of NEXAFS spectra recorded at different photon incident angles θ, allows to determine the average tilt angle of transition dipole moment (TDM) relative to the sample normal, α, can be determined. For substrates with 3-fold or higher symmetry, the intensity depends only on α and θ and not on the molecular azimuthal angle, as described by the following equation:

$$I(\alpha,\theta) = A\left\{\frac{P}{3}\left[1+\frac{1}{2}(3\cos 2\theta - 1)(3\cos 2\alpha - 1)\right] + \frac{1}{2}(1-P)\sin 2\alpha\right\}$$

where A is a constant and P = 0.91 is the polarization factor of the synchrotron light. The analysis performed for the spectra taking before annealing yields an average tilt angle α of approximately 43 ± 5 ° (Fig.6.7, blue squares).

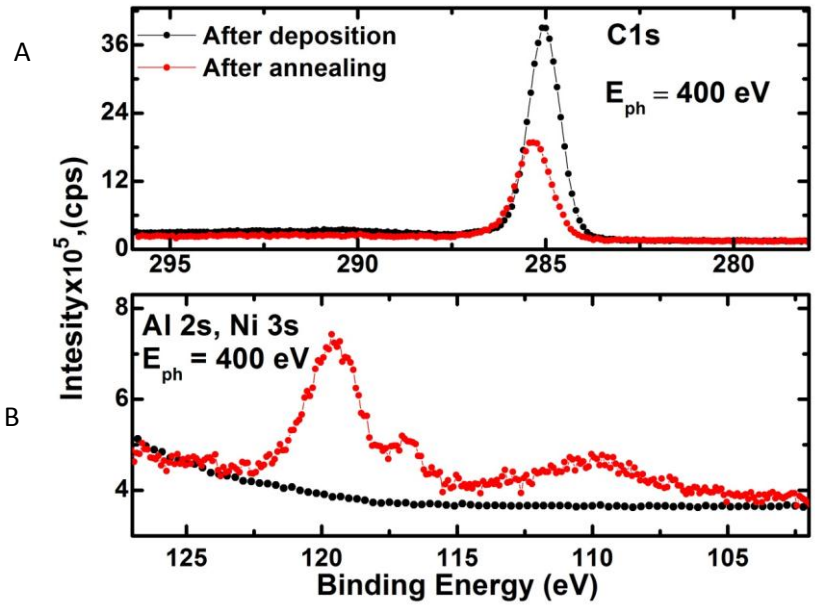

Fig. 6.5.: XPS data for Tc multilayer coverage measured@100 K: (a) C1s directly after Tc deposition (black) , after annealing to 280 K (red); (b) Al2s, Ni3s after Tc deposition (black) , after annealing to 280 K (red);

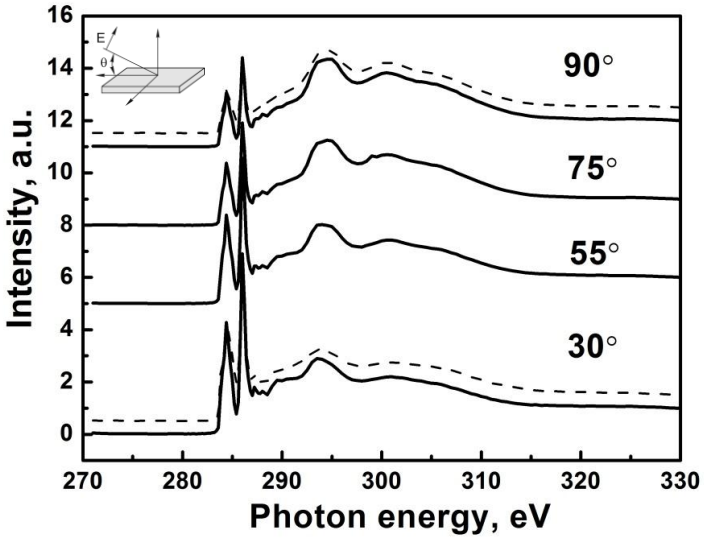

Fig. 6.6.: C K-edge NEXAFS spectra for multilayer measured@100 K: directly after Tc deposition (solid lines), after annealing to 280 K (dashed lines).

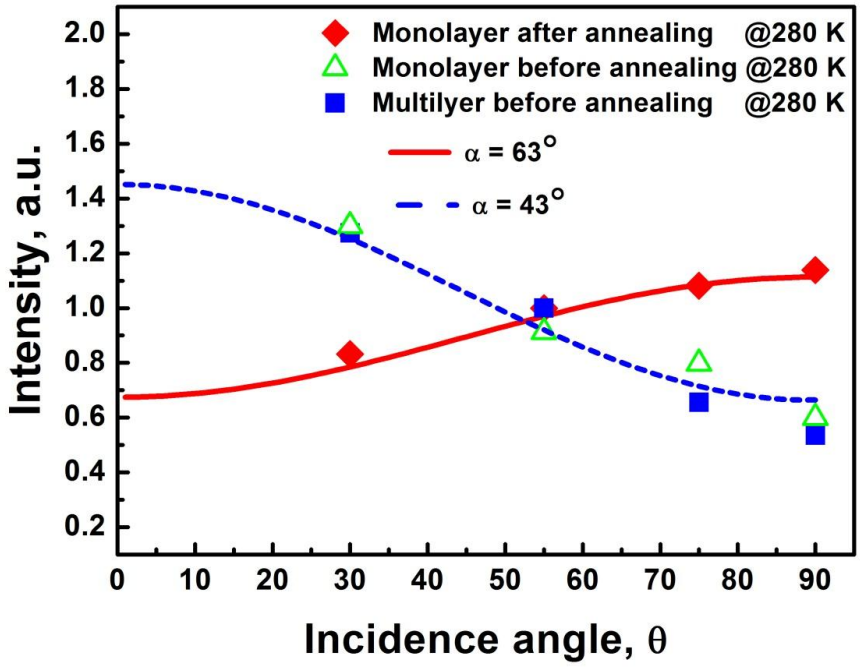

Fig. 6.7.: The angle dependence of the first π* resonance intensity recorded for the tetracene monolayer before and after annealing (green triangles and red diamonds respectively) and multilayer before annealing (blue squares) with corresponding fitting curves

6.4. Results for monolayer tetracene films

A more interesting behavior can be observed for the monolayer (ML) coverage of tetracene. To get a ML thickness, tetracene was evaporated at 130° C for 60 sec in accordance with deposition protocol developed before [85]. The XPS analysis was conducted for the samples directly after Tc deposition. It is noticeable that the position, intensity and full width at half maximum (FWHM) of the C1s peak at BE 285.3 eV of a monolayer tetracene film after deposition (Fig. 6.8(a), black curve) are the same as for the C1s peak for the multilayer upon annealing (see Fig. 6.5(a), red curve). In addition the Ni3s and Al2s lines (Fig. 6.8(b)) are the same as for annealed multilayer sample (Fig. 6.5(b), red curve). NEXAFS spectra recorded for the monolayer of Tc directly after deposition are presented in (Fig. 6.9 (a)). The angle dependance of the NEXAFS

resonances are the same to those presented above for multilayer Tc films and a quantitative analysis of the resonance intensity on angle of incidence yields also an average tilt angle of 42 ± 5° (Fig.6.7, green triangles). This direct comparison of the XPS and NEXAFS data obtained for the Tc monolayer sample and for annealed multilayer sample allows to conclude that upon annealing of the multilayer only about a monolayer of the Tc remains on the surface in accordance with assumption made above.

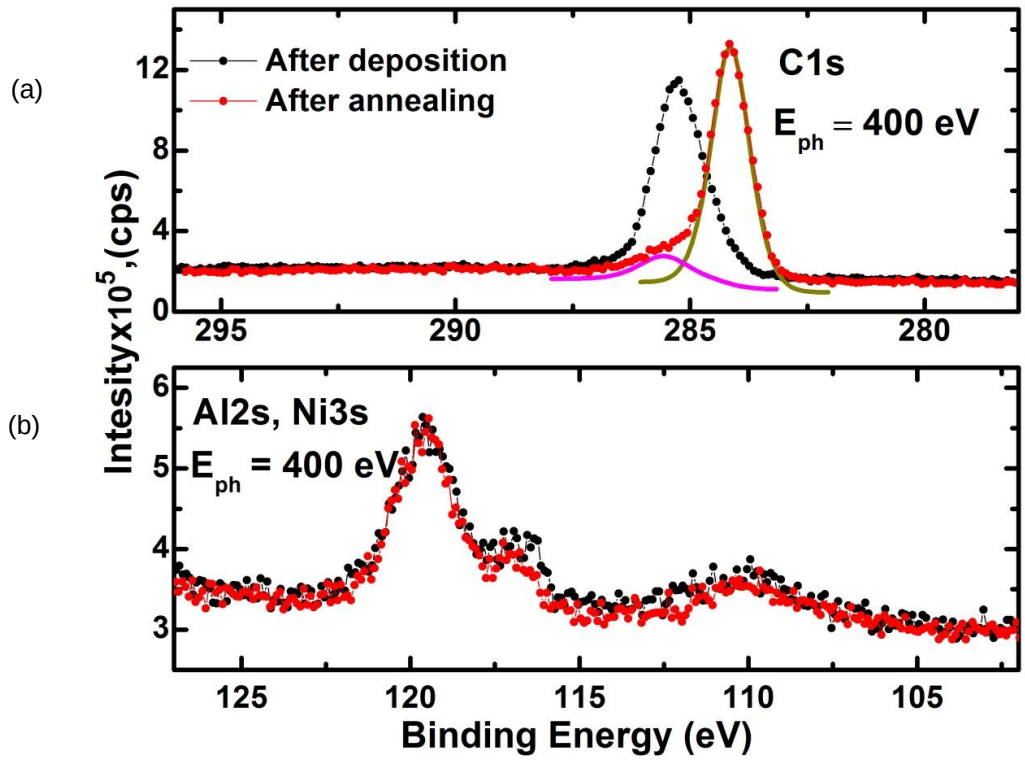

Fig. 6.8.: XPS data for Tc monolayer coverage measured@100 K: (a) C1s directly after Tc deposition (black) , after annealing to 280 K (red); (b) Al2s, Ni3s lines after Tc deposition (black) , after annealing to 280 K (red);

On the basis of our data we propose that before annealing the Tc molecules adopt a structure similar to a disordered variant of the "beta-phase" observed for Tc adsorbed on Ag(111) [85]. In the present case the long axis of the Tc molecule is orientated parallel to the surface with a phenyl ring rotation on 43± 5° (Fig. 6.10(c)). Such a more planar

orientation of the molecule relative to the substrate explains the fact that the C1s binding energy observed for this phase (285.3 eV) is shifted by 0.25 eV relative to the multilayer (285.05 eV). Similar binding energies (~285 eV) were reported for other planar aromatic compounds adsorbed on 3d metals and strongly interacting with a such substrates, e.g. in the case of graphene on Ni(111), where a hybridization of graphene π-orbitals and $3d_z$ orbitals of nickel takes place [89,90]. Although in the present case a thin oxide layer is present, the interaction with the supporting metal is apparently strong enough to cause a ~ 1 eV shift in C1s binding energy.

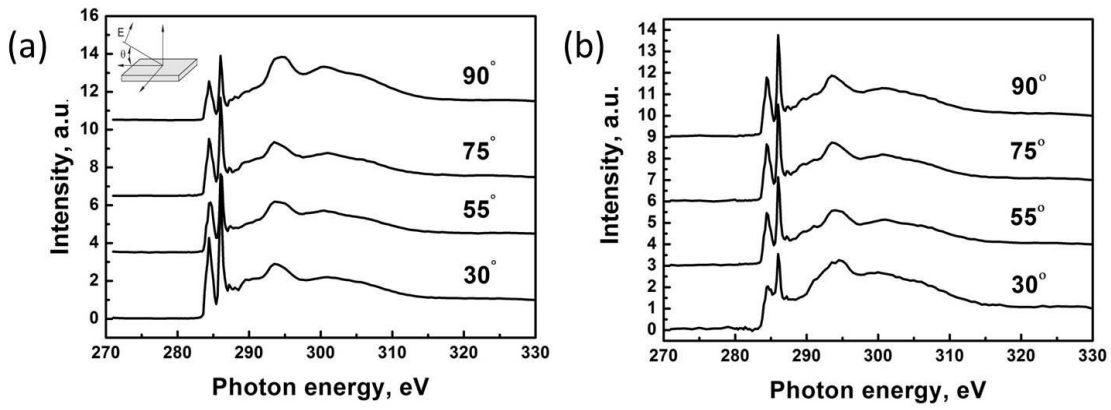

Fig. 6.9: C K-edge NEXAFS spectra for monolayer: (a) before annealing to 280 K and measured@100 K; (b) after annealing to 280 K measured@100 K.

In a next step the deposited monolayer was annealed to 280 K and then cooled back to 100 K. NEXAFS spectra for the annealed Tc monolayer reveal that the dependence of the resonance intensity on the photon incident angle θ shows just the opposite trend (Fig. 6.9(b)) if compared to the Tc monolayer before annealing (Fig. 6.9(a)): The σ*-type resonances are now more intense for grazing incidence while the π*-type resonances are stronger at the normal incidence. The quantitative analysis of the resonance intensity dependence on angle of incidence yields a tilt angle of 63 ± 5° of the Tc molecular plane

relative to the substrate (Fig. 6.7 red diamonds). On the basis of this data we propose an upright orientation of the tetracene molecules with a tilt angle of α=63° between the long axis of the Tc molecule and the surface (see Fig. 6.10(d)).

XPS data collected on the annealed monolayer reveal that the BE of the C1s line changes from 285.3 eV before annealing to 284.1 eV after annealing (Fig. 4(a), red curve). Such a C1s binding energy, 284.1 eV, is fully consistent with an upright orientation of the planar aromatic compound close to a metal substrate. Similar values have been reported for aromatic SAMs on Au substrates, where the planar aromatic subunits adopt a similar, upright orientation [91]. These results correlate also with the previous studies [44,45], where the reorientation of molecules should induce dewetting of the layer and formation of standing molecule islands. Both NEXAFS and XPS results clearly demonstrate the temperature-induced molecular reorientation in the monolayer of tetracene and this reorientation can explain an absence of luminescence directly after Tc deposition and its appearance after corresponding annealing. We would like to mention that a similar behavior was also observed for ethylbenzene and styrene adsorbed on oxygen-terminated FeO(111), where the adsorbate-adsorbate interaction prevailed over adsorbate-substrate interaction. This caused the high tilt angle as well as the growth in the form of two-dimensional islands [88].

Conclusion

In our study we determined the molecular orientation of tetracene molecules on thin well-defined aluminum oxide films supported on a $Ni_3Al(111)$ substrate using XPS and NEXAFS spectroscopy. A detailed analysis for the corresponding XPS and NEXAFS data of the deposited tetracene layers was carried out. For Tc multilayers the NEXAFS data reveal an average tilt angle of 43 ± 5° with respect to the surface.

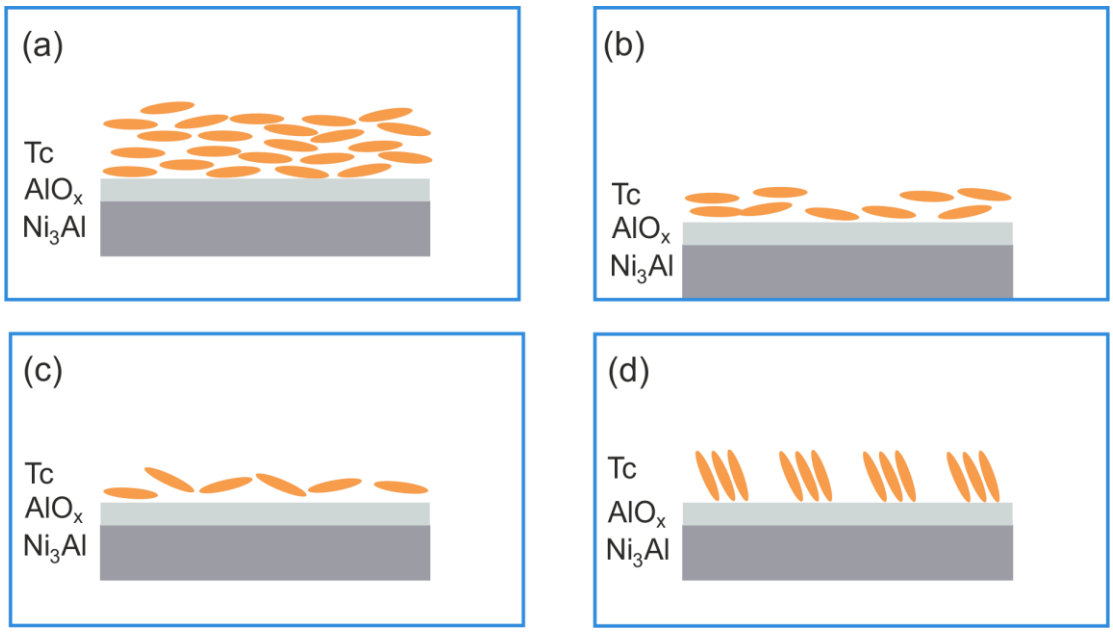

Fig. 6.10.: Tetracene adsorption models: (a) multilayer before annealing to 280 K measured@100 K, (b) after annealing to 280 K K measured@100 K; (c) monolayer before annealing to 280 K measured@100 K, (d) after annealing to 280 K measured@100 K.

This value remains unchanged upon annealing, meanwhile XPS data reveal the partial desorption of the Tc layer (Fig. 6.10(a), (b)). For Tc monolayers a considerable reorientation of the molecules on annealing is found: After deposition onto a cold (100 K) substrate a monolayer of tetracene molecules adopts a disordered adsorption configuration similar to one for Tc multilayer (Fig. 6.10(b), (c)) with molecular platelets tilted (43 ± 5°) with respect to the surface. Upon annealing at 280 K and subsequent cooling to 100 K the film morphology changes and molecular islands with a more up-standing orientation are formed (Fig. 6.10 (d)). These results are a direct experimental confirmation of the hypothesis put forward in previous work [45], where it was suggested that the molecules are adsorbed in a more planar fashion which transform to a more up-standing orientation upon annealing. The C1s binding energy was found to be almost the same for both Tc monolayers directly after deposition and Tc multilayers after annealing, but as soon as molecules in the thin layer undergo reorientation, the binding energy

decreases to values typical for densely packed planar aromatic compounds. To summarize, the obtained results clearly demonstrate that a precise control over the local molecular structure is needed to understand the charge transport in organic semiconductors in close contact with inorganic substrate. The latter is very important for predicting optical properties of the fluorescent organic layer in OLEDs.

7. NEXAFS/XPS STUDY OF AZOBENZENE ADSORBED ON RUTILE TiO_2 (110) SURFACE

In recent years, molecular switches have become interesting since they are promising as future components of the molecular electronic and photonic devices. Azobenzene ($C_{12}H_{10}N_2$) is probably one of the most studied photoswitches [95-101]. Azobenzene and its derivatives (azo molecules) can exist in two configurations (trans- and cis-) presented in Fig. 7.1. These molecules can be switched between two states with photo stimulation at particular wavelengths: i.e. an ultraviolet light excitation corresponding to the energy gap of trans-to-cis conversion, and a blue light is equivalent to that of cis-to-trans conversion. For a variety of reasons, the cis- isomer is less stable than the trans- because it has a distorted configuration, and is less delocalized than the trans- configuration. Thus, cis-azobenzene will thermodynamically turn back to the trans- formation through a cis-to-trans relaxation mechanism.

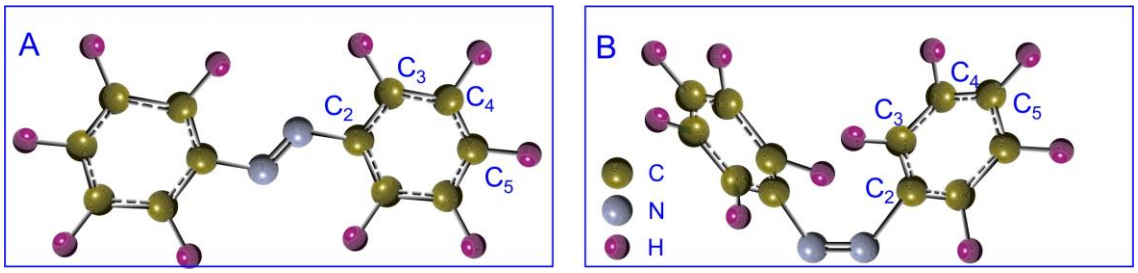

Fig. 7.1.: Azobenzene in trans- (a) and cis- configuration (b).

The integration of molecular switches with inorganic surfaces can give rise to novel hybrid materials in which the properties of the two components are mutually affected or even synergetically enhanced in a reversible fashion. However if azobenzene is adsorbed on the surface its photoswitching efficiency can be largely reduced due to the electronic coupling with substrate or neighbor molecules. For this reason attempts to use the nobel

metals as a substrate often failed. The alternative approach aimed to reduce the electronic coupling may be the use of ultrathing isolating films [95-98] or layered semiconductors [99-101] as a substrate.

The TiO_2 surface may be also a good candidate as a substrate for the flat lying photoswitch. Although, TiO_2 should provide a weak electronic coupling with organic species due to its relatively high band gap about 3-3.4 eV, the TiO_2 surface could be a good candidate for an extraordinary coupling under specific conditions. A number of studies on the azobenzene adsorption on rutile TiO_2(110) and anatase TiO_2(101) temperature was conducted by Li et al., using STM, XPS, and synchrotron-based ultraviolet photoemission spectroscopy [32,102]. They provided the evidence that TiO_2 surface is capable to cleave N═N double bond of azobenzene at room temperature, which leads to a formation of phenylimide (C_6H_5N) in a superstructure assembly. However, the adsorption behavior of azobenzene on rutile TiO_2(110) at low temperatures is still not clear. Therefore, here we provide NEXAFS/XPS results of azobenzene adsorption on TiO_2 in the extended temperature range of 100–290 K.

7.1. Calculation of NEXAFS spectra for cis- and trans- isomers of azobenzene

The preliminary calculation of the NEXAFS spectra is necessary for the better assignment of the resonances during interpretation of the experimental results. For this purpose the simulation of the azobenzene NEXAFS spectra for free azobenzene molecule both for cis- and trans- isomers could be done using StoBe package. According to the symmetry of azobenzene molecule the calculations were performed only for the atoms C1, C2, C3, C4 (see Fig 7.1). Calculated C K-edge NEXAFS spectra for azobenzene in trans-configuration are presented in Fig. 7.2. The curves C1, C2, C3, C4 below represent the

contribution from each separate atom. The summation of these curves yields the spectrum of the whole molecule. The 6 distinct resonances are present and marked with letters A, B, C, D, E, F. The calculation for cis- configuration was performed also the same way.

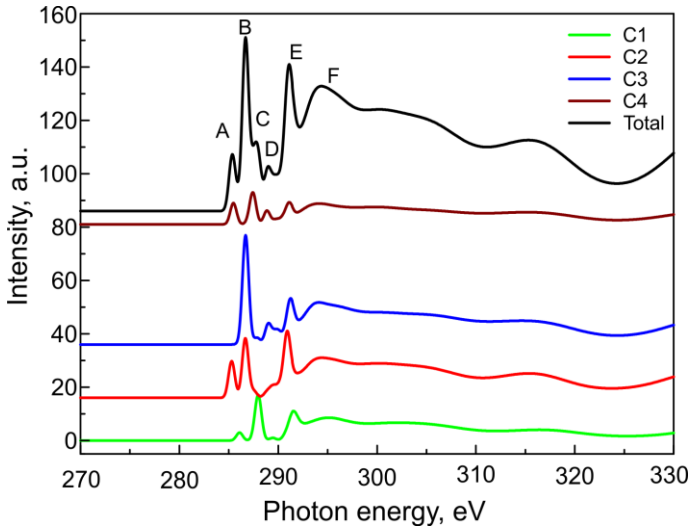

Fig. 7.2.: Simulated C K-edge NEXAFS spectrum of azobenzene in trans-configuration.

In Fig. 7.3 the C K-edge (a) and N K-edge (b) spectra calculated for azobenzene in cis- and trans- configuration are compared to the experimental results for the multilayer of azobenzene adsorbed on the layered semiconductor HfS_2 [101]. The photon energy scale for the StoBe simulated spectra was shifted 1 eV in the direction of low energies to match experimental results, which is a common correction for the StoBe calulations. The simulated spectra for both C K-edge and N K-edge show a good match with the experimental results. Like for the case with StoBe simulation for azo-TATA platform described in chapter 4 a small difference between C-K NEXAFS spectrum for cis- and trans- configuration are visible for the small resonance marked A (Fig. 7.2). At the same time N K-edge spectra for cis- and trans- configuration appear to be very similar. Since the cleavage of the N=N bond of the azobenzene on rutile TiO_2(110) at room temperature, and formation of two phenylimide (C_6H_5N) was observed in the previous work [29] the StoBe simulation has been done for the aniline, which is very similar to phenylimide. The

simulated StoBe results for aniline are presented in Fig. 7.4. C K-edge spectrum of aniline appear to be similar to the C K-edge spectrum of azobenzene, except of the absence of a small pre-resonance (marked A (Fig. 7.2)). At the same time N K-edge spectrum shows a significant difference, since the π* resonance at 400.0 eV is completely absent and only σ* resonance corresponding to C-N bond is visible. Since this particular π* resonance corresponds to the double N=N bond this fact can be utilized in future to distinguish between intact azobenzene molecule and a cleaved one.

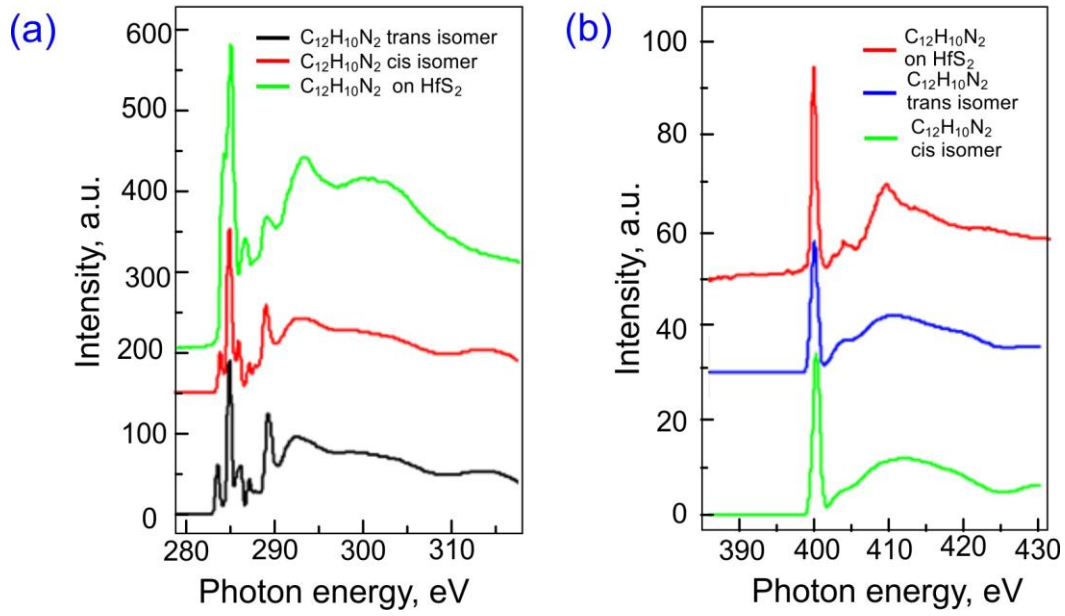

Fig. 7.3.: Comparison of simulated C K-edge (a) and N K-edge (b) NEXAFS spectra of azobenzene in cis- and trans- configuration with experimental spectra of azobenzene measured at 55 degrees. The photon energy scale of the StoBe simulated spectra was shifted 1 eV in the direction of low photon energies.

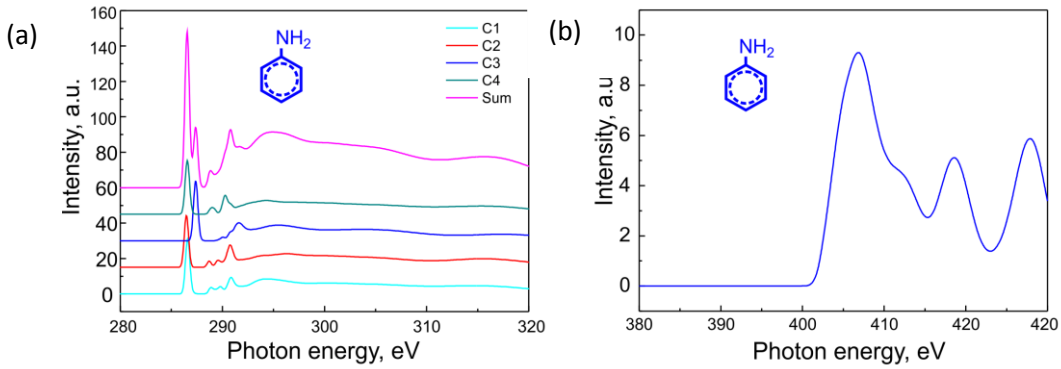

Fig. 7.4.: Calculated C K-edge NEXAFS spectrum (a) and N K-edge NEXAFS spectrum (b) of free aniline molecule.

7.2. Experimental results

The schematic view of the sublimation set-up is presented in Fig.7.5. Azobenzene (Sigma-Aldrich, purity, 99,9 %) was placed in a evacuated metal-glass adaptor which was separated from the analysis chamber by the leak valve.

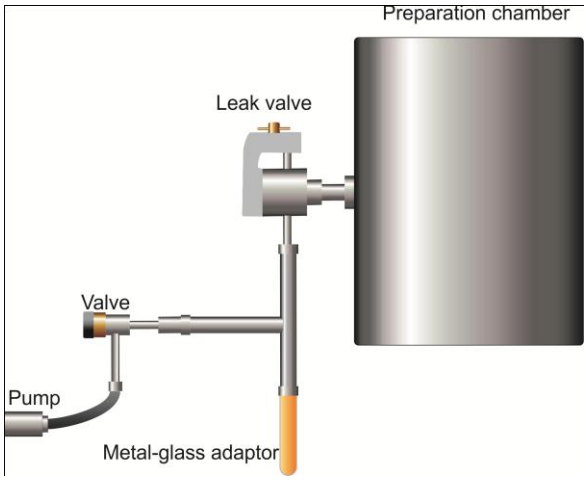

Fig. 7.5.: Scheme of the sublimation set-up

The single crystal of rutile TiO_2(110) (CrysTek GmbH) was prepared according to the standard preparation procedure consisting of a few sputtering and annealing cycles (see Chapter 1.1.3 and Chapter 5.2). The surface quality was checked by LEED. Fig. 7.6

demonstrates LEED image of the freshly prepared rutile TiO_2(110) surface measured at 109 eV. The proportional relation between the distance of neighboring LEED reflexes i.e. between the neighboring atoms in [001] direction and [1-10] direction is 2:1. Assuming that a stick coefficient of the azobenzene to TiO_2 substrate is 1 and 1L = 1.33 x 10^{-6} mbar·s the pressure in the preparation chamber was adjusted to 1.33 x 10^{-8} mbar by opening the leak valve and kept at this level for 100 seconds. After the deposition was finished the sample was transferred to the analysis chamber where NEXAFS and XPS data were collected.

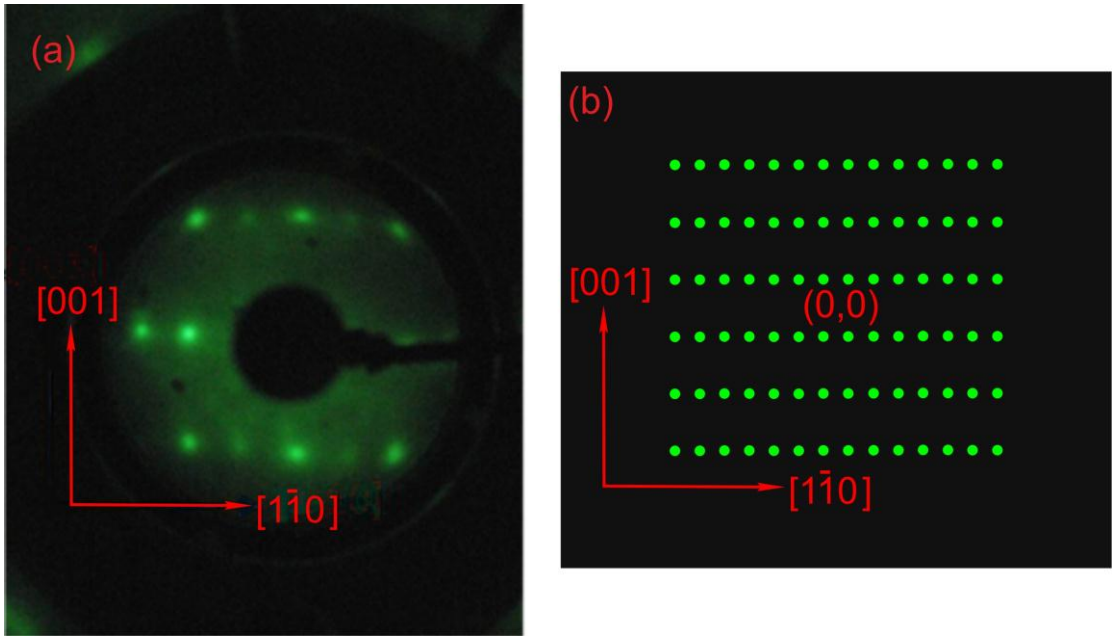

Fig. 7.6.: LEED image of the freshly prepared rutile TiO_2(110) surface measured at 109 eV (a), model of the same LEED image (b).

C K-edge NEXAFS spectra for the azobenzene adsorbed at low temperature measured at the incidence angles 30°, 55°, 75° and 90° are presented in Fig. 7.7. The profiles are in a good agreement with StoBe simulations (Fig. 7.3). The difference of the spectra intensities shows very small dichroism and therefore the exact orientation cannot be determined. The azobenzene N K-edge NEXAFS spectra are presented in Fig. 7.8. The observation of π* resonance for the N K-edge confirms a presence of the N=N double

bond of azobenzene adsorbed on rutile TiO_2(110) surface at the substrate temperature of 100 K. The analysis of the spectra intensities shows the average orientation of the N=N bond of about 45 degrees with respect to the surface.

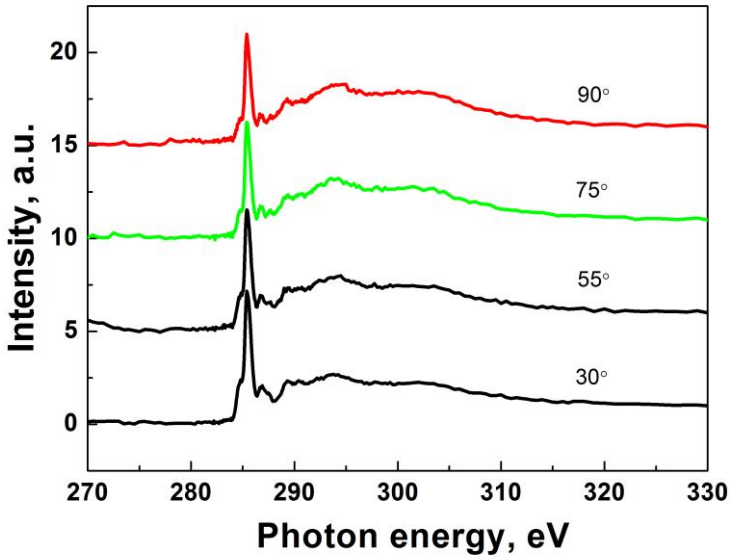

Fig. 7.7.: C K-edge NEXAFS of azobenzene adsorbed on rutile TiO_2(110) at different incidence angles recorded at 100 K.

To find temperature at which N=N bond cleavage observed in the work of Li et al. [29] occurs, NEXAFS measurements were carried out while the sample temperature gradually increased. The measurements results are presented in Fig. 7.9. In the temperature range 120–170 K N K-edge spectra are very similar and still correspond to that of azobenzene. However at 210 K the π* resonance disappears completely and only σ* resonance remains. This mean that N=N bonding cleaved and azobenzene molecule splits into two phenyl imide (C_6H_5N). It is necessary to mention that the spectrum at 210 K is quite similar to the StoBe calculation for the aniline (Fig. 7.4 (b)).

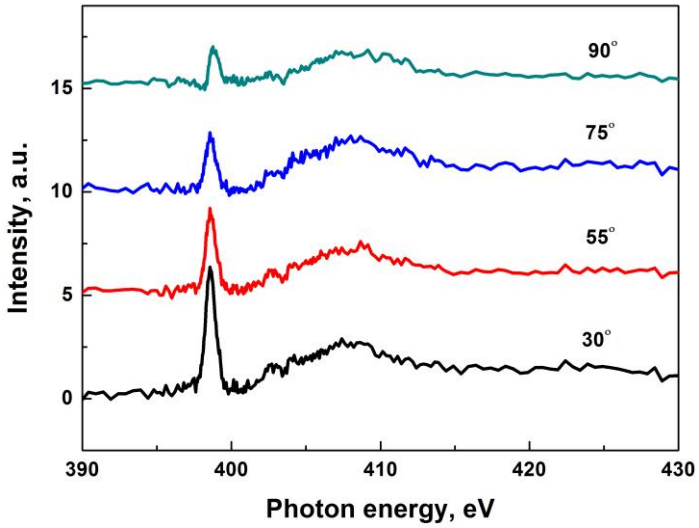

Fig. 7.8.: N K-edge NEXAFS spectra of azobenzene adsorbed on rutile TiO_2(110) at different incidence angles recorded at the temperature 100 K.

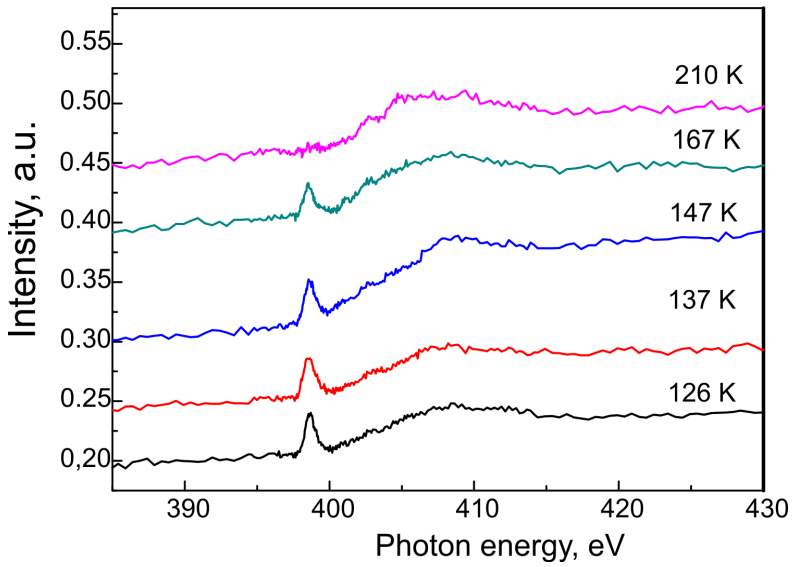

Fig. 7.9.: NEXAFS N K-edge spectra of azobenzene adsorbed on rutile TiO_2(110) measured in the temperature range of 126 - 210 K and at 55° radiation incidence.

Fig. 7.10 presents NEXAFS C K-edge spectra of azobenzene adsorbed on rutile TiO_2(110) at 100 K after heating to 290 K. The profile as corresponds to the StoBe

calculation for the aniline (Fig. 7.4). The difference between π* and σ* resonance intensities at grazing and normal incidence points out to the average angle of 45 degrees to the surface.

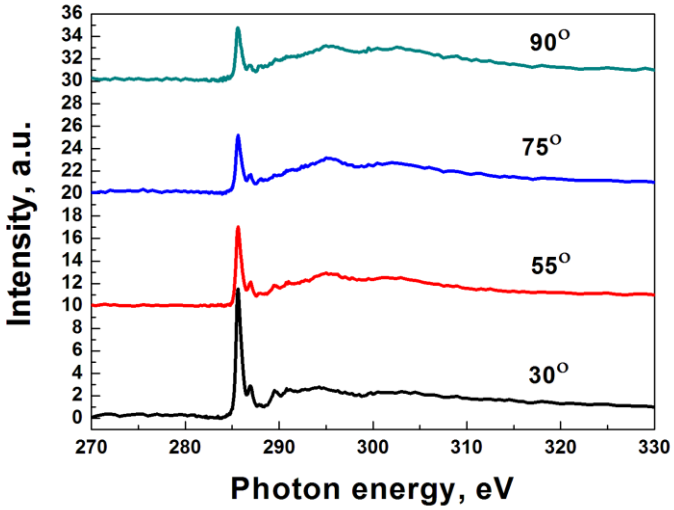

Fig. 7.10.: NEXAFS C K-edge spectra of azobenzene adsorbed on rutile TiO_2(110) at 100 K after heating to 290 K.

XPS data (Ti2p, O1s, C1s and N1s lines) were collected in normal emission geometry for the samples at the temperature 100 K and after heating to 290 K. The excitation energy was 600 eV for Ti2p and O1s lines and 450 eV for C1s and N1s lines. The Ti2p and O1s lines measured at room temperature for the clean rutile TiO_2(110) substrate, after the deposition of azobenzene at 100 K, and annealing back to the room temperature are presented in Fig. 7.11(a) (bottom, middle and top curve respectively). The Ti2p XPS spectrum of the clean rutile TiO_2(110) surface measured at room temperature has double maximum due to the spin orbital splitting: $Ti2p_{1/2}$ at 464.87 eV and $Ti2p_{3/2}$ at 459.13 eV. Upon deposition of azobenzene at 100 K a small shift of about 0.24 eV is observed for Ti2p lines. After the temperature is increased the peak returns to its original position. Since the shift is very small and the position of Ti2p lines is in

agreement to that observed before [29] we can safely exclude any effects related to the surface charging for any XPS observed in this experiment. The interesting behavior can be observed for O1s peak. For the clean surface only one O1s peak appear at the energy 530.6 eV (Fig. 7.11(b), buttom curve). However, directly after deposition of azobenzene at 100 K the second oxygen peak appears at 533.6 eV (Fig. 7.11(b), middle curve). When the sample is heated to 290 K and oxygen peak at 533.6 eV disappears (Fig. 7.11(b), top curve). To clarify the source of this second oxygen peak, a stoichiometry analysis was carefully performed by evaluating of XPS peak intensities. The peak area of two O1s peaks appearing at low temperature is equal to the peak area of the O1s peak of the clean surface and the surface after heating to 290 K. Thus, the second oxygen peak must belong also to the substrate and is related to the different chemical state of oxygen.

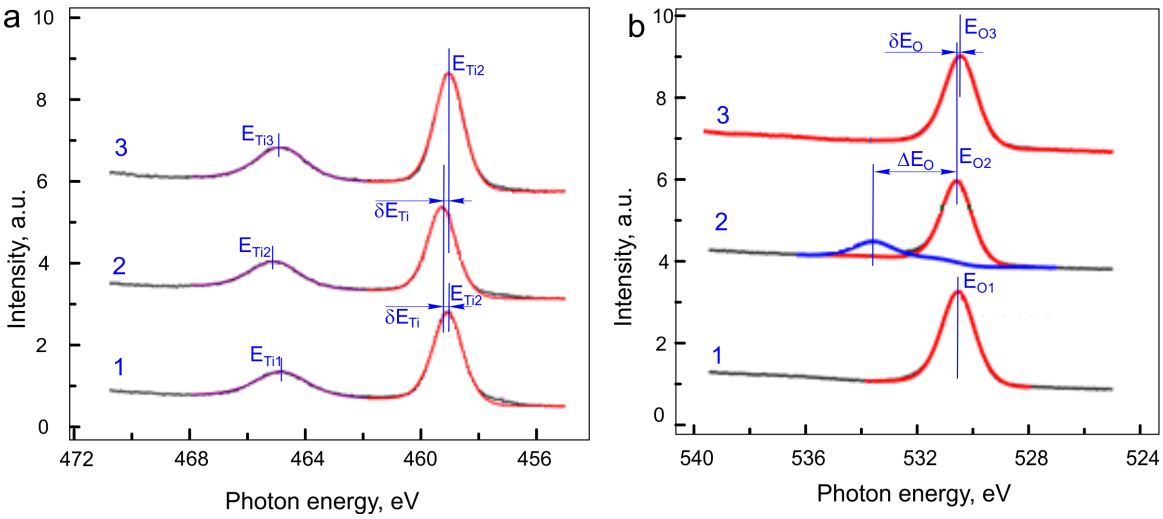

Fig. 7.11.: XPS of Ti2p (a) and O1s (b) lines of azobenzene monolayer adsorbed on rutile TiO_2(110).

C1s and N1s XPS lines are presented in Fig. 7.12 (a), (b) correspondingly. The deconvolution of C1s peak revealed 5:1 ratio distribution between one amine and five aliphatic carbons both at 100 K and at room temperature. However, due to the heating to the room temperature, the amine (285.5 eV) and aliphatic (284.7 eV) C1s peaks shift to

285.2 eV and 284.0 eV respectively. This energy position of C1s peak is very close to this value for aniline reported in the literature [102]. The N1s line also shift to lower binding energies upon annealing from 400.2 eV to 399.5 eV. The similar behavior of the N1s peak was observed in [103] where the transformation aniline to azobenzene was studied on the graphene surface. On the base of the XPS and NEXAFS data we suggest that the second oxygen peak observed for azobenzene adsorbed at 100 K (Fig. 7.11 (b), middle curve) might be caused by the interaction between the bridge oxygen atoms of the rutile TiO_2(110) and nitrogen atoms of azobenzene.

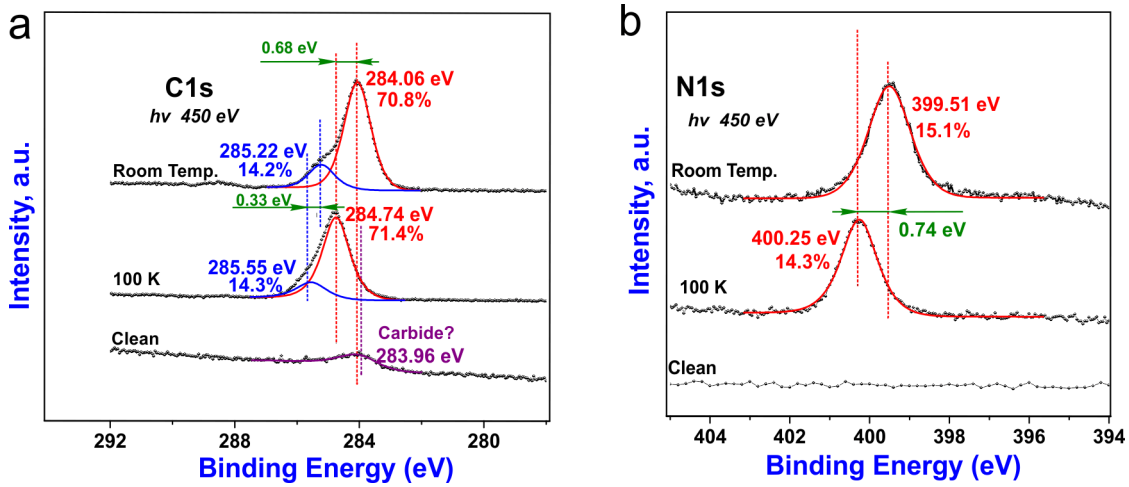

Fig.7.12.: XPS of C1s and N1s lines of azobenzene monolayer adsorbed on rutile TiO_2(110).

7.3. Conclusion

Thus, the NEXAFS and XPS study revealed that azobenzene adsorbs as an intact molecule on the rutile TiO_2(110) surface at 100 K. Unfortunately it is still not possible to make any definite conclusion about the conformation and exact orientation of the molecule with respect to the surface on the base of NEXAFS data. Since, the trans-configuration is considered to be favorable only for a very small coverage ~0.02 ML [29] and at the full coverage the phenyl rings were reported to be flipped as a result of intermolecular interaction, one can assume that the 1 ML of azobenzene adopts a cis-

configuration at the temperature of 100 K. Gradual heating of the substrate leads to the cleavage of N=N bond at the temperature of 190 ± 20 K. As a result two phenyl imide molecules are produced. The analysis of XPS data suggests us that the observation of a secondary O feature at the temperature 100 K is presumably a result of the interaction between the bridge oxygen atoms of the rutile TiO_2(110) substrate and the nitrogen atoms of azobenzene molecules at the temperature of 100 K.

CONCLUSIONS

In context of this experimental thesis the proper functionality of the newly constructed NEXAFS/XPS set-up has been demonstrated. The results for different organic adsorbate metal oxide systems: TPA/r-TiO_2(110), tetracene/Al_2O_3/Ni_3Al(111), azobenzene/Al_2O_3/Ni_3Al(111) were obtained. All three systems were studied using NEXAFS and synchrotron based XPS. LEED was used as an additional technique for the substrate characterization. NEXAFS experimental measurements were supported by the simulation of the NEXAFS data for the organic molecules in the gas phase using StoBe software package.

For the terephthalic acid adsorbed on the rutile TiO_2(110) surface the most important finding was the upright orientation of the saturated coverage of TPA. The importance of this result lies in the fact that it demonstrated the suitability of metal oxides in particular TiO_2 to be used as a template for the structured organic monolayers growth. The monolayer of the carboxyl-terminated TPA may found a similar application as the carboxyl-terminated self-assembling monolayers. The future work on this system may go in the direction of functionalization of the carboxyl-terminated monolayer with metal ions like $Zn^{2+,}$ Cu^{2+} and further toward the MOF growth.

For the Al_2O_3/Ni_3Al(111) functionalized with tetracene the important result was that the orientation of the tetracene at thin coverage has become more up-standing upon annealing to 280 K and cooling back to 100 K. This result is a strong confirmation of the existing theory, where the optic properties of tetracene depend on the molecular orientation. Luminescence will be quenched if the molecules lie more flat due to the electronic coupling of tetracene with the substrate and restores if the molecules change the orientation to the more up-standing. This theory can be also checked in the future on

other molecules from the acene family, for instance pentacene. In would be also interesting to use the alternative isolation barriers like NaCl thin films instead of the ultrathin Al_2O_3 layer.

NEXAFS/XPS study of azobenzene on rutile TiO_2(110) was conducted both at room and at low temperatures. In addition to the direct confirmation of the N=N bond cleavage at room temperature, which was already suggested in previous studies, it was shown that azobenzene adsorbs as an intact molecule at low temperatures (100 K). Considering the results obtained for the terephthalic acid on rutile TiO_2(110) it may be also reasonable to study the adsorption of azobenzene derivatives containing carboxyl groups in order to create a monolayer of up-right oriented azobezene containing molecules on the surface, the example of such a molecule can azobenzene-4,4'-dicarboxylic acid. This system may found further application similar to the photoswitchable azobenzene containing SAMs on gold substrates.

REFERENCES

1. V. E. Henrich, **The surfaces of metal oxides.** *Rep. Prog. Phys.,* **48,** 1985: p. 1481-1541.
2. T. Asanuma, T. Matsutani, C. Liu, T. Mihara and M. Kiuchi, **Structural and optical properties of titanium dioxide films deposited by reactive magnetron sputtering in pure oxygen plasma.** *Journal of Applied Physics,* **95,** 2004: p. 6011–6016.
3. L.J. Meng, M.P. dos Santos, **Investigations of titanium oxide films deposited by d.c. reactive magnetron sputtering in different sputtering pressures**. *Thin Solid Films,* **226,** 1993: p. 22-29.
4. P. Löbl, M. Huppertz and D. Mergel, **Nucleation and growth in TiO_2 films prepared by sputtering and evaporation.** *Thin Solid Films*, **251,** 1994: p. 72-79.
5. A. M. Ma, M. Gupta, F. R. Chowdhury, M. Shen, K. Bothe, K. Shankar, Y. Tsui, D. W. Barlage, **Zinc oxide thin film transistors with Schottky source barriers.** *Solid-State Electronics,* **76**, 2012: p. 104–108.
6. U. Diebold, S.-Ch. Li and M. Schmid, **Oxide surface science.** *Annu. Rev. Phys. Chem.* **61,** 2010: p. 129–48.
7. U. Diebold, **The surface science of titanium dioxide.** *Surface Science Reports,* **48,** 2003: p. 53-229.
8. C. Pang, R. Lindsay, G. Thornton, **Chemical reactions on rutile TiO_2(110).** *Chem. Soc. Rev.,* **37,** 2008: p. 2328-2353.
9. A. G. Thomas and K. L. Syres, **Adsorption of organic molecules on rutile TiO_2 and anatase TiO_2 single crystal surfaces.** *Chem. Soc. Rev.*, **41**, 2012: p. 4207-4217.
10. U. Diebold, M. Li, O. Dulub, E.L.D. Hebenstreit, W. Hebenstreit, **The relationship between bulk and surface properties of rutile TiO_2(110).** *Surface Review and Letters,* **7**, 2000: p. 613-617.
11. *http://www-brs.ub.ruhr-uni-bochum.de/netahtml/HSS/Diss/ReissSebastian/*
12. S. Reiß, H. Krumm, A. Niklewski, V. Staemmler and Ch. Wöll, **The adsorption of acenes on rutile TiO_2(110): A multi-technique investigation.** *Journal of Chemical Physics*, **116,** 2002: p. 7704–7713.

13. S. Suzuki, Y. Yamaguchi, H. Onishi, K. Fukui, T. Sasaki and Y. Iwasawa, **Study of pyridine and its derivatives adsorbed on a TiO_2(110)-(1x1) surface by means of STM, TDS, XPS and MD calculation in relation to surface acid base interaction.** *J. Chem. Soc., Faraday Trans,* **94,** 1998: p. 161-166.
14. S. Suzuki, Y. Yamaguchi, H. Onishi, T. Sasaki, K. Fukui and Y. Iwasawa, **STM visualization of site-specific adsorption of pyridine on TiO_2(110).** *Catalysis Letters,* **50**, 1998: p. 117-123.
15. S. A. Chambers, S. Thevuthasan, Y. J. Kim, G.S. Herman, Z. Wang, E. Tober, R.Ynzunza, J. Morais, C. H. F. Peden, K. Ferris, C.S. Fadley, **Chemisorption geometry of formate on TiO_2(110) by photoelectron diffraction.** *Chemical Physics Letters,* **267**, 1997: p. 51-57.
16. B. E. Hayden, A. King, M.A. Newton, **Fourier transform Reflection Absorption IR Spectroscopy Study of Formate Adsorption on TiO_2(110).** *J. Phys. Chem. B,* **103,** 1999: p. 203-208.
17. A. Gutierrez-Sosa, P. Martinez-Escolano, H. Raza, R. Lindsay, P.L. Wincott, G. Thornton, **Orientation of carboxylates on TiO_2(110).** *Surface Science,* **471,** 2001: p. 163-169.
18. Q. Guo, E.M. Williams, **The effect of adsorbate–adsorbate interaction on the structure of chemisorbed overlayers on TiO_2(110),** *Surf. Sci.,* **433-435**, 1999: p. 322-326.
19. H. Onishi, Y. Yamaguchi, K.-i. Fukui, Y. Iwasawa, **Temperature-Jump STM observation of reaction intermediate on metal-oxide surfaces.** *J. Phys. Chem.* **100**, 1996: p. 9582-9584.
20. Q. Guo, I. Cocks, E.M. Williams, **The adsorption of benzoic acid on a TiO_2(110) surface studied using STM, ESDIAD and LEED.** *Surface Science* **393,** 1997: p. 1-11.
21. L. Patthey, H. Rensmo, P. Persson, K. Westermark, L. Vayssieres, A. Stashans, A. Petersson, **Adsorption of bi-isonicotinic acid on rutile TiO_2(110).** *J. Chem. Phys.*, **110**, 1999: p. 5913-5918.
22. P. Persson, S. Lunell, P.A. Brühwiler, J. Schnadt, S. Södergren, J.N. O'Shea, O. Karis, H. Siegbahn, N. Martensson, M. Bassler, L. Patthey, **N 1s x-ray absorption study of the bonding interaction of bi-isonicotinic acid adsorbed on rutile TiO_2(110).** *J. Chem. Phys.*, **112**, 2000: p. 3945.

23. O. M. Yaghi, M. O'Keeffe, N. W. Ockwig, H. K Chae, M. Eddaoudi, J. Kim, **Reticular synthesis and the design of new materials.** *Nature*, **423**, 2003: p. 705–714.
24. J. C. Love, L. A. Estroff, J. K. Kriebel, R. G. Nuzzo, M. Whitesides, **Self-assembled monolayers of thiolates on metals as a form of nanotechnology.** *Chem. Rev.* **105,** 2005: p. 1103–1169.
25. A. Tekiel, J. S. Prauzner-Bechcicki, S. Godlewski, J. Budzioch, M. Szymonski, **Self-Assembly of terephthalic acid on rutile TiO_2(110): toward chemically functionalized metal oxide surfaces.** *J. Phys. Chem. C* **112,** 2008: p. 12606–12609.
26. J. S. Prauzner-Bechcicki, S. Godlewski, A. Tekiel, P. Cyganik, J. Budzioch, M. J. Szymonski, **High-resolution STM studies of terephthalic acid molecules on rutile TiO_2(110)-(1×1) surfaces**. *Phys. Chem. C*, **113,** 2009: p. 9305–9315.
27. M. Watkins, T. Trevethan, M. L. Sushko, A. L. Shluger, **Designing Molecular Architecture to Control Diffusion and Adsorption on Insulating Surfaces.** *J. Phys. Chem. C,* **112,** 2008: p. 4226–4231.
28. *S.* C. Li and U. Diebold, **Reactivity of TiO_2 rutile and anatase surfaces toward nitroaromatics.** *J. Am. Chem. Soc.,* **132**, 2010: p. 64.
29. A. Grirrane, A. Corma and H. Garcia, **Gold-Catalyzed Synthesis of Aromatic Azo Compounds from Anilines and Nitroaromatics.** *Science*, **322**, 2008: p. 1661–166.
30. J. P. Prates Ramalho and F. Illas, **Theoretical study of the adsorption and dissociation of azobenzene on the rutile TiO_2(110) surface.** *Chemical Physics Letters*, **501,** 2011: p. 379– 384.
31. M. K. Bradley, J. Robinson, and D. P. Woodruff, **Identifying the azobenzene/aniline reaction intermediate on TiO_2(110): A DFT Study.** *J. Phys. Chem. C,* 2013, **117**: p. 12591−12599.
32. M. Hansen, K. Anderko, **Constitution of binary alloys**. *2.* edition, Mc Graw-Hill Book Company, New York (1958).
33. Y. Lei, A. Uhl, C. Becker , K. Wandelt, B.C. Gates, R. Meyer, M. Trenary, **Adsorption and reaction of $Rh(CO)_2$(acac) on Al_2O_3/Ni_3Al(111)**. *Phys. Chem. Chem. Phys.,* **12**, 2010: p. 1264–1270.

34. C. Becker, J. Kandler, H. Raaf, R. Linke, T. Pelster, M. Drager, M. Tanemura, K. Wandelt. **Oxygen adsorption and oxide formation on Ni_3Al (111).** *J. Vac. Sci. Technol A,* **16**, 1998: p. 1000-1005.
35. A. Stierle, F. Renner, R. Streitel, H. Dosch, W. Drube, B.C. Cowie, **X-ray diffraction study of the ultrathin Al_2O_3 layer on NiAl (110).** *Science,* **303**, 2004: p. 1652.
36. S. Degen, C. Becker and K. Wandelt. **Thin alumina films on $Ni_3Al(111)$: A template for nanostructured Pd cluster growth.** *Faraday Discuss.,* **125,** 2004: p. 343–356.
37. C. Becker, K. von Bergmann, A. Rosenhahn, J. Schneider and K. Wandelt, **Preferential cluster nucleation on long-range superstructures on Al_2O_3/Ni_3Al (111).** *Surf. Sci.,* **486**, 2001: p. 443-448.
38. A. Wiltner, A. Rosenhahn, C. Becker, P. Pervan, M. Milun, M. Kralj and K. Wandelt, **Growth of copper and vanadium on a thin Al_2O_3-film on $Ni_3Al(111)$.** *Thin Solid Films,* **400**, 2001: p. 71.
39. C. Becker, A. Rosenhahn, A. Wiltner, K. von Bergmann, P. Pervan, M. Milun, M. Kralj and K. Wandelt, **Al_2O_3-films on $Ni_3Al(111)$: a template for nanostructured cluster growth.** *New J. Phys,* **4,** 2002: p. 75.
40. M. B. Casu, A. Schöll, K. R. Bauchspiess, D. Hübner, T. Schmidt, C. Heske and E. Umbach, **Nucleation in organic thin film growth: perylene on $Al_2O_3/Ni_3Al(111)$.** *J. Phys. Chem. C,* **113**, 2009: p. 10990–10996.
41. C. Santato, I. Manunza, A. Bonfiglio, F. Cicoira, P. Cosseddu, R. Zamboni and M. Muccini, **Tetracene light-emitting transistors on flexible plastic substrates.** *Applied Physics Letters,* **86**, 2005: p. 141106.
42. W. Gebauer, A. Langner, M. Schneider, M. Sokolowski, E. Umbach, **Luminescence quenching of ordered π-conjugated molecules near a metal surface: quaterthiophene and PTCDA on Ag(111).** *Phys. Rev. B,* **69,** 2004: p. 155431.
43. M. Schneider, E. Umbach, A. Langner, M. Sokolowski, **Luminescence of molecules adsorbed on surfaces of wide gap materials.** *Journal of Luminescence,* **110,** 2004: p. 275–283.
44. A. Langner, Y. Su, and M. Sokolowski, **Luminescence quenching of tetracene films adsorbed on an ultrathin alumina AlOx layer on $Ni_3A(111)$**. *Phys.Rev. B,* **74**, 2006: p. 045428.

45. S. Soubatch, R. Temirov, M. Weinhold, F.S. Tautz, **The interplay between molecular orientation, film morphology and luminescence properties of tetracene thin films on epitaxial AlOx/Ni$_3$Al(111).** *Surface Science,* **600,** 2006: p. 4679–4689.
46. E. J. N. Wilson. **"Fifty Years of Synchrotrons"**. CERN, Geneva, Switzerland. Conference proceeding, 1996.
47. F. R. Elder, A. M. Gurewitsch, R. V. Langmuir, H. C. Pollock**, Radiation from electrons in a synchrotron,** *Physical Review,* **71,** 1947: p. 829-830.
48. O. Glasser, **Wilhelm Conrad Röntgen and the early history of the Röntgen rays.** Julius Springer, Berlin, 1931.
49. S. Mobilio, A. Balerna, **Introduction to the main properties of synchrotron radiation.** *Conference proceedings – Italian Physical Society,* **82**: p. 1-24.
50. E. E. Koch, D. E. Eastman and Y. Farges, **Handbook of Synchrotron Radiation**. *Vol.1a* , Chapter 1, Ed. by E. E. Koch (North-Holland Pub-lishing Company, Amsterdam), 1983.
51. G. Yalovega, I. Rodina, A. Soldatov. **Synchrotron radiation: methods of matter research.** Tutorial review (in russian). Southern Federal University, 2004, Rostov on Don, Russia.
52. *http://www.helmholtz-berlin.de/zentrum/historie/bessy/index_de.html. Cited 25.02.2013*
53. J. F. Watts, J. Wolstenholme, **An Introduction to Surface Analysis by XPS and AES.** *John Wiley & Sons,* Chichester, UK. 23.05.2003 - 212 Pages.
54. T. A. Carlson, **Basic Assumptions and Recent Developments in Quantitative XPS.** *Surface and Interface analysis,* **4,** 1982: p. 125-133.
55. G. Hähner, **Near edge X-ray absorption fine structure spectroscopy as a tool to probe electronic and structural properties of thin organic films and liquids.** *Chemical, Soc, Rev.*, **35**, 2006: p. 1244.
56. J. Stöhr, **NEXAFS Spectroscopy**. Springer, Berlin, 1992.
57. A. Nefedov, Ch. Wöll, **Advanced Applications of NEXAFS Spectroscopy for Functionalized Surfaces, in Surface Science Techniques**. (Eds) G. Bracco and B. Holst Springer Series in Surface Science, **v. 51**, (Springer-Verlag, Berlin, Heidelberg, New York, Tokyo): p.277-306.

58. K. Oura, V. G. Lifshifts, A. Saranin, A.V. Zotov, M. Katayama, **Surface Science: An Introduction.** Springer, Berlin Heidelberg New York, 2003: p. 1–45.
59. R. M. Martin, **Electronic Structure: Basic Theory and Practical Methods. Basic Theory and Practical Density Functional Approaches v. 1.** Cambridge University Press 2004.
60. E. Eberhard, R. M. Dreizler, **Density Functional Theory: An Advanced Course (Theoretical and Mathematical Physics),** Springer Verlag Berlin Heidelberg 2004.
61. J. T. Oden, **An introduction to mathematical modeling. A course in mechanics.** Wiley E-Text 2012.
62. C. Fiolhais, F. Nogueira, M. Marques, **A primer in density functional theory.** Springer-Verlag Berlin Heidelberg 2003.
63. http://www.staff.uni-mainz.de/sulpizi/teaching_files/lecture_2.pdf cited 01.06.13.
64. *http://www.fhi-berlin.mpg.de/KHsoftware/StoBe/index.html* cited 01.06.13.
65. L. Triguero, L. G. M. Pettersson and H. Agren, **Calculations of near-edge X-ray-absorption spectra of gas-phase and chemisorbed molecules by means of density-functional and transition-potential theory.** *Phys. Rev. B,* **58**, 1998: p. 8097.
66. K. Tamada, H. Akiyama, T. X. Wei, **Photoisomerization reaction of unsymmetrical azobenzene disulfide self-assembled monolayers studied by surface plasmon spectroscopy: influences of side chain length and contacting medium.** *Langmuir*, **18,** 2002: p. 5239–5246.
67. K. Tamada, H. Akiyama, T. X. Wei, S. A. Kim, **Photoisomerization reaction of unsymmetrical azobenzene disulfide self-assembled monolayers: modification of azobenzene dyes to improve thermal endurance for photoreaction.** *Langmuir*, **19**, 2003: p. 2306–2312.
68. S. H. Bao, L. D. Yin, T. J. Shu, **The intermolecular interaction in self-assembled monolayers on gold electrode.** *Chin. Chem. Lett.* **10**, 1999: p. 145–146.
69. U. Jung, S. Kuhn, U. Cornelissen, F. Tuczek, T. Strunskus, V. Zaporojtchenko, J. Kubitschke, R. Herges, and O. Magnussen, **Azobenzene-containing triazatriangulenium adlayers on Au (111): structural and spectroscopic characterization**. *Langmuir*, **27**, 2011: p. 5899–5908.

70. R. Baer, D. M. Charutz, R. Kosloff and M. Baer, **A study of conical intersection effects on scattering processes: the validity of adiabatic single-surface approximations within a quasi-Jahn–Teller model.** *J. Chem. Phys.* **111**, 1996: p. 9141.
71. D. S. Sholl, J. A. Steckel, **Density functional theory: A practical introduction.** Wiley, Hoboken, 2009.
72. A. Lippitz, J. F. Friedrich, W. E. S. Unger, A. Schertel, Ch. Wöll, **Surface analysis of partially crystalline and amorphous poly(ethylene terephthalate) samples by X-ray absorption spectroscopy (NEXAFS).** *C. Polymer,* **37,** 1996: p. 3151–3155.
73. T. Okajima, K. Teramoto, R. Mitsumoto, H. Oji, Y. Yamamoto, I. Mori, H. Ishii, Y. Ouchi, K. Seki, **Polarized NEXAFS spectroscopic studies of Poly(Butylene terephtalate), Poly(Ethylene-terephthalate), and their model compounds.** *J. Phys. Chem. A*, **102,** 1998: p. 7093–7099.
74. F. Zasada, W. Piskorz, S. Godlewski, S. Jakub, P. Bechcicki, A. Tekiel, J. Budzioch, P. Cyganik, M. Szymonski and Z. Sojka, **Chemical Functionalization of the TiO_2(110)-(1x1) Surface by deposition of terephthalic acid molecules. A Density functional theory and scanning tunneling microscopy study**. *Phys. Chem. C,* **115**, 2011: p. 4134–4144.
75. G. Witte, Ch. Wöll, **Growth of aromatic molecules on solid substrates for applications in organic electronics.** *J. Mat. Res.* **19**, 2004: p. 1889.
76. F.-J. Meyer zu Heringdorf, M. C. Reuter and R. M. Tromp, **Growth dynamics of pentacene thin films.** *Nature*, **412**, 2001: p. 517.
77. R. Ruiz, B. Nickel, N. Koch, L. C. Feldman, R. F. Haglund, A. Kahn, and G. Scoles, **Pentacene ultrathin film formation on reduced and oxidized Si surfaces.** *Phys. Rev. B,* **67,** 2003: p. 125.
78. K. Kang, Z. G. Zhang, C. Papusoi, and T. Suzuki, **(001) oriented FePt–Ag composite nanogranular films on amorphous substrate.** *Appl. Phys. Lett.,* **82**, 2003: p. 3284.
79. Y. Luo, G. Wang, J. A. Theobald, P. H. Beton, **Fractal-compact island transition and self-limiting growth of pentacene on polymers.** *Surf. Sci.,* **537,** 2003: p. 241.

80. T. Breuer, I. Salzmann, J. Götzen, M. Oehzelt, A. Morherr, N. Koch, and G. Witte, **Interrelation between ubstrate roughness and thin-film structure of functionalized acenes on graphite.** *Cryst. Growth*, **11,** 2011: p. 4996.
81. J. Götzen, D. Käfer, Ch. Wöll and G. Witte, **Growth and structure of pentacene films on graphite: weak adhesion as a key for epitaxial film growth.** *Phys. Rev. B*, **81,** 2010: p. 4997.
82. Y. Guo, G. Yu, Y. Liu, **Functional organic field-effect transistors.** *Advanced Materials*, **22**, 2010: p. 4427–4447.
83. C. Santato, I. Manunza, A. Bonfiglio, F. Cicoira, P. Cosseddu, R. Zamboni and M. Muccini, **Tetracene light-emitting transistors on flexible plastic substrates.** *Applied Physics Letters*, **86**, 2005: p. 141106.
84. http://www.nist.gov/srd/nist82.cfm
85. T. Sueyoshi, M. Willenbockel, M. Naboka, A. Nefedov, S. Soubatch, Ch. Wöll and S. F. Tautz, **Spontaneous change in molecular orientation at order-disorder transition of tetracene on Ag(111**). *J. Phys. Chem. C,* **117**, 2013, 9212–9222.
86. D. T. Jiang, J. Shi, A. Tersigni, T. Regier and X. R. Qin, **NEXAFS study of tetracene and pentacene thin films,** *Canadian Light Source 2007 Activity Report*, 32-33.
87. S. Soubatch, I. Kröger, C. Kumpf, and F. S. Tautz, **Structure and growth of tetracene on Ag(111).** *Journals Phys. Rev. B,* **Volume 84,** 2011: p 195440.
88. Y. Joseph, M. Wühn, A. Niklewski, W. Ranke, W. Weiss, Ch. Wöll and R. Schlögl, **Interaction of ethylbenzene and styrene with iron oxide model catalyst films at low coverages: A NEXAFS study.** *Phys. Chem. Chem.* Phys., **2**, 2000 p. 5314-5319.
89. A.Grüneis, D.Vyalikh. **Tunable hybridization between electronic states of graphene and a metal surface.** *Phys. Rew. B,* **77**, 2008: p. 193401.
90. W. Zhang, A. Nefedov, M. Naboka and Ch. Wöll. **Molecular orientation of terephthalic acid assembly on graphene: NEXAFS and XPS study.** *Phys. Chem. Chem.Phys.,* **14**, 2012: p. 10125-10131.
91. A. Shaporenko, A. Terfort, M. Grunze, M. Zharnikov**. A detailed analysis of the photoemission spectra of basic thioaromatic monolayers on noble metal substrates.** *J. Electr. Spectr. Rel. Phenom.,* **151,** 2006: p. 45–51.

92. A. Corma, P. Serna, **Chemoselective Hydrogenation of nitro compounds with supported gold catalysts.** *Science,* **313,** 2006: p. 332-334.

93. A. Grirrane, A. Corma, H. Garcia, **Gold-catalyzed synthesis of aromatic azo compounds from anilines and nitroaromatics.** *Science,* **322,** 2008: p. 1661.

94. Sh.-Ch. Li, Y. Losovyj, V. K. Paliwal, and U. Diebold, **Photoemission study of azobenzene and aniline adsorbed on TiO_2 anatase (101) and rutile (110) surfaces.** *J. Phys. Chem. C*, **115**, 2011: p. 10173–10179.

95. J.-P. Sauvage, **Molecular machine and motors.** Springer; Edition: 2001 (3. July 2001)

96. A. A. Beharry and G. A. Woolley, **Azobenzene photoswitches for biomolecules.** *Chem. Soc. Rev.,2011,* **40**: p 4422-4437.

97. H. Rau in **Photochromism molecules and systems.** ed. H. Durr and H. Bouas-Laurent, Elsevier, Amsterdam, 1990: p. 165–192.

98. G. Tiberio, L. Muccioli, R. Berardi, C. Zannoni, **How does the trans-cis photoisomerization of azobenzene take place in organic solvents?** *ChemPhysChem*, **11,** 2010: p. 1018–1028.

99. J. Dokić, M. Gothe, J. Wirth, M. V. Peters, J. Schwarz, S. Hecht and P. Saalfrank, **Quantum chemical investigation of thermal cis-to-trans isomerization of azobenzene derivatives: substituent effects, solvent effects, and comparison to experimental data**. *J. Phys. Chem. A*, **113,** 2009: p. 6763–6773.

100. A. Safei, J. Henzl and K. Morgenstern, **Isomerization of an azobenzene derivative on a thin insulating layer by inelastically tunneling electrons**. *Phys. Rev. Lett.* **104,** 2010: p. 216102.

101. E. Ludwig, T.Strunscus, S. Hellmann, A. Nefedov, Ch. Wöll, L. Kipp and K. Rossnagel, **Electronic structure, adsorption geometry, and photoswitchability of azobenzene layers adsorbed on layered crystals.** *Phys. Chem Chem Phys.,* **15**, 2013: p. 20272.

102. J.L. Solomon, R.J. Madix, J. Stöhr**, Orientation and absolute coverage of benzene, aniline, and phenol on Ag(110) determined by NEXAFS and XPS**.*Surface Science,* **255,** 1991: p. 12–30.

103. M. Lee, K. Kim and H. Lee, **The aniline-to-azobenzene oxidation reaction on monolayer graphene or graphene oxide surfaces fabricated by benzoic acid.** *Nanoscale Research Letters,* **8,** 2013: p. 372.

APPENDIX A

Use of the StoBe package for the simulation of NEXAFS spectra of the free molecules on example of benzene:

The typical file will include:

Title - brief descriptive title of the present StoBe run on the lines following the keyword. This title appears in the output file(s).

Keywords:

NOSYmmetry - do not use symmetry
SYMMetry - use of spatial symmetry and unrestricted calculations
CARTesian - geometry input in cartesian coordinates
ZMATrix - geometry input in internal coordinates

CARTesian ..., each line defines one atom (I) of
the system. The input format is:

Nm X Y Z ZZ

where

Nm is element symbol for atom, followed by up to two numbers.

ZZ is effective nuclear charge of atom. This may be different
from the atomic number if model core potentials.

X, Y, Z = x , y , z coordinates of atom given in Angstrom.

Runtype
This keyword defines the type of calculation to be performed. Depending on the run type up to two option keywords (which must be consistent) are needed where all meaningful combinations are discussed in the following.

Scftype
This keyword defines the method of handling 2-electron integrals to construct the Kohn-Sham matrices and allows forcing numerical evaluation of the exchange-correlation potentials and total energy in the SCF-cycles rather than using the fitted potentials based on the auxiliary basis.

Potential
The exchange-correlation functional used in the calculations is defined by three keywords characterizing the

- overall type of functional FTYP (LOCAl, NONLocal, MIXEd),

- the exchange part EXCH (NORMal, PD86, PD91, PVS1, BE88, BECKe, DEPK, BE86, BA86, PBE, PBE2, RPBE), and

- the correlation part CORR (XALPha, VWN, PD91, PVS1, PD86, PD91, LAP, PBE)

Grid
The user specifies the quality and type of the grids used for the least squares fit of the exchange-correlation potentials and final energy density. Keyword GRID comes with up to three additional option keywords from the following three groups.

Multiplicity
Spin multiplicity of the N-electron state. Numbers 1, 2, 3, etc. refer to singlet, doublet, triplet, etc. states. By default, a singlet state is assumed (leading to an error message for systems where the total number of electrons is odd). The spin multiplicity together with the net charge, see CHARge, determines the total number of spin alpha and beta orbitals to be occupied and the multiplicity / charge values are checked for consistency.

Charge
Net charge of the system, positive (negative) for cations (anions). By default, the system is assumed neutral (number = 0). The net charge together with the spin multiplicity, determines the total number of spin alpha and beta orbitals to be occupied and the multiplicity / charge values are checked for consistency.

Maxcycles
This keyword defines the maximum number of iterations, NSCF, calculated in any SCF procedure (single point calculation or geometry optimization). The default value is NSCF=50. Note that restarting a run with NSCF=0 calculates only 1-electron properties without iterating and no restart file will be written

ECONvergence
This keyword defines the energy convergence for an SCF procedure where the number gives the convergence threshold Econv (in Hartree). An SCF procedure is terminated if three consecutive values of the total energies differ by less than Econv.

DCONvergence
This keyword defines the electron density convergence for an SCF procedure where the number gives the convergence threshold Dconv (in a.u.). An SCF procedure is terminated if three consecutive values of the densities differ by less than Dconv. The default value is Dconv = 0.001 .

dmixing
This keyword defines the extrapolation between successive SCF iteration steps by linear mixing schemes.

orbi
This keyword determines the internal representation of d basis functions.

FSYMmetry SCFOccupation [EXCIted]
Uses symmetry-based block-diagonalization of the Kohn-Sham matrix and defines a fixed occupation scheme by giving the number of occupied alpha and beta orbitals for each symmetry representation.

The occupation information starts on new lines as

ALFA na1 na2 na3 ... nansym
BETA nb1 nb2 nb3 ... nbnsym

where nai, nbi are the occupation numbers of alpha and beta orbitals of each symmetry representation i, i = 1 ... nsym. These occupation numbers are kept fixed in the SCF calculation irrespective of the Aufbau principle. Note that the definition of the numbers following the 'ALFA' and 'BETA' keywords is somewhat different when used for atoms, see below. Fixed occupations are incompatible with the level smear option, see keyword SMEAr.

MULLiken [OFF / ON [FULL, ORBItal]]
This keyword includes a listing of the gross Mulliken population analysis and Mayer bond orders at the end of SCF calculations or geometry optimizations. By default, the total Mulliken population analysis and total Mayer bond orders,i. e. values summed over all occupied orbitals, are included. In addition, orbital resolved data can be requested where the analysis is performed for all occupied and virtual orbitals included in the listing. For NEXAFS calculations all excitation orbitals with intensity greater than 0.001 are included in the listing.

BASIS SET INPUT
The list of all StoBe keywords and corresponding numerical parameters is terminated by the END line. The remaining part of the input file defines the basis sets (orbital bases, auxiliary bases, model core potential (MCP or ECP) definitions, and augmentation bases for core electron spectroscopy, NEXAFS, if applicable) to be used in the calculations.

Orbital basis sets

Explicit definition:

Here the basis set of each atom center is defined by a one-line title
which refers to an entry in the basis set file provided with the input

>O-ELEMENT (n1s,n2s,...,nKs/n1p,n2p,...,nLp/n1d,n2d,...,nMd)

ELEMENT is a name which helps the user to identify the basis
(typically the element name).
K - denotes the number of s-type Gaussians with n1s,n2s,...,nKs primitives respectively

L - contractions of p-type Gaussians with n1p, n2p,...,nLp primitives,
M - contractions of d-type Gaussians with n1d,n2d,...nMd primitives
respectively.

Examples of orbital basis sets (the star at the end
denotes that a diffuse function is added) are

>O-OXYGEN (621/41/1)
>O-HYDROGEN (41/1*)
>O-NITROGEN (7111/411/1)

Auxiliary basis sets

Explicit definition
Here the basis set of each (non-equivalent) atom center is defined by a one-line title which refers to an entry in the basis set file provided with the input.

>A-ELEMENT (ns(CD),nspd(CD); ns(XC),nspd(XC))

ELEMENT is a name which helps the user to identify the basis (typically the element's name),

ns(CD) - is the number of s-type Gaussians used to fit the charge density (CD)
nspd(CD) - is the number of s-, p- and d- type Gaussians (sharing the same exponent) used to fit the valence charge density

ns(XC) and **nspd(XC)** have definitions similar to ns(CD) and nspd(CD), while referring to the Gaussians used to fit the exchange and correlation potentials.

Examples of auxiliary
basis sets are

>A-NITROGEN (4,4;4,4)
>A-OXYGEN (5,2;5,2)

Model core potential definitions

The model core potential (MCP) of each (non-equivalent) atom center is defined by a one-line title which refers to an entry in the basis set file provided with the input. Possible MCP titles are of the form

>P-LABEL(Zeff) (nv(mcp): ns(mcp),np(mcp),nd(mcp))

nv(mcp) is the number of s-type Gaussians used to fit the potential seen by the valence electrons
ns(mcp),np(mcp),nd(mcp) are respectively the number of s-, p-, and d-type Gaussians used to describe the s,p and d core orbitals and Zeff is the effective nuclear charge after removal of the core electrons.

Examples of MCP basis sets are

>P-PALLADIUM(+16) (6:9,6,4)	>P-ALUMINUM(+3) (4:6,4)
>P-PHOSPHORUS(+5) (4:6,4)	>P-GERMANIUM(+14) (3:7,5)
>P-SULFUR(+6) (4:6,4)	>P-CHLORINE(+7) (4:6,4)
>P-NICKEL(+16) (5:7,4)	>P-SILICON(+4) (4:6,4)
>P-RHODIUM(+15) (6:9,6,4)	>P-NIOBIUM(+11) (5:8,6,4)
>P-PLATINUM(+16) (7:12,9,7,5)	>P-MOLYBDENUM(+14) (5:8,6,4)

Augmentation basis sets

The model augmentation basis set of each (non-equivalent) atom center is defined by a one-line title which refers to an entry in the basis set file provided with the input. At present, this is the only way to define augmentation basis sets. Possible titles are

>X-FIRST or >X-SECOND or >X-DUMMY

where X-FIRST is sufficient for first-row systems and X-SECOND is somewhat more extended. X-DUMMY is used for all atom centers except those where the core excitation originates from.

Example of the StoBe input file for benzene molecule

```
title
C6H6 (Benzene), no symmetry, C1s transition state for Xray
absorption
nosymm
cartesian angstrom
 C -1.20809736 -0.69749534 0.00000000  6.0
 C -1.20809736 0.69749534  0.00000000  4.0
 C 0.00000000 1.39499068   0.00000000  4.0
 C 1.20809736 0.69749534   0.00000000  4.0
 C 1.20809736 -0.69749534  0.00000000  4.0
 C -0.00000000 -1.39499068 0.00000000  4.0
 H -2.16038780 -1.24730048 0.00000000  1.0
 H -2.16038780 1.24730048  0.00000000  1.0
 H 0.00000000 2.49460095   0.00000000  1.0
 H 2.16038780 1.24730048   0.00000000  1.0
 H 2.16038780 -1.24730048  0.00000000  1.0
 H -0.00000000 -2.49460095 0.00000000  1.0
end
runtype start
scftype direct
potential nonlocal be88 pd86
grid fine
multiplicity 1
charge 0
maxcycles 50
econvergence 0.000001
dconvergence 0.000001
dmixing mdens 0.25
diis new 7
orbi 5d
fsym scfocc excited
alfa 16
beta 16
sym 1
alfa 0 1 1 0.5
beta 0 0
end
mulliken on
spinconta full
xray xas
remthreshold 1.D-6
end
shrt
end
A-CARBON (5,2;5,2)
A-CARBON(+4) (3,3;3,3)
A-CARBON(+4) (3,3;3,3)
A-CARBON(+4) (3,3;3,3)
```

```
A-CARBON(+4) (3,3;3,3)
A-CARBON(+4) (3,3;3,3)
A-HYDROGEN (3,1;3,1)
A-HYDROGEN (3,1;3,1)
A-HYDROGEN (3,1;3,1)
A-HYDROGEN (3,1;3,1)
A-HYDROGEN (3,1;3,1)
A-HYDROGEN (3,1;3,1)
O-CARBON iii_iglo
O-CARBON(+4) (311/211/1)
O-CARBON(+4) (311/211/1)
O-CARBON(+4) (311/211/1)
O-CARBON(+4) (311/211/1)
O-CARBON(+4) (311/211/1)
O-HYDROGEN (311/1) misc
O-HYDROGEN (311/1) misc
O-HYDROGEN (311/1) misc
O-HYDROGEN (311/1) misc
O-HYDROGEN (311/1) misc
O-HYDROGEN (311/1) misc
P-CARBON(+4) (3,1:8,0)
P-CARBON(+4) (3,1:8,0)
P-CARBON(+4) (3,1:8,0)
P-CARBON(+4) (3,1:8,0)
P-CARBON(+4) (3,1:8,0)
X-FIRST
X-DUMMY
X-DUMMY
X-DUMMY
X-DUMMY
X-DUMMY
X-DUMMY
X-DUMMY
X-DUMMY
X-DUMMY
X-DUMMY
X-DUMMY
END
```